Sapienza University of Rome
Engineering Faculty
Department of Hydraulics, Transportations and Roads

High resolution numerical modeling of the atmospheric circulation over complex terrain

Franco Catalano

A Thesis submitted for the degree of Doctor of Philosophy

Doctoral school in Hydraulics Engineering

XXII Cycle

Supervisor: Prof. Antonio Cenedese

Referee: Prof. Dino Zardi
(Department of Civil and Environmental Engineering, University of Trento, Italy)

June 2010

«Un uomo si mette in marcia per raggiungere, passo a passo, la saggezza. Non è ancora arrivato»

«A man sets out to reach, step by step, the wisdom. He is still on the road»

Italo Calvino, presentation for "Palomar", written in 1983 and published posthumous in 1992. (English translation by the author)

Contents

Abstract

A detailed knowledge of the atmospheric circulation which characterizes the complex Planetary Boundary Layers (PBLs) typical of mountainous regions is of great interest for environmental assessment studies. Furthermore, efforts are underway in developing wind farms, often located in mountainous areas; efficient wind power-plants require detailed and reliable knowledge of wind fluctuations near the surface which cannot be learned from regional-scale investigations. The Large Eddy Simulation (LES) methodology provides three-dimensional, time evolving structure of turbulence and a much more accurate estimate of turbulence statistics compared to those from PBL schemes used by operative meteorological models.

In the present work the coherent structures and the turbulent characteristics of a complex PBL driven by surface heating, thermally-induced circulations and geostrophic wind forcing is investigated by means of the LES technique. The three-dimensional non-hydrostatic meteorological model WRF is used with a LES grid resolution to explicitly resolve the energy-containing turbulent eddies and is modified to include a new formulation for the filter width of the subgrid scale model. The LES model is coupled with a wall scheme and surface heat and momentum fluxes are computed based on Monin-Obukhov surface similarity theory.

Riassunto

L'accurata conoscenza della circolazione atmosferica e della complessa struttura dello strato limite in zone di montagna riveste una notevole importanza per gli studi di impatto ambientale. Inoltre, negli ultimi anni si stanno dedicando molte risorse per lo sviluppo e l'installazione di parchi eolici, di sovente localizzati in zone con forte presenza orografica. Lo sfruttamento efficiente dell'energia fornita dalle turbine richiede una quantificazione affidabile dell'entità delle fluttuazioni del vento in prossimità del terreno; tale informazione non può essere fornita da studi a scala regionale. La metodologia Large Eddy Simulation (LES) è in grado di riprodurre la struttura tridimensionale e non stazionaria della turbolenza atmosferica a differenti scale, garantendo statistiche turbolente con un livello di accuratezza notevolmente superiore a quello degli schemi di strato limite impiegati operativamente nei modelli meteorologici.

Nel presente lavoro le strutture coerenti e le caratteristiche turbolente dello strato limite atmosferico in presenza di orografia variabile sono indagate per mezzo della tecnica LES; le forzanti considerate comprendono: il ciclo giornaliero della temperatura al suolo, gli effetti della circolazione baroclina risultante e la presenza di un vento geostrofico. Il modello meteorologico tridimensionale non-idrostatico WRF, modificato con una nuova formulazione per la dimensione del filtro del modello di sottogriglia, è utilizzato con una risoluzione adeguata al calcolo esplicito delle strutture con contenuto energetico significativo. Il modello è accoppiato ad uno schema di parete basato sulla teoria della similarità di Monin-Obukhov per il calcolo del flusso di calore superficiale e della velocità di attrito.

Acknowledgements

List of Tables

List of Figures

1 Introduction

The Large Eddy Simulation (LES) approach is based on the explicit resolution of the governing equations for the large energy carrying structures with characteristic dimension L, while the effects of the smaller motions on the resolved fields are addressed by a subgrid scale (SGS) model. The rationale is that the smaller structures, mainly dissipative, can be considered less dependent on the flow conditions. The scale separation is obtained applying a low-pass filter to the governing equations. The dimensions of the filter, which fall within the inertial subrange, are imposed by the numerical resolution Δ.

In the last 3 decades, owing to a progressive increase of computer power, LES has become an important tool for the study of turbulent flows. Since the pioneering work of Deardorff (1972), a considerable and increasing effort has been put on the development and application of LES models to the study of atmospheric turbulence occurring in neutral and convective boundary layers (CBLs) (Moeng 1984; Nieuwstadt 1993; Sullivan et al. 1994). The smaller sizes of the energy containing eddies, which characterize the stably stratified boundary layer (SBL), require significantly more resolution and more sophisticated subgrid scale models. Nevertheless LES has provided reliable results also in the study of the SBL, particularly for the moderately stable cases (Beare et al. 2006). All these studies were conducted assuming simple idealized boundary conditions, such as horizontal homogeneity or periodicity. These assumptions are inadequate for the investigation of real Planetary Boundary Layers (PBLs), for which surface inhomogeneities along with complex orography play a fundamental role in the determination of turbulent flow features. Furthermore, in a real PBL one must consider the interaction of microscale turbulence with mesoscale motions, which poses the problem of how to correctly describe inflow and outflow turbulent conditions (Moeng et al. 2007).

Nowadays there exists two different approaches with respect to the numerical simulation of atmospheric turbulent flows: mesoscale modeling on large (from 100 km to 3000 km) domains with coarse resolution ($1 \leq \Delta \leq 50$ km) and LES on small domains (less than 20 km) with fine resolution ($\Delta \leq 200$ m). The main difference is on the amount and type of resolved turbulence and hence on the SGS models. In the region where an important issue arises about the adequacy of existing turbulent closures since these are designed to operate at different scales. Wyngaard (2004) pointed out that in this region, which he termed "Terra Incognita", a tensorial turbulent diffusivity should be considered. Then, in order to correctly reproduce the atmospheric circulation in a real PBL, we need a model able to work both on the mesoscale and microscale in a two-way nested framework, verifying the performance of the SGS models with respect to the ratio of the intermediate grids.

Most severe events of atmospheric pollution occur under weak synoptic systems when circulation is mainly driven by local forcing. Mid-latitude zones with complex orography are mainly affected by sea-land breeze regimes and slope winds, the latter often in association with valley winds. Since many urban sites are located in proximity of the coast or in mountainous regions, a detailed knowledge of the atmospheric circulation, which characterizes such complex PBLs, is of great interest for environmental assessment studies. Furthermore, large urban areas contribute to the heterogeneity of heat and moisture surface fluxes and can effectively influence the structure of the above boundary layer through the "Urban Heat Island" effect. The non-hydrostatic mesoscale model WRF (Weather Research and Forecast) has been proved to be a good tool to perform LES studies in a two-way nesting framework (Moeng et al. 2007). Following this approach, a first step toward LES of real PBLs can be the investigation of local winds under weak synoptic systems, for which we can neglect large scale forcing and work on relatively small domains. Subsequently we can extend the nested grids to perform a downscaling from the mesoscale motions, with the coarser grid designed to acquire the synoptic scale boundary conditions from a general circulation model, as in current mesoscale studies.

This work is arranged as follows. Chapter 2 presents a review of the numerical techniques used to simulate the atmospheric circulation at different scales. The problem of turbulence modeling is briefly discussed and a great emphasis is given on the Large Eddy Simulation technique and its differences with respect to the Reynolds Averaged Navier-Stokes (RANS) methodology. Chapter 3 briefly describes the state of the art of the atmospheric circulation characteristic of the mountainous regions. Chapter 4 reports the LES results of the circulation in a valley, both the unstable daytime conditions and stable nighttime regime are analyzed. Chapter 5 is devoted to the investigation of the influence of the geostrophic wind on the thermally driven circulation described in the previous chapters. The work is completed by an appendix describing the parametrical schemes used to reproduce the effects of the unresolved physics.

2 Numerical models for the atmospheric circulation

Numerical models, used for the simulation of the atmospheric circulation (meteorological models), have two main purposes:

- to efficiently and consistently interpolate the measurements of meteorological variables taken in a limited number of positions in order to obtain information in every location of interest;

- to forecast the evolution of the system; this can be done for no more than a few days, the system having chaotic characteristics.

In the latter case the measurements allow both the verification of the quality of the prediction and the update of the boundary conditions (data assimilation process).

2.1 Scales of motion

The partial derivative differential equations system upon which every meteorological model is based is formed by the balance of mass, momentum, energy and scalars (one equation for each scalar considered), along with the diagnostic equation of state.

The independent variables are the spatial coordinates x, y, η and the time t. The vertical coordinate η is a function of the hydrostatic pressure (Laprise 1992) which assumes different expressions depending on the model considered. The dependent variables are the three components of the velocity u, v, w, potential temperature θ, density ρ, pressure p, mixing ratios for water in its different states.

The concentration of the pollutants is assumed to be very low, compared to the density of the air ($c << \rho$); it is then possible to neglect the influence of the pollutants on the fluid dynamic field, their concentration is determined offline solving an additional system of differential equations (transport and dispersion equations).

The numerical solution of the differential equations system is obtained after their discretization in order to obtain an algebraic equations system. The unknowns are the values of the variables in some points of the field; the set formed by these points is the computational domain.

Turbulence plays a fundamental role in the study of the atmospheric circulation. A turbulent motion is composed of a wide range of coherent spatial structures of different lengths. Grid spacing of the order of a millimeter must be used to solve the finer structures; this is the aim of the DNS (Direct Numerical Simulation) technique.

Due to the onerous computational demand, DNS is applied only for very limited domains. Operational needs require cell dimensions much bigger than the finer turbulent structures; in this case it is more appropriate to characterize the atmospheric circulation in terms of its mean and second-moment properties. The RANS methodology is based on the Reynolds decomposition of the flow variables into mean value and turbulent fluctuation. Introducing this decomposition into the balance equations and averaging, additional terms arise from the non-linearity of the advection terms; the new unknowns are the second-order correlations of the velocity components and the cross-correlations between potential temperature and velocity. This requires additional equations in order to solve the system. Furthermore, transport equations for the second-order correlations contain as unknowns third-order correlations and, to generalize, the equations for the nth-order correlations contain as additional unknowns $n+1^{th}$-order correlations (turbulent hierarchy). It is then necessary to develop closure relations that do not require additional higher-order variables.

Like the atmospheric motions, meteorological models can be classified on the base of the resolved spatial and temporal scales.

The GCM (General Circulation Models) works on the planetary scale and their domain is the whole atmosphere of the earth. The most widely used are the European model developed by ECMWF (European Centre for Medium-Range Weather Forecasts), characterized by a horizontal resolution of 0.5° (about 50 km at the middle latitudes) and the American model GFS (Global Forecast System) developed by NOAA (National Oceanic and Atmospheric Administration), with a horizontal resolution of 1°. The GCM are used for climatological analysis and to provide medium-range weather forecasts. The initial and boundary conditions are provided by the measurements of ground stations, radiosondes and meteorological satellites.

For the investigation of synoptic and mesoscale phenomena (breezes, slope and valley winds, urban heat islands) the spatial and temporal resolution of the GCMs is not sufficient and a different category of models is necessary: LAM (Limited Area Models). These models work with domains of tens to a few thousands of kilometers and thus cannot reproduce the atmospheric structures characterized by larger dimensions. For this reason, initial and boundary conditions for these models are provided by a GCM. An important feature of LAMs is their ability to operate in a nested grids framework (nesting), with increasing resolution (Fig. 2.1).
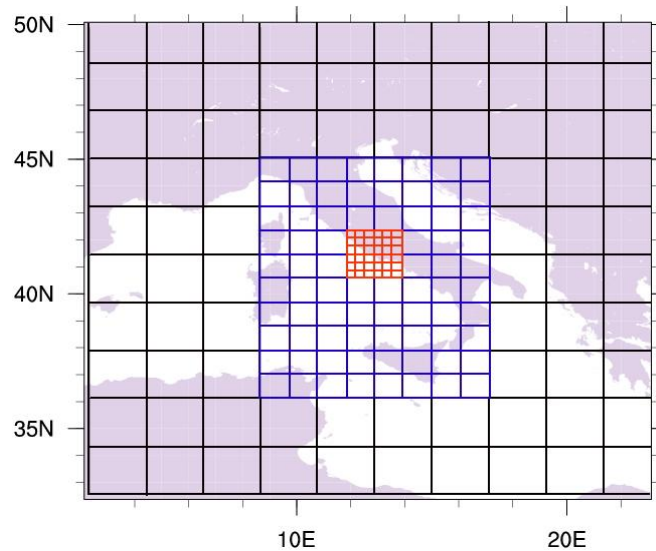
Fig. 2.1. Example of horizontal nested grids with increasing resolution.

This technique allows to extend the simulation to an area wide enough to capture the evolution of the synoptic scale and, at the same time, to reproduce the mesoscale simulation which requires a finer resolution, optimizing the number of grid point and hence the computational time. A typical configuration for a mesoscale study is: a coarse grid with a horizontal resolution of 50 km, an intermediate grid with a spacing of 10 km and a fine mesh with a resolution of 2 km. The vertical grid is non homogeneous, having a finer resolution near the ground (vertical stretching). The higher resolution near the surface is justified by the consideration that it is in the lower portion of the domain that mesoscale forcings develop.

A first classification of LAMs is based on the hypothesis on the vertical distribution of pressure in atmosphere: hydrostatic and non-hydrostatic. The hydrostatic hypothesis assumes that vertical acceleration components are negligible with respect to pressure gradients; this assumption becomes then inacceptable at resolutions higher than 10 km.

The eddies smaller than the grid dimensions are not explicitly resolved. Their influence on the bigger scales is taken into account by means of empirical or semi-empirical parametric schemes.

For the investigation of the dispersion of pollutants in urban areas it is necessary to use resolutions on the order of a few meters, in order to reproduce the atmospheric flows in a specified road or square; this kind of models are called urban scale models. The horizontal dimension of the domain varies from tens of meters to a few kilometers. These models can be divided into two main categories: CFD (Computational Fluid Dynamics), based on the explicit resolution of the balance equations and fully parametric models, based on a semi-empirical description of the effects of the buildings.

2.2 Lateral Boundary conditions

Mesoscale studies make use of the assimilation of the initial and boundary conditions from a global scale model; boundary conditions are generally updated with a time frequency of six hours. To avoid the generation of unphysical gradient at the boundaries, which might cause numerical instabilities, a relaxation zone of 4 - 5 cells is embedded where the value of the variables is obtained as a weighted average between the assimilated value and the value computed by the model.

Meteorological models are used for idealized investigations too; in this case the boundary conditions are arbitrarily assigned depending on the specific phenomena to be reproduced. The value assumed by the variables at the boundaries is then specified by functions of time and space. In the following the most widely used types of idealized boundary conditions will be briefly discussed.

- **Periodic**
  The generic variable ψ is forced to assume the same value at the opposed extremes of the domain:

  $$\psi(x,0)=\psi(x,L_y) \tag{2.1}$$

  for south and north boundaries;

  $$\psi(0,y)=\psi(L_x,y) \tag{2.2}$$

  for west and east boundaries. L_x and L_y represent, respectively, the length of the domain along x and y. This kind of boundary condition is used for the domains that present homogeneity at least along one of the horizontal coordinate axis, since it reproduces an infinite domain in that direction.

- **Symmetric, antisymmetric or wall**
  Additional cells are introduced, generally three or four, outside of the boundary and the values of the generic variable ψ at the same distance from the boundary are forced to be the same, i.e. for the west and east boundaries:

  $$\psi(x_b\text{-}x,y)=\psi(x_b\text{+}x,y) \tag{2.3}$$

  where the position of the boundary x_b is 0 for the west boundary and L_x for the east boundary. For the velocity component normal to the considered boundary $u_\perp$, an antisymmetric condition is usually imposed, with null values on the considered boundary and of opposite sign outside of it:

  $$u_\perp(x_b\text{-}x)=\text{-}u_\perp(x_b\text{+}x) \tag{2.4}$$

  Conditions for the south and north boundary are defined in the same way.

  From the above definitions, it is evident that every perturbation which propagates toward the boundaries is entirely reflected back into the domain; if these perturbations and the associated reflections would assume a particular relevance, the solution would be strongly affected by the presence

of the boundaries even in the middle of the domain. For this reason this kind of boundary conditions are also called wall boundary conditions.

- **Radiation or open**

  The aim of this kind of conditions is to allow the perturbations propagating toward the boundaries to cross them, thus reducing (virtually eliminating) the reflections. This is obtained substituting, in the nodes located on the boundaries, the momentum balance equation for the normal component of velocity with the relation:

  $$\frac{\partial u_\perp}{\partial t} + c_f \frac{\partial u_\perp}{\partial x} = 0 \qquad (2.5)$$

  which states that the perturbation of $u_\perp$ would cross the boundary with a phase speed c_f. The remaining variables are kept equal to their original values; an alternative is to impose their gradients along the direction normal to the boundary are zero.

  The key for a strong reduction of the reflections is a correct choice for c_f; a number of methods have been proposed in literature for the determination of this parameter. Orlanski (1976) assumes that it is possible to measure the phase speed of the outgoing perturbations just before they reach the boundary; the solution at time t - 1 in the cell preceding the boundary is then used to compute c_f:

  $$c_f = -\left(\frac{\partial u_\perp}{\partial t} \bigg/ \frac{\partial u_\perp}{\partial x} \right)_{x_b -\Delta x, t-\Delta t} \qquad (2.6)$$

  Klemp and Wilhelmson (1978) proposed to evaluate c_f as the sum of a constant c and the speed $u_\perp$:

  $$c_f = c + u_\perp \qquad (2.7)$$

  c is the maximum value of the phase speed of the internal waves:

  $$c = \frac{N L_z}{\pi} \qquad (2.8)$$

  where N is the Brunt-Väisälä frequency and L_z is the vertical extension of the domain.

2.3   Turbulence closure for RANS models

Turbulence closures models can be organized on the basis of the maximum order of the correlations explicitly resolved and the number of transport equations introduced to model the higher order moments.

8

2.3.1 Eddy viscosity models

This class of models assumes that the characteristics of a turbulent flux are directly related to the gradients of the components of the mean velocity and temperature. Correlations of second and higher orders are modeled.

2.3.1.1 Algebraic models

The correlations for the three components of velocity fluctuations can be expressed by the symmetric second-order Reynolds tensor $\overline{u_i' u_j'}$. The simplest closure, proposed by Boussinesque, relates Reynolds tensor to the gradients of the mean velocity by a turbulent viscosity coefficient ν_T which is a specific characteristic of the flow (hypothesis of Boussinesque):

$$\overline{u_i' u_j'} = -\nu_T \left(\frac{\partial \overline{u}_i}{\partial x_j} + \frac{\partial \overline{u}_j}{\partial x_i} \right) \qquad (2.9)$$

In the kinetic theory of gases the molecular viscosity of a fluid is proportional to the product of the mean free path of a molecule times its mean velocity; similarly the turbulent viscosity can be expressed as the product of a characteristic length (which represents the dimension of the eddies responsible of the momentum transport) times a velocity scale.

The cross-correlation of velocity and potential temperature can be expressed by a first-order closure:

$$\overline{u_j' \theta'} = -K_\theta \frac{\partial \overline{\theta}}{\partial x_j} \qquad (2.10)$$

where K_θ is chosen after a calibration with atmospheric measurements.

Algebraic models use for the computation of ν_T only algebraic expressions, without any transport equation; hence they are models of order 1. The Prandtl model is one of the simplest; it assumes a turbulent current with plane geometry and the maximum gradient of velocity normal to the mean flow direction. Consider the parcel of fluid being translated, by the effect of turbulence, of a distance l_m from its original position along the direction of the mean gradient. The conservation of momentum allows approximating the variation of velocity of the parcel by a Taylor expansion:

$$u' = l_m \frac{\partial \overline{u}}{\partial z} \qquad (2.11)$$

where $\overline{u}$ is the mean velocity. The components of the diagonal of the Reynolds tensor $\overline{u_i'^2}$ can be expressed by:

$$\overline{u_i'^2} = l_m^2 \left(\frac{\partial \overline{u}}{\partial z} \right)^2 \qquad (2.12)$$

If we assume the proportionality between $\overline{u_i' u_j'}$ and $\overline{u_i'^2}$, then:

$$\overline{u_i'u_j'} = -\nu_T \frac{\partial \overline{u}}{\partial z} \approx l_m^2 \left| \frac{\partial \overline{u}}{\partial z} \right| \frac{\partial \overline{u}}{\partial z} \tag{2.13}$$

and:

$$\nu_T \approx l_m^2 \left| \frac{\partial \overline{u}}{\partial z} \right| \tag{2.14}$$

In the viscous sublayer the dimensions of the eddies are limited by the presence of the ground and the mixing length l_m is given by:

$$l_m = kz \tag{2.15}$$

where $k = 0.4$ is the von Kármán constant.

Above the viscous sublayer l_m is given by:

$$l_m = c\delta \tanh\left(\frac{k}{c} \frac{z}{\delta} \right) \tag{2.16}$$

where $c \cong 0.085$ is an empirical constant and δ is the boundary layer thickness.

2.3.1.2 One-equation models

These models are based on the definition of the scale velocity as a function of the turbulent kinetic energy (TKE) $\overline{q}$; an additional transport equation is then solved:

$$\frac{D\overline{q}}{Dt} = P_{tur} + G_{tur} + T_{tur} - \varepsilon \tag{2.17}$$

- The production term P_{tur} is related to the transfer of energy from the mean flow to the turbulent fluctuations:

$$P_{tur} = -\overline{u_i'u_j'} \frac{\partial \overline{u}_i}{\partial x_j} \tag{2.18}$$

- The production term G_{tur} expresses the variation of kinetic energy due to buoyancy forces:

$$G_{tur} = \frac{g}{\theta_0} \overline{\theta' u_i'} \delta_{3i} \tag{2.19}$$

- The transport term T_{tur} can be written in divergence form:

$$T_{tur} = \frac{\partial}{\partial x_j} \left(\underbrace{-\overline{\overline{q}u_j'}}_{I} - \underbrace{\frac{1}{\rho_0} \overline{p'u_i'}}_{II} + \underbrace{\nu \frac{\partial \overline{q}}{\partial x_j}}_{III} \right) \tag{2.20}$$

T_{tur} contains the contributions to the redistribution of turbulence energy by velocity fluctuations (I) and by pressure fluctuations (II); furthermore, in proximity of the walls the transport is also influenced by molecular viscosity effects (III).

- The dissipation ε is given by:

$$\varepsilon = \nu \overline{\left(\frac{\partial u_i'}{\partial x_j} \right)^2} \qquad (2.21)$$

This term represents viscous dissipative phenomena active at the small scales.

Equation (2.17) represents the transfer of energy from the larger to the smaller scales, according to the Kolmogorov theory. The turbulent kinetic energy associated to the dissipative scales, neglecting the contribution from the transfer of energy toward the larger scales (inverse cascade), is a function of the rate of dissipation ε and the integral length scale L_f only. The dimensional analysis gives:

$$\left[\overline{q} \right] = \left[\varepsilon^\alpha L_f^\beta \right] = \left[\frac{L^2}{t^2} \right] = \left(\frac{L^2}{t^3} \right)^\alpha L^\beta \qquad (2.22)$$

$$\overline{q} = \left(\varepsilon L_f \right)^{\frac{2}{3}} \qquad (2.23)$$

Hence ε can be expressed by the closing relation:

$$\varepsilon = \overline{q}^{\frac{3}{2}} \Big/ L_f \qquad (2.24)$$

The term T_{tur}, neglecting the transport due to molecular viscosity effects, can be modeled by a gradient diffusion approach:

$$T_{tur} = \frac{\nu_T \rho}{Pr} \frac{\partial \overline{q}}{\partial x_j} \qquad (2.25)$$

Prandtl number is generally assumed to be 1 in atmosphere.

The eddy viscosity coefficient is then given by:

$$\nu_T = \sqrt{\overline{q}} L_\mu \qquad (2.26)$$

The one-equation models assume that the length scales L_μ and L_f are proportional and given by:

$$L_\mu = \sqrt{2a_1} kz \qquad (2.27)$$

$$L_f = \left(2a_1 \right)^{-\frac{3}{2}} kz \qquad (2.28)$$

where $a_1 = 0.15$, determined by a comparison with atmospheric measurements.

The cross-correlation $\overline{u_j'\theta'}$ is given by (2.10), where K_θ is assumed to be proportional to the eddy viscosity coefficient:

$$K_\theta = \frac{\nu_T}{Pr} \qquad (2.29)$$

2.3.1.3 Two-equation models

This category introduces, along with the turbulent kinetic energy equation, an additional transport equation for the scale turbulent variable Ψ:

$$\frac{D\Psi}{Dt} = \left[c_{\Psi 1} \left(-\overline{u'_i u'_j} \frac{\partial \overline{u}_i}{\partial x_j} \right) + c_{\Psi 2} \left(\frac{g}{\theta_0} \overline{\theta' u'_k} \delta_{3k} \right) + c_{\Psi 3} \overline{q} \frac{\partial \overline{u}_k}{\partial x_k} - c_{\Psi 4} \varepsilon \right] \frac{\Psi}{\overline{q}} + \frac{\partial}{\partial x_j} \left(\rho \frac{\nu_T}{\sigma_\Psi} \frac{\partial \Psi}{\partial x_j} \right)$$

(2.30)

where $c_{\Psi i}$ are empirical coefficients to be determined on the basis of experimental measurements. σ_Ψ is the turbulent Prandtl/Schmidt number for the variable Ψ; the meaning of this parameter changes whether the thermal diffusivity (Prandtl number $Pr = \frac{\nu}{\kappa}$, with ν kinematic viscosity and κ thermal diffusivity) or the molecular diffusivity (Schmidt number $Sc = \frac{\nu}{D}$, with D molecular diffusivity) prevails.

The main reasons upon which the scale turbulent variable is chosen are:

- ability to solve directly the equation of transport for characteristic turbulent scale variable;
- the scale variable should be chosen in order that its boundary conditions can be easily specified.

The most widely used two-equation model consider the turbulent kinetic energy dissipation term ε as the additional scale variable; hence this model is called k-ε, from the original nomenclature that called k the turbulent kinetic energy.

The transport equation for ε is:

$$\frac{D\varepsilon}{Dt} = \left[c_{\varepsilon 1} \left(-\overline{u'_i u'_j} \frac{\partial \overline{u}_i}{\partial x_j} \right) + c_{\varepsilon 2} \left(\frac{g}{\theta_0} \overline{\theta' u'_k} \delta_{3k} \right) + c_{\varepsilon 3} \overline{q} \frac{\partial \overline{u}_k}{\partial x_k} - c_{\varepsilon 4} \varepsilon \right] \frac{\varepsilon}{\overline{q}} + \frac{\partial}{\partial x_j} \left(\rho \frac{\nu_T}{\sigma_\varepsilon} \frac{\partial \varepsilon}{\partial x_j} \right)$$

(2.31)

where $c_{\varepsilon 1} = 1.44$, $c_{\varepsilon 2} = 0.8$, $c_{\varepsilon 3} = 0.33$, $c_{\varepsilon 4} = 1.92$, $\sigma_\varepsilon = 1.3$. The term $\overline{w'\theta'}$ is given by (2.10).

The relation for the eddy viscosity comes from dimensional analysis:

$$\nu_T = c_\mu \frac{\overline{q}^2}{\varepsilon}$$

(2.32)

with $c_\mu = 0.09$.

The generic variable Ψ can be expressed as a function of $\overline{q}$ and ε:

$$\Psi = \overline{q}^m \varepsilon^n$$

(2.33)

The eddy viscosity can thus be expressed as a function of Ψ:

$$\nu_T = c_\mu \frac{\overline{q}^{2 + \frac{m}{n}}}{\Psi^{\frac{1}{n}}}$$

(2.34)

We can write the transport equation for the generic turbulent scale variable in the same form of (2.17):

$$\frac{D\Psi}{Dt}=\frac{D\Psi}{D\varepsilon}\frac{D\varepsilon}{Dt}+\frac{D\Psi}{D\overline{q}}\frac{D\overline{q}}{Dt}=\overline{q}^{m}n\varepsilon^{n-1}c_{\varepsilon1}P_{tur}\frac{\varepsilon}{\overline{q}}+m\overline{q}^{m-1}\varepsilon^{n}P_{tur}+....=c_{\Psi1}P_{tur}\frac{\overline{q}^{m}\varepsilon^{n}}{\overline{q}}+... \qquad (2.35)$$

The coefficients $c_{\Psi i}$ are given by:

$$c_{\Psi i}=m+nc_{\varepsilon i} \qquad (2.36)$$

Table 2.1 summarizes the main characteristics of the most widely used two-equation schemes.

Model	Ψ	Unit of Ψ
$k-\varepsilon$	ε	$\left[m^2s^{-3}\right]$
$k-\omega$	$\omega=\dfrac{\varepsilon}{\overline{q}}$	$\left[s^{-1}\right]$
$k-\tau$	$\tau=\dfrac{1}{\omega}$	$[s]$
$k-L$	$L=\dfrac{\overline{q}^{\frac{3}{2}}}{\varepsilon}$	$[m]$
$k-kL$	$kL=\overline{q}L=\dfrac{\overline{q}^{\frac{5}{2}}}{\varepsilon}$	$\left[m^3s^{-2}\right]$

Table 2.1. Two-equation models with different additional prognostic variable Ψ.

2.3.2   Reynolds-stress models

This category of models overcomes the approximation of the Boussinesque hypothesis directly solving transport equations for the components of the stress tensor $\overline{u_i'u_j'}$; only third-order and fourth-order correlations undergo modeling. The main advantage of this methodology lies on the fact that the flow is less influenced by higher order statistical moments. Since the Reynolds tensor is second-order and symmetric, six differential equations are to be solved and, consequently, the terms to be modeled increase. On one hand, this gives the opportunity to model more accurately the physics of turbulence but on the other this modeling can be very difficult for some kind of flows. Furthermore, numerical problems can arise from the strong coupling of the equations of the system and a significant amount of computational power is needed with respect to the eddy viscosity models.

2.4   Large Eddy Simulation

Turbulent fluxes are composed by coherent spatial structures whose dimensions are distributed over a wide spectrum of length scales. The larger structures are the foremost responsible for the transport processes, while the smaller scales are mainly

involved in the viscous dissipation of kinetic energy. The process can be viewed as a cascade of energy from the larger eddy structures, characterized by the integral length scale L_f, to the Kolmogorov microscale η.

This mechanism is governed by the Reynolds number, through the relation:

$$\frac{\eta}{L_f} = Re^{-\frac{3}{4}} \tag{2.37}$$

The large structures, more energetic, are characterized by a marked anisotropy and a strong dependence on the flow type; the microstructures are instead essentially independent from the boundary conditions and mostly isotropic. From (2.37), the separation between microscale and macroscale is more evident for high Reynolds numbers.

Applying the Fourier decomposition to the dependent variables in the Navier-Stokes equations it is possible to analyze the spectral density of the turbulent kinetic energy E as a function of the wavenumber k (Fig. 2.2). Higher wavenumbers correspond to smaller structures. It is evident that lower energy content is associated to the smaller structures. The region of the spectrum with an approximately linear shape, called inertial subrange, divides the dissipative microstructures from the large eddies connected to turbulent transport; in this range of wavenumbers the energy flux toward the Kolmogorov microscale equals the dissipation rate ε. The Kolmogorov theory predicts for the energy spectral density the relation:

$$E(k) = \alpha \varepsilon^{\frac{2}{3}} k^{-\frac{5}{3}} \tag{2.38}$$

where $\alpha = 1.5$.
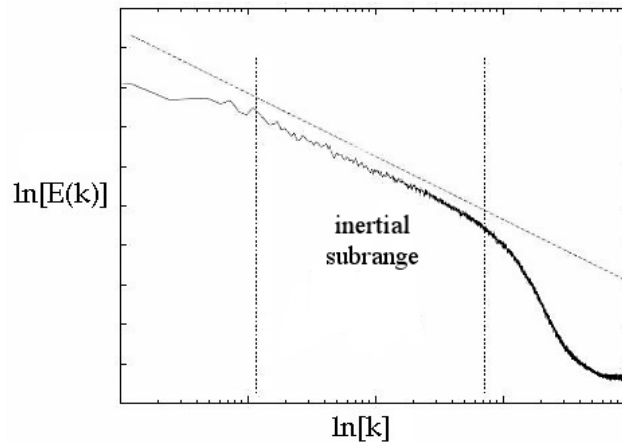
Fig. 2.2. Turbulent kinetic energy spectral density: the -5/3 linear slope in the log-log plot delineates the inertial subrange.

The LES methodology relies on the explicit resolution of the governing equations only for the structures larger than a chosen dimension; the influence of the smaller subgrid scales on the resolved field is modeled. The separation between resolved

14

and subgrid scales results from the application of a low-pass filter (Nieuwstadt 1990). The generic variable $f(\mathbf{x},t)$ is thus decomposed in a filtered component $\overline{f}(\mathbf{x},t)$ and a residual. The filtering operation can be expressed mathematically by the convolution between the variable and the filter $G(\mathbf{x}-\xi,\Lambda)$:

$$\overline{f}(\mathbf{x},t) = \int_{-\infty}^{+\infty} G(\mathbf{x}-\xi,\Lambda)f(\xi,t)d\xi \tag{2.39}$$

where Λ is the filter width.

The most widely used filter types are:

–   box or top hat:

$$G(x\text{-}\xi,\Lambda) = \begin{cases} \dfrac{1}{\Lambda^3} & , \quad |x\text{-}\xi| \le \dfrac{\Lambda}{2} \\ 0 & , \quad \text{altrove} \end{cases} \tag{2.40}$$

–   sharp cutoff, defined in Fourier space:

$$G(k,\Lambda) = \begin{cases} 1 & , \quad k \le \dfrac{\pi}{\Lambda} \\ 0 & , \quad \text{altrove} \end{cases} \tag{2.41}$$

–   gaussian, defined in Fourier space:

$$G(k,\Lambda) = e^{-\frac{\Lambda^2 k^2}{4}} \tag{2.42}$$

The filters can be represented both in the physical and in the Fourier space (Fig. 2.3).
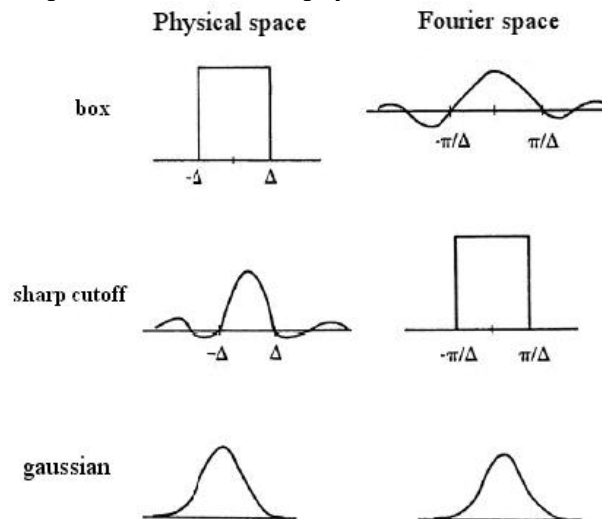
Fig. 2.3. Representation of different filters for the LES in physical and Fourier spaces.

For a compressible fluid it is convenient to decompose the turbulent variables, based on Favre filtering (Erlebacher et al. 1992):

$$f(\mathbf{x},t)=\tilde{f}(\mathbf{x},t)+f'(\mathbf{x},t) \tag{2.43}$$

The Favre filter is defined by:

$$\tilde{f}=\frac{\overline{\rho f}}{\overline{\rho}} \tag{2.44}$$

where the explicit space and time dependence of the variable has been omitted.

The main difference between LES and RANS techniques relies in the fact that, while in the Reynolds decomposition the average of the fluctuating component is zero, in the LES we have:

$$\widetilde{f'}(\mathbf{x},t)\neq 0 \tag{2.45}$$

thus:

$$\tilde{\tilde{f}}(\mathbf{x},t)\neq\tilde{f}(\mathbf{x},t) \tag{2.46}$$

Neglecting Coriolis terms and taking into account the Boussinesque approximation, the filtered governing equations for dry atmosphere are:

$$\overline{p}=p_0\left(\frac{R_d\tilde{\theta}}{p_0}\right)^{\gamma} \tag{2.47}$$

$$\frac{\partial\overline{\rho}}{\partial t}+\frac{\partial(\overline{\rho}\tilde{u}_i)}{\partial x_i}=0 \tag{2.48}$$

$$\frac{\partial(\overline{\rho}\tilde{u}_i)}{\partial t}+\frac{\partial(\overline{\rho}\widetilde{\tilde{u}_i\tilde{u}_j})}{\partial x_j}=-\frac{\partial\pi}{\partial x_i}+g\beta\overline{\rho}\tilde{\theta}\delta_{i3}+\frac{\partial\tau_{ij}}{\partial x_j}+\mu\frac{\partial^2\tilde{u}_i}{\partial x_j^2}+F_i \tag{2.49}$$

$$c_p\frac{\partial(\overline{\rho}\tilde{\theta})}{\partial t}+c_p\frac{\partial(\overline{\rho}\widetilde{\tilde{u}_j\tilde{\theta}})}{\partial x_j}=c_p\frac{\partial h_j}{\partial x_j}+\kappa\frac{\partial^2\tilde{\theta}}{\partial x_j^2}+F_\theta \tag{2.50}$$

where δ_{ij} is the Kronecker operator, p_0 is the reference pressure, $R_d = 2/7c_p$ is the gas constant for dry air, $\gamma = c_p/c_v = 1.4$ is the ratio of the heat capacities for dry air, $c_p = 1004.5$ J K^{-1} Kg^{-1} is the heat capacity at constant pressure, β is the thermal expansion coefficient, κ the thermal conductivity and μ is the dynamic viscosity. The terms F_i represent momentum forcing and surface friction, F_θ is the thermal forcing. The remaining terms are defined by:

$$\pi=\overline{p}+\frac{1}{3}\eta_{kk} \tag{2.51}$$

$$\tau_{ij}=-\left(\eta_{ij}-\frac{1}{3}\eta_{kk}\delta_{ij}\right) \tag{2.52}$$

$$h_j=-\overline{\rho}\left(\widetilde{\tilde{u}_j\theta'}-\widetilde{u_j'}\tilde{\theta}-\widetilde{u_j'\theta'}\right) \tag{2.53}$$

$$\eta_{ij}=-\overline{\rho}\left(\widetilde{\tilde{u}_iu_j'}-\widetilde{u_i'}\tilde{u}_j-\widetilde{u_i'u_j'}\right) \tag{2.54}$$

The terms τ_{ij} and h_j represent the influence of the subgrid scales on the resolved field: again the above equations must be closed through parametric schemes, like for the RANS models.

It results, from the discussion above, that the main advantage of the LES methodology relies in its ability to model only the small scales. The parameterization is then easier, since the subgrid scales can be considered almost independent from the flow conditions. Furthermore, a higher energetic content is generally resolved and the influence of the subgrid contributions on the resolved scales is less important than with the RANS technique. Nevertheless, it should be noted that for the flows characterized by small scale forcings the LES technique is not efficient since in this case the subgrid scale modeling depends significantly from the flow conditions. Examples of situations where the LES is not recommended include: wall turbulence, where the small structures are highly energetic and anisotropic and turbulent combustion, where molecular diffusion and chemical reactions are important.

The choice of the filter width Λ is a fundamental step in the LES investigations. Usually this parameter is chosen to be proportional to the spatial resolution h, thus depending on the characteristics of the flow. A more rigorous method for the definition of Λ is the so-called adaptative LES (Pope 2004). The method is based on the definition of a measure $M(\mathbf{x},t)$ for the resolved turbulence, as the ratio between the subgrid scale turbulent kinetic energy $q'(\mathbf{x},t)$ and the total energy (including the resolved component $\tilde{q}(\mathbf{x},t)$):

$$M(\mathbf{x},t)=\frac{q'(\mathbf{x},t)}{\tilde{q}(\mathbf{x},t)+q'(\mathbf{x},t)} \tag{2.55}$$

For a DNS M = 0, while for a RANS M = 1; a decrease of M corresponds to an increase of the resolved energy and of the number of turbulent structures explicitly represented. Chosen a threshold value ε_M for M and a fixed $\dfrac{h}{\Lambda}$ ratio, it is possible to refine the mesh in order to have in every region of the domain:

$$M(\mathbf{x},t)\leq\varepsilon_M \tag{2.56}$$

The choice $\varepsilon_M=0.2$, for example, ensures the explicit resolution of the 80% of the turbulent kinetic energy.

2.4.1 Eddy viscosity subgrid scale models

The LES subgrid scale schemes can be grouped into two main categories: eddy viscosity models and scale similarity models. The formers assume the proportionality between the subgrid strain tensor τ_{ij} and the resolved strain tensor S_{ij}. The latter are based on the strong analogy between the contiguous scales in the wavenumber space; in this case, τ_{ij} is expressed as a function of a tensor obtained by multiple filtering of the resolved field.

We will focus only on the eddy viscosity models. The subgrid parameterization models essentially viscous dissipative phenomena; these processes can be described by a gradient diffusion approach:

$$\tau_{ij} = -2\nu_{LT}\bar{\rho}S_{ij} \tag{2.57}$$

$$h_j = \nu_{LH}\bar{\rho}\frac{\partial\tilde{\theta}}{\partial x_j} \tag{2.58}$$

with:

$$S_{ij} = \frac{1}{2}\left(\frac{\partial\tilde{u}_i}{\partial x_j} + \frac{\partial\tilde{u}_j}{\partial x_i}\right) \tag{2.59}$$

The various models differ for the expressions used for ν_{LT} and ν_{LH}.

One of the first eddy viscosity models, still widely used, was developed by Smagorinsky (1963); it assumes that the eddy viscosity coefficient ν_{LT} is proportional to the dissipation ratio ε, this being locally and instantaneously balanced by the shear production of the subgrid turbulent kinetic energy $-\tau_{ij}S_{ij}$, which is the energy transferred from the resolved to the subgrid scales. From dimensional analysis it results:

$$\nu_{LT} = C\varepsilon^{\frac{1}{3}}\Lambda^{\frac{4}{3}} \tag{2.60}$$

imposing the local equilibrium between production and dissipation:

$$\varepsilon = -\tau_{ij}S_{ij} = \nu_{LT}S^2 \tag{2.61}$$

combining (2.61) and (2.60):

$$\nu_{LT} = l^2 S \tag{2.62}$$

where $S = \sqrt{2S_{ij}S_{ij}}$. The length scale l is related to the filter width Λ, which is in turn a function of the grid cell dimensions:

$$l = C_s\Lambda \tag{2.63}$$

The non dimensional parameter $C_s = C^{\frac{3}{4}}$ is the ratio between the filter width and the characteristic dimension of the cell; its value depends on the type of the filter. For the top hat filter Nieuwstadt (1990) suggested $C_s = 0.23$.

The coefficient ν_{LH} is usually assumed proportional to the ratio between ν_{LT} and the turbulent Prandtl number:

$$\nu_{LH} = \frac{\nu_{LT}}{Pr_T} \tag{2.64}$$

The values of Pr_T in atmosphere (Eidson 1985) usually lie in the interval $\left(\frac{1}{3};\frac{1}{2}\right)$.

Smagorinsky's hypothesis of balance between shear production and dissipation is not acceptable for buoyancy-driven flows. A possible solution is to introduce an additional prognostic equation for the subgrid-scale turbulent kinetic energy e (Moeng 1984), like in the RANS one-equation models. Moeng's original formulation considered an incompressible flow; here the transport equation has been rewritten to include compressibility effects, consistently with the Favre averaging defined in (2.44):

$$\frac{\partial(\bar{\rho}e)}{\partial t}+\frac{\partial\left(\bar{\rho}e\tilde{u}_i\right)}{\partial x_i}=\bar{\rho}\left(-\widetilde{u_i'u_j'}\frac{\partial\tilde{u}_i}{\partial x_j}+\frac{g}{\theta}\widetilde{u_3'\theta'}+\frac{\partial\left[\widetilde{u_i'\left(e+p'/\rho_0\right)}\right]}{\partial x_j}-\varepsilon\right) \qquad (2.65)$$

The downgradient diffusion assumption can be used to model the pressure correlation and turbulent diffusion term:

$$\widetilde{u_i'\left(e+p'/\rho_0\right)}=-2\nu_{LT}\frac{\partial e}{\partial x_j} \qquad (2.66)$$

Neglecting the energy contribution from the inverse energy cascade we can express the dissipation ε as a function of the filter width Λ:

$$\varepsilon=\frac{C_\varepsilon e^{\frac{3}{2}}}{\Lambda} \qquad (2.67)$$

with $C_\varepsilon=1.9C_k+\dfrac{\left(0.93-1.9C_k\right)l}{\Lambda}$.

The expression for the length scale l differs for positive and negative stratification:

$$l=\begin{cases}\min\left[\Lambda\ ,\ 0.76\dfrac{\sqrt{e}}{N}\right] & \text{for}\quad N^2>0 \\ \Lambda & \text{for}\quad N^2\le 0\end{cases} \qquad (2.68)$$

where the Brunt-Vaisälä frequency is defined by $N^2=\dfrac{g}{\theta}\dfrac{\partial\theta}{\partial z}$.

The formulation (2.68) implies, for stable regimes, l < Λ near the surface, where the local potential temperature lapse rate (and hence N) is larger. This is consistent with the presence of smaller scales in the wall region (Sagaut 2006).

The turbulent viscosities ν_{LT} and ν_{LH} are modeled with:

$$\nu_{LT}=C_k l\sqrt{e};\quad \nu_{LH}=\nu_{LT}\frac{1}{Pr_t} \qquad (2.69)$$

with C_k = 0.15. The inverse turbulent Prandtl number is a function of the ratio between the length scale and the filter width:

$$\frac{1}{\text{Pr}_t} = 1 + \frac{2l}{\Lambda} \tag{2.70}$$

Near the ground, due to the importance of viscous effects, the characteristic dimensions of the eddies become smaller and their order of magnitude can be evaluated in wall units:

$$x_i^+ = \frac{x_i u_\tau}{\nu} \tag{2.71}$$

where $u_\tau = \sqrt{\dfrac{\tau_w}{\rho}}$ is the friction velocity, τ_w is the wall strain, ρ and ν are, respectively, the density and the cinematic viscosity of the fluid. The inertial subrange moves toward higher wavenumbers and, in order to resolve a significant energy content, it is necessary to use cell dimensions on the order of $\Delta x^+ \simeq 100$, $\Delta z^+ \simeq 20$; notably smaller than the discretizations that can be used far from the wall, where viscous effects are negligible and the energetic scales are larger. Also, the time step for the integration is related to the time scale of the eddies, which is inverse proportional to the spatial scale and hence to the cell dimensions. A possible solution is to refine the grid only close to the walls, for example with the vertical stretching. Anyway, for very complex geometries the computational cost remains elevated; Reynolds (1990) estimated that it can be on the order of $\text{Re}^{2.4}$.

Efficient, even if less accurate, solutions are the hybrid methods, called DES (Detached Eddy Simulation); in these models the RANS technique is used for the wall layer and the LES above a certain distance from the walls. In this case, the dimensions of the cell and the time step are large enough to retain that the effects of the turbulent structures near the ground can be taken into account statistically. Sullivan et al. (1994) proposed a criterion for the determination of the RANS/LES interface based on the ratio between the fluctuating component of the strain tensor (computed subtracting from S_{ij} its horizontal average) and its resolved part.

2.4.1.1   Filter width for anisotropic grids

If the grid is composed by a cubic mesh the filter width is equal to the sides of the cell: $\Lambda = \Delta x = \Delta y = \Delta z$. If, instead, the grid is anisotropic the filter cutoff length is not the same in each direction of the space and the subgrid stresses may significantly differ from their values obtained with an isotropic filter. Two approaches are available: 1) define a single characteristic length scale to represent the filter and 2) introduce a tensorial subgrid viscosity with different length scales for each direction. The second approach requires a considerable increase of both model complexity and computational demand. Hence we will limit the following discussion to the first approach.

The filter width in the scalar models can be expressed in the form: $\Lambda = \Lambda(\Delta x, \Delta y, \Delta z)$. The most commonly used expression is the empirical formulation proposed by Deardorff (1970), which equals Λ to the geometrical mean of the dimensions of the cell Δ:

$$\Delta=\sqrt[3]{\Delta x \Delta y \Delta z} \tag{2.72}$$

Scotti et al. (1993) have demonstrated that this definition is appropriate only for moderately anisotropic grids. Combining (2.57), (2.61) and (2.62) and approximating to the second-order moments, the dissipation ratio reads:

$$\varepsilon = l^2 \left(2 S_{ij} S_{ij} \right)^{\frac{3}{2}} \tag{2.73}$$

For an isotropic homogeneous flow the resolved second-order moments of the strain rate $S_{ij}S_{ij}$ is defined as the convolution of the Kolmogorov spectrum E(k), given by (2.38), with the filter kernel $G(\mathbf{k})$:

$$S_{ij}S_{ij} = \int E(k) \cdot G^2(\mathbf{k}) d\mathbf{k} = \varepsilon^{\frac{2}{3}} \frac{\alpha}{2\pi} \int k^{-\frac{5}{3}} \left| G(\mathbf{k}) \right|^2 d\mathbf{k} \tag{2.74}$$

where $k \equiv |\mathbf{k}|$. Substitution of (2.74) into (2.73) yields:

$$l = \left(\frac{\alpha}{2\pi} \int k^{-\frac{5}{3}} \left| G(\mathbf{k}) \right|^2 d\mathbf{k} \right)^{-\frac{3}{4}} \tag{2.75}$$

The cell aspect ratios are:

$$a_1 = \frac{\Delta_i}{\max[\Delta x, \Delta y, \Delta z]}$$
$$a_2 = \frac{\Delta_k}{\max[\Delta x, \Delta y, \Delta z]} \tag{2.76}$$

Δ_i and Δ_k are the lengths of the two smaller sides of the cell. For example, if max[Δx, Δy, Δz] = Δz, then $a_1 = \Delta x/\Delta z$ and $a_1 = \Delta y/\Delta z$.

In the case of a sheet-like grid ($\Delta z \ll \Delta x \simeq \Delta y$), considering a sharp cutoff filter, the integral of (2.75) tends to a constant: $l \simeq 0.1\Delta a_1^{-1/3}$. Taking into account (2.63), it is evident that Deardorff's definition (2.72) underestimates the Smagorinsky constant C_s for highly anisotropic grids. The reason is that, even if the filter is almost 2D for a sheet-like cell, the fine scales are significantly weakened in the direction of the smaller side too. A similar result can be obtained for pencil-like grids ($\Delta z \simeq \Delta y \ll \Delta x$).

On the basis of the above discussion, the authors proposed a modification of Deardorff's expression by a function f(a_1, a_2) which takes into account grid anisotropy.

$$\Lambda = f\Delta \tag{2.77}$$

The expression for f(a_1, a_2) is obtained by a numerical evaluation of (2.75):

$$f = \cosh \sqrt{\frac{4}{27}\left[\left(\ln a_1\right)^2 - \left(\ln a_1\right)\left(\ln a_2\right) + \left(\ln a_2\right)^2\right]} \qquad (2.78)$$

This formulation results in an increase of the filter width (and hence the eddy viscosity) in the zones of the domain where the aspect ratios are smaller.

3   Thermally driven circulations over complex terrain

3.1   Baroclinic instability

Atmospheric circulation in mountainous areas under weak synoptic conditions is mainly characterized by slope and valley winds (Simpson 1994). The slope wind system is driven by the horizontal temperature gradient between the air near the slope and that at some hundreds of meters from the slope at the same height, while the valley wind circulation results from the temperature difference between the air within the valley and that over an adjacent plain. These gradients are generated by the solar shortwave heating during the day and the radiative longwave cooling at the ground during the night. The resulting pressure gradient force drives an air flow from the regions of low temperature toward those of high temperature near the ground and a compensating return motion in the upper part of the atmosphere. The overall circulation is then determined by baroclinicity and characterized by vorticity, as can be viewed applying the Bjerknes theorem. The same mechanism is common for all thermally driven local systems such as the sea and land breezes, or flows due to the urban heat island effect (Martin 2006).

We define the circulation Γ as the line integral of the velocity $\mathbf{u}$ along a closed path L; the Stokes theorem allows to express Γ as the vorticity flux trough an open simply connected surface A bounded by L. Taking the lagrangian derivative of Γ, considering a material line $\mathbf{l}$ and taking into account the Helmoltz theorem, we have:

$$\frac{D\Gamma}{Dt} = \oint_L \left(\frac{1}{3} v\nabla(\nabla \cdot \mathbf{u}) + v\nabla^2\mathbf{u} \right) d\mathbf{l} + \int_A \left(\frac{\nabla\rho \times \nabla p}{\rho^2} \right) \mathbf{n} dA \qquad (3.1)$$

where we have introduced the Navier-Stokes equation for a viscous fluid and considered that mass forces are perfect differentials and thus give no contribution to the circulation. Also, since we are interested in fine mesoscale phenomena, the Coriolis terms have been neglected. The term $\dfrac{D\Gamma}{Dt}$ is an angular acceleration and thus describes the rotational characteristic of the flow. The baroclinic vector $\dfrac{\nabla\rho \times \nabla p}{\rho^2}$ is zero only for barotropic flows, where pressure and density gradients are parallel. The line integral at the right hand side of (3.1) accounts for the viscous dissipation effects, which reduce the circulation. Hence, for an inviscid barotropic flow the

circulation is constant. For a baroclinic flow density is a function of both pressure and temperature:

$$\rho = \rho(p,T) \tag{3.2}$$

thus pressure gradient is not parallel to density gradient.

In order to evaluate the contribution of the baroclinic term to the circulation, it is convenient to rewrite the area integral at the right hand side of (3.1) as a line integral:

$$\int_A \left(\frac{\nabla\rho \times \nabla p}{\rho^2} \right) \mathbf{n}\,dA = \oint_L \left(-\frac{1}{\rho}\nabla p \right) d\mathbf{l} \tag{3.3}$$

which, again, results from the application of the Stokes theorem.
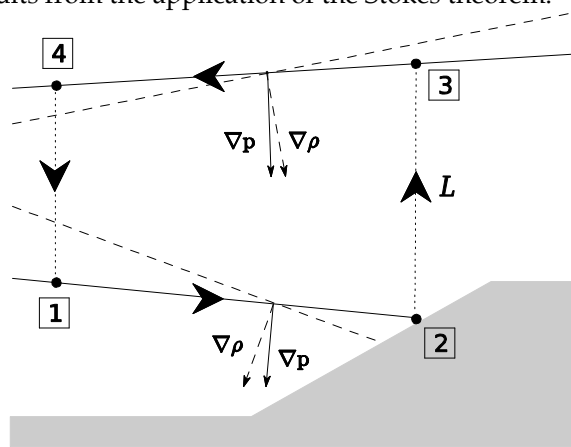
Fig. 3.1. Evaluation of the baroclinic term along a closed path L **over a finite slope: the solid lines represent the isobars and the dashed lines are the isopycnals.**

Fig. 3.1 illustrates the circulation tendency around the closed loop 1-2-3-4 over a finite slope; the solid and dashed lines represent, respectively the isobars and the isopycnals. The segments 1-2 and 3-4 give no contribution to the circulation since they are isobaric surfaces. Moving from 2 to 3 ∇p is negative, thus its contribution to the integral is positive. From 4 to 1 ∇p is positive and its contribution to the integral is negative. Since ρ appears in the denominator of the baroclinic term and the average density in the section 2-3 is less than that of the segment 4-1, the net contribution is positive. Therefore, the line integral assumes a positive sign and we obtain an increase of the counterclockwise circulation along the path L. The baroclinic circulation acts to reduce density gradients, carrying lighter air toward low pressure zones and heavier air toward high pressure zones. The result is a tilt of the isopycnals into an orientation in which they are closer parallel with the isobars; that is, the circulation represents a tendency to gain the barotropic state, converting the potential energy associated to the horizontal density gradient into the kinetic

energy of the local wind system. The baroclinic circulation also lowers the barycentre of the entire flow system and hence reduces the overall potential energy.

3.2 Mountain wind systems

Typical speed values of slope currents range from 0.5 m/s for low intensity anabatic winds to more than 10 m/s for fast katabatic flows in regions with a significant snow or ice cover over long (tens of kilometers) slopes (Monti et al. 2002; Pettré and André 1991). While the depth of the anabatic current can easily exceed 500 m (Reuten et al. 2005), the katabatic wind is characterized by a vertical extension ranging from 5–30 m in midlatitude climates to more than 100 m over long slopes in polar regions. In the evening and in the early morning the temperature gradients tend to disappear and the resulting circulation intensity is consequently strongly reduced, creating a critical situation for the dispersion of pollutants. Therefore, these wind systems have a great influence on the air quality of inhabited mountain areas, since they can enhance ventilation within the valley atmosphere favoring the dilution of pollutants. Furthermore, they modify the stability profiles, which are crucial for the dispersion properties of the atmosphere. Such currents also play an important role in the formation of clouds, favoring the uplift of moist air masses above the lifting condensation level. Another important issue is that slope and valley winds, like other local circulation systems, play an important role in redistributing energy from the local to the regional scale (Noppel and Fiedler 2002). Since this effect can be of the same order as the parameterized surface turbulent exchange in GCMs but is not usually taken into account, the investigation of these wind systems is of great interest for the development of better parameterizations for the GCMs.

One of the first theoretical works on slope flows was developed by Prandtl (1952), who assumed a steady, two dimensional, constant viscosity flow in a thermally stratified fluid with a constant lapse rate. The transport mechanism which generates the flow derives from a balance between the divergence of heat flux perpendicular to the slope and the advective transport along the slope (simplified heat budget equation), together with a balance between buoyancy and friction (simplified momentum equation). According to this model, the maximum wind speed is not dependent on the slope angle; the influence of this parameter is limited to the vertical extent of the anabatic current. Manins and Sawford (1979) (in the following named MS) presented a hydraulic model of katabatic winds which, assuming stationarity, can be used to predict the flow depth h as a function of the distance along the slope:

$$h = \frac{3}{4} E_c s \qquad (3.4)$$

where s is the distance from the top of the slope. The entrainment coefficient E_c is given by Briggs' (1981) semi empirical relationship: $E_c = 0.05 \left(\sin\beta \right)^{2/3}$, where β is the slope steepness.

Ye et al. (1987) proposed a revision of Prandtl's theory for a turbulent upslope flow and concluded that the maximum intensity of the wind is not dependent on the

background atmospheric stability. Instead it depends linearly on the surface heat flux and on the slope angle. Hunt et al. (2003) (in the following named HU) used a bulk approach to describe the unsteady anabatic flow over a slope, subdividing the vertical domain into three zones where different flow situations are likely to occur: a surface layer with prevailing frictional effects, a middle layer where turbulent mixing dominates and an inversion layer controlled by buoyancy and inertial forces. They derived a linear expression for the mean velocity of the middle layer of the anabatic current:

$$U_m = \lambda w_* \beta^{1/3} \tag{3.5}$$

with:

- $w_* = \left(\dfrac{gQ_s h}{\theta_s} \right)^{\frac{1}{3}}$ convective velocity scale;

- λ parameter dependent from the surface roughness and the PBL depth;

- $Q_s = \overline{w'\theta'}_s$ surface kinematic heat flux;

- θ_s surface temperature over the slope.

It should be observed that all theoretical models developed for slope winds implicitly assume "quasi-hydrostatic" equilibrium (Mahrt 1982; Haiden 2003). That is, vertical accelerations in the momentum balance equation are considered negligible with respect to the buoyancy term. This assumption is valid if the slope boundary layer is shallow compared to the radius of curvature of the orography profile and fails for very steep slopes or abrupt changes of terrain inclination.

Many authors have measured the circulation over complex terrain during field studies. Brehm and Freytag (1982) analyzed the mass transport and the temperature structure in the Inn valley (Austria) and pointed out the importance of subsidence motions and entrainment from the free atmosphere associated with the return flow. These phenomena, along with the reduced volume with respect to a plain geometry, are the main reasons for the enhanced diurnal warming of the air volume in a valley. Kondo et al. (1989) measured the heat budgets in a basin under nighttime stable conditions and daytime convective regime, also evaluating the development of the cold pool during the night; they emphasized the importance of subsidence in lowering the convective boundary layer. Princevac et al. (2001) briefly reports measurements of the HU constant λ taken during the Vertical Transport and Mixing (VTMX) field campaign, conducted in Salt Lake City (Utah). Princevac and Fernando (2005), Princevac et al. (2008), Lee et al. (2006) and Monti et al. (2002) used data from the VTMX campaign to investigate the nighttime circulation, also computing the calibration parameters for the MS model. They pointed out the importance of the entrainment at low Richardson numbers and the development of along-slope periodic oscillations as the stability of flow increases during the night. Lee et al. (2006) used the VTMX measurements to implement and test a new PBL parameterization scheme based on a stability dependent turbulent Prandtl number.

The study by Monti et al. (2002) also includes an investigation of the different waves which can develop at the interface between the upslope flow and the return current, as a function of the stability of the flow, evaluated via the gradient Richardson number $Ri_g = \dfrac{g}{\theta} \dfrac{\dfrac{\overline{\partial \theta}}{\partial z}}{\left(\dfrac{\partial u}{\partial z}\right)^2 + \left(\dfrac{\partial v}{\partial z}\right)^2}$. Haiden and Whiteman (2005) analyzed wind and potential temperature data from a tethered-balloon field campaign, finding that the local equilibrium assumption on the base of the Prandtl model is not verified for weak stratifications. Reuten et al. (2005) investigated the flow pattern in the Fraser Valley (Canada) pointing out that the anabatic wind and the return current may exhibit equal velocity and vertical extension for valleys with steep slopes.

Laboratory scale studies with simplified geometries were performed in order to validate theoretical and numerical models. Deardorff and Willis (1987) investigated the upslope flow by means of an inclined water tank heated from below, using oil parcels as a tracer. The complete daily cycle of heating and cooling was investigated by Chen et al. (1996). They used a salt-stratified water tank and two-dimensional ridge geometry. Their sensitivity analysis with respect to the background stratification confirmed a weak dependence on this parameter, as previously argued by Ye et al. (1987). Fernando et al. (2000) used a water tank with two different experimental setups, a simple variable slope and a two dimensional sinusoidal basin, to reproduce the anabatic and katabatic currents in neutral and stratified background environment. Chan (2001), by means of experiments in a thermally controlled water tank, provided calibration values for the anabatic intensity relation derived by HU. Along with their analytical model, HU presented a laboratory study of the transition between the anabatic and the katabatic current above a two dimensional valley showing the formation of a frontal structure over the slope. Cenedese et al. (2004) used a thermally controlled water tank with various background stratification values to reproduce the diurnal and nocturnal circulation over a simple slope. Calibration values for the MS and HU analytical models were also provided. A recent work by Princevac and Fernando (2007) focused on the steepness conditions leading to the onset of the anabatic flow. They used a variable simple slope and different water-glycerin solutions to obtain a relation for the critical slope angle at which the onset of the anabatic wind occurs, as a function of the Prandtl number.

Numerical modeling represents a way to extend theoretical and laboratory scale insights toward more complex situations. The pioneering work by Orville (1964) on upslope winds was based on the integration of the vorticity equation in a two dimensional domain with a simple slope of 45° and a plateau. The basic flow features, described at the beginning of this section, were captured despite the simplicity of his model. Bader and McKee (1983) analyzed the heat transfer mechanism in a valley, obtaining results in line with the observations made by Brehm and Freytag (1982). Ye et al. (1987) developed a numerical model to extend and validate their theoretical work. Segal et al. (1987) focused on the effects related to the slope orientation on upslope flows, which becomes important especially for

midlatitude winter conditions. Rampanelli et al. (2004) used the WRF model to investigate the diurnal circulation over a valley with simplified two and three dimensional geometries. The numerical resolution for this study was 1 km on the horizontal and 50 m on the vertical, which fall in the fine mesoscale range. The first LES study of the atmospheric boundary layer over a slope was performed by Schumann (1990) who assumed an unbounded homogeneous rough plane. The SGS model was based on the TKE closure, periodic conditions were imposed for the lateral boundaries and a constant and uniform heat flux was imposed at the bottom. The results showed the development of transverse convective rolls which are an indicator of a dynamical instability. Anquetin et al. (1998) investigated, by means of an LES model, the formation and breakup of the cold pool over an idealized two dimensional valley with a resolution of 200 m along the horizontal directions and a stretched grid with $75 \leq \Delta z \leq 100$ m along the vertical direction. Skyllingstad (2003) performed the first LES of a katabatic wind, focusing also (Smith and Skyllingstad 2005) on the influence of along slope steepness variations. He assumed an infinite slope with periodic lateral boundary conditions and open boundary conditions in the direction of the flow, finding a good agreement with the predictions of the MS hydraulic model. LESs of the PBL within the Riviera Valley (Switzerland) focused mainly on the mean fields of the PBL (Chow et al. 2006; Weigel et al. 2006); the heat budget is also analyzed but, due to their resolution of 150 m in the horizontal and 20 m in the vertical, results showed a significant importance of the modeled subgrid-scale components of the turbulent fluxes compared to the resolved ones. Michioka and Chow (2008) performed an LES with horizontal resolution of 25 m of the circulation in the area of Mount Tsukuba (Japan) but focused mainly on the dispersion characteristics of a passive scalar.

Most of the published LESs of the atmospheric circulation considered rather small domains with homogeneous and steady surface forcing; the complete diurnal and nocturnal cycle was not thoroughly investigated. The turbulence structure of the valley circulation, despite its relevance for environmental and wind-energy issues, has not been sufficiently studied.

When the fast katabatic current impacts the quiescent atmosphere of the valley, a hydraulic jump may form. This phenomenon is difficult to observe (Pettré and André 1991) and to reproduce with a numerical model, due to its small characteristic length and time scales. Yu and Cai (2006) managed to reproduce in their idealized simulations the basic features of this structure, like the updraft and the correlation between the velocity and the temperature fields. According to these authors further insights can be derived from a LES study of the katabatic current, which is one of the issues we address in the present investigation.

4 Large Eddy Simulation of the circulation in a valley: effects of geometry and strong capping

The complete day-night cycle of the circulation over a slope under simplified idealized boundary conditions is investigated by means of LES. The thermal forcing is given with a time-varying law for the surface temperature. A surface layer parameterization based on the Monin-Obukhov similarity theory is used as a wall layer model. The domain geometry is symmetric, having an infinitely long straight valley in the y direction. Since the depth of the katabatic flow in mid-latitude climates is limited to 5 - 30 m, we introduced a vertically stretched grid in order to obtain a finer mesh near the ground. The length scale for the calculation of eddy viscosities is modified to take into account the grid anisotropy. A pre-integration of 24 h is made in order to obtain a capping inversion over the valley. Results show that the model is able to reproduce microscale circulation dynamics driven by thermal forcing over sloping terrain. The diurnal growth of the CBL leading to the development of the anabatic wind as well as the evolution of the cold pool in the valley during the night and its interaction with the katabatic flow are shown. Waves develop at the interface between the anabatic current and the return flow. During the day, as a combined effect of the geometry and the forcing, a horizontal breeze develops directed from the middle of the valley toward the ridges. The impact of the gravity current on the quiescent atmosphere in the valley generates a weak hydraulic jump during the night.

The Chapter is arranged as follows. In Section 4.1 a short description of the WRF model and its configuration to be used for our LES study is given. The daytime and nighttime results are presented in Section 4.2 and 4.3, respectively. Section 4.4 deals with some consideration about the complete heating-cooling cycle. Section 4.5 reports some comparisons with analytical models, field observations and laboratory investigations from some of the literature works discussed in the previous Chapter. Conclusions are given in Section 4.6.

4.1 Model and experiment setup

The numerical simulations were performed using the three dimensional meteorological model WRF (in LES mode), developed by NCAR (National Center for Atmospheric Research) in cooperation with several universities and research groups. The model is based on the fully compressible non-hydrostatic Navier-Stokes equations with a terrain-following hydrostatic-pressure vertical coordinate. For a detailed description of the WRF modeling system see Skamarock et al. (2008).

Since the horizontal scales of the investigated phenomena are quite small we can neglect the Coriolis terms (Rossby number >> 1); in addition we will limit the present study to a dry atmosphere. Under these simplifications the model equations are given by (2.47) - (2.50).

Here the tilde denotes quantities averaged over the cell volume Δ^3 and the prime is used for SGS variables. To simplify the notation, we have omitted the tilde for the resolved (RES) variables and the overbar will be used instead of the tilde to denote turbulent correlations.

The turbulence energy model of Moeng (1984) with the modified transport equation (2.65) is used to model the subgrid-scale fluxes. The contributions of pressure correlations and turbulent diffusion terms (2.66) are relatively small with respect to the other terms and will be neglected.

The formulation (2.70) for the SGS turbulent Prandtl number gives $Pr_t \cong 1/3$ in neutral and unstable conditions and has an upper bound of $Pr_t = 1$ for stable regimes; this has proven to be successful in simulation of unstable to moderately stable boundary layers. However, some authors (Monti et al. 2002; Zilitinkevich et al. 2008) questioned its application for very stable regimes, since observations of nocturnal boundary layers have shown that, when Ri_g is larger than $\cong 0.1$, Pr_t can exceed unity. Axelsen and Van Dop (2009a, b) in their LES of the katabatic winds have employed an alternative formulation of the SGS Prandtl number which takes into account its dependence on Ri_g, observing that an underestimation of Pr_t generates lower surface buoyancy. Nevertheless, in the present work the imposed thermal forcing does not generate very stable regimes and the results satisfy the limit $Ri_g \cong 0.1$ (not shown), hence the current formulation for Pr_t can be retained.

The common practice is to define Λ as the geometrical mean of the dimensions of the cell $\Delta = \sqrt[3]{\Delta x \Delta y \Delta z}$ (Deardorff 1970); for cubic or moderately anisotropic grids this approach is justified. In case of highly anisotropic grids, like vertically stretched grids with small aspect ratios $\dfrac{\Delta z}{\Delta x, \Delta y} << 1$, the almost two-dimensional filtering dampens most of the fine scales in the z direction resulting in an underestimation of the constant C_k. Scotti et al. (1993) proposed a modification of the filter width Λ based on a correction function $f(a_1, a_2)$, described in Section 2.4.1.1. This modification of the length scale results, for the stretched grids, in an increase of the filter width both in the lower and in the upper part of the domain, where the aspect ratios are smaller (Fig. 4.1).
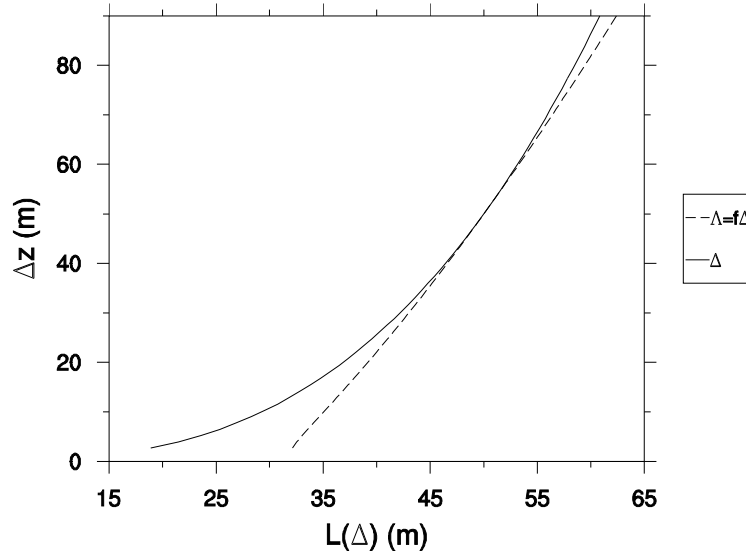
Fig. 4.1. Effect of the anisotropy correction on the filter width as a function of the vertical resolution: the solid line represent Deardorff's (1970) filter definition, dashed line is the filter with the correction proposed by Scotti et al. (1993).

Catalano et al. 2007 performed LES with the same geometry directly imposing a sinusoidal time dependence for the turbulent heat flux at the bottom boundary to provide the thermal forcing at the surface; also, the anisotropy correction was not applied and the classical definition of Deardorff was assumed. This previous formulation does not take into account the coupling between momentum and heat fluxes and the resulting differences of surface heat fluxes in zones of the domain where different flow conditions occur. This leads to deviations from the real conditions, especially during the nighttime period when in the valley the prevalent heat exchange occurs by radiative cooling and small negative values of surface heat flux are likely to occur, while over the slope high negative values are expected due to the momentum contribution on the cooling of the air.

In order to provide a more realistic boundary condition, in the present study the thermal forcing is imposed with a time-varying law for the surface temperature. A surface layer parameterization based on the Monin-Obukhov similarity theory is then used as a wall layer model to provide the surface heat flux and the friction velocity to the first layer of the grid. In the following the variables defined at the surface will be denoted by the subscript $_s$ and those defined at the first model layer by $_1$. Stability regimes and functions are determined by the bulk Richardson number

$$Ri_b = \frac{gz_1}{\theta_1} \frac{\theta_1 - \theta_s}{U_1^2}$$, following Zhang and Anthes (1982).

The domain geometry is composed of a valley, symmetric with respect to xz and $yz|_{x=\frac{L_x}{2}}$ planes, where L_x is the length of the domain along the x direction (Fig. 4.2);

the same plot also shows the four locations of the vertical profiles considered for the discussion.
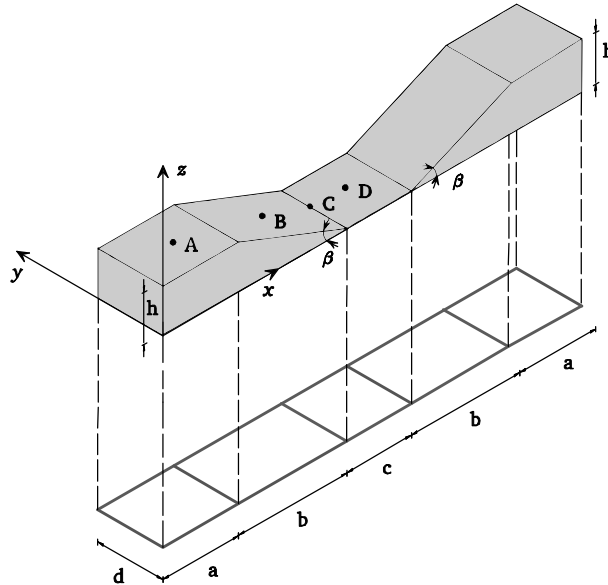
Fig. 4.2. Shape of the orography and locations of the vertical profiles (capital letters): A is located in the middle of the west ridge, B in the middle of the west slope, C at the foot of the west slope and D is in the middle of the valley.

Three simulations with different volumes of the valley and slope angles (Table 4.1) were performed in order to analyze the influence of these key parameters on the flow pattern and the distribution of the temperature. It is important to recall here that, since momentum and heat fluxes are coupled, a change in the geometry, which results in a modification of the circulation, will also result in a change of the computed surface heat fluxes.

Periodic lateral boundary conditions are assumed for the x and y directions, in order to reproduce an infinite succession of valleys and ridges along the x direction. The top boundary of the domain is assumed to be at constant pressure with zero vertical velocity. A preliminary analysis (not shown) suggested a negligible influence of gravity waves reflections on the solution, due to the presence of a capping inversion; hence an upper damping layer will not be used. The choice is supported by previous mesoscale (Rampanelli et al. 2004) and LES (Moeng et al. 2007; Antonelli and Rotunno 2007) studies of the atmospheric boundary layer conducted with the WRF model. The WRF code contains optimized algorithms for the damping of acoustic wave modes; here we set the 3D divergence damping coefficient to 0.1, the external wave filter coefficient to 0.01, and the small time step off centering coefficient to 0.1. The horizontal grid resolution is uniform, $\Delta x = \Delta y = 50$ m; the vertical grid is defined with a parabolic stretching in order to have $\Delta z \cong 2$ m near the ground and $\Delta z \cong 90$ m at the top of the domain. Table 4.2 summarizes the main parameters for the three simulations. Since the vertical coordinate is terrain following and the top of

the domain is fixed, vertical resolution slightly increases with ground elevation. For a constant and homogeneous horizontal grid we have:

$$a_1 = \frac{\Delta z}{\Delta x} \quad , \quad a_2 = 1 \quad \text{for} \quad \Delta z < \Delta x$$

$$a_1 = a_2 = \frac{\Delta x}{\Delta z} \quad \quad \text{for} \quad \Delta z > \Delta x$$

(4.1)

Hence there is a moderate increase of the filter width near the ground ($\Delta z < \Delta x$) and a slight increase close to the top of the domain ($\Delta z < \Delta x$) (Fig. 4.1).

	CASE 1	CASE 2	CASE 3
a (m)	3500	3500	3500
b (m)	5000	3000	3000
c (m)	3000	5000	1000
d (m)	3000	3000	3000
h (m)	500	500	500
H (m)	2400	2400	2400
β	≅ 5°45′	≅ 9°30′	≅ 9°30′
V_{valley} (km³)	12	12	6

Table 4.1. Domain configurations; geometry is given in Fig. 4.2. V valley is the volume of the basin.

We use a 5th order advection scheme for horizontal advection terms, 3rd order for vertical advection and a 3rd order Runge-Kutta (RK) scheme for the time integration with a time step $\Delta t = 1$ s. The integration of acoustic and gravity waves is performed using a smaller time step $\Delta t_s = \Delta t / 12$, using a time-splitting scheme incorporated into the RK loop, hence allowing for larger time steps in the RK integration.

A sinusoidal time dependence is imposed for the increments of the surface temperature $\Delta \theta_s$ with respect to the values θ_s, corresponding to the initial stratification defined by the Brunt-Vaisälä frequency N (Table 4.2):

$$\Delta \theta_s = \Delta \theta_{s,max} \sin \left[\frac{2 \pi t}{T} \right]$$

(4.2)

where $\Delta \theta_{s,max}$ is the amplitude, T = 24 h is the period and t is the time. This choice for the surface thermal forcing is supported by the observations of Monti et al. (2002), done during the VTMX campaign. For the beginning of October they reported a sinusoidal variation of the surface temperature with maximum amplitude of ≅ 5 K around the daily average.

	CASE 1	CASE 2	CASE 3
N_x, N_y, N_z:	400x60x58	360x60x58	280x60x58
Δx, Δy (m)	50		
Δz (m)	Stretched: 2 – 90		
Δt (s)	1		
$\Delta \vartheta_{s,max}$ (K)	5		
N^2 (s^{-2})	$1.6 \cdot 10^{-4}$		
z_0 (m)	0.3		
L.B.C.	Periodic x, Periodic y		

Table 4.2. Parameters of the simulations: $\Delta\theta_{s,max}$ is the amplitude of the imposed thermal forcing, N^2 is the initial Brunt-Väisälä frequency, z_0 is the surface roughness.

It should be noticed that imposing a constant surface temperature anomaly over the basin and the ridges implies neglecting the effects of the variations of the solar radiation's angle and its daytime evolution (e.g. shadowing from the surrounding terrain) and the influence of the deviation from the zenith direction. In the following, the terms west-east and south-north refer, respectively, to the orientation of x and y axes. Due to the above mentioned assumptions, there is not a real correspondence with the geographical coordinates on the earth surface.

The origin of time axis roughly corresponds to the sunrise. A pre-integration of 24 h is made in order to obtain a capping inversion over the valley.

Since both geometry and boundary conditions are independent with respect to the y direction, the mean flow can be considered two dimensional on a vertical plane and the variables are averaged along the y direction.

The simulations were run for 3 days; at the end of the first day a capping inversion forms over the valley (Fig. 4.3) as a result of the nighttime cooling. The solution is then almost cyclic after the first complete 24 hour cycle. Hereinafter we will discuss only the second day of the simulation; the time scale will then be adjusted in order to have $0 \leq t \leq 24$ h for the second daily cycle.

In the following, Case 2 will be used as the reference simulation for the analysis of the results. The stable layer at the end of the pre-integration period extends up to about 500 m with a Brunt-Väisälä frequency $N^2 = 9.8 \ast 10^{-4}$ s^{-2}.
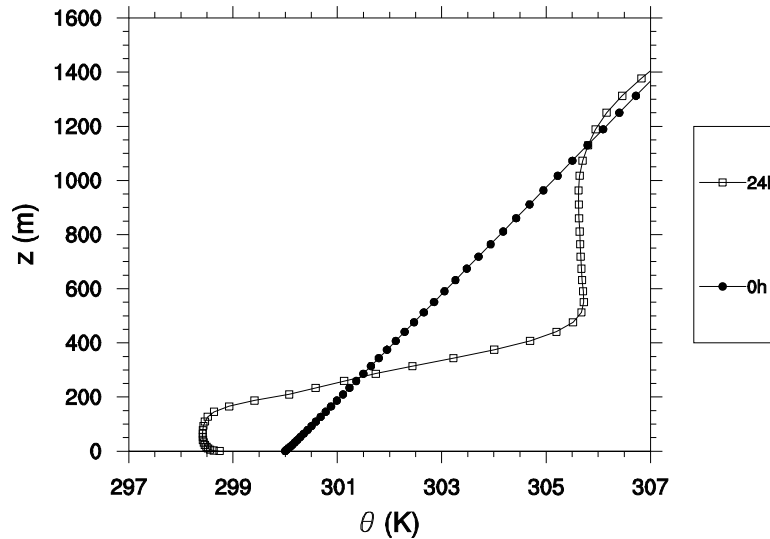
Fig. 4.3. Capping inversion as evidenced by the mean potential temperature profiles taken at point D for Case 2 for the beginning (filled circles) and the end (open squares) of the first day of simulation.

4.2 Daytime results

4.2.1 Mean winds and temperature

During the daytime period, surface heating creates horizontal potential temperature gradients (Fig. 4.4) which, in turn, lead to the development of anabatic winds over the two slopes. At t = 5 h the thermal structure is characterized by the presence of a deep ($\cong$ 800 m) mixed layer over the ridges and a shallow ($\cong$ 200 m) CBL at the bottom of the basin. This is overlied by a strongly stratified inversion layer with a vertical extension of about 200 m and a deep residual layer aloft. A significant along-slope potential temperature gradient, directed toward the ridge, is also observed. The symmetric geometry of the valley will force the circulation into a closed pattern, as can be seen from the stream function plot (Fig. 4.5). This representation was obtained after a decomposition of the wind field into spherical harmonics from which the stream function can be computed analytically by derivation (Adams and Swarztrauber 1997). Different features can be identified in the daily circulation:

- the anabatic current over the slopes, extending from the ground up to about 200m;

- a horizontal breeze directed from the center of the valley toward the slopes, extending from z $\cong$ 450 m to z $\cong$ 650 m;

- a strong updraft and an associated intense roll vortex over the ridge;

- a region characterized by a free convection regime near the east and west lateral boundaries;

- a return current in the upper part of the domain directed from the ridges toward the center of the valley with a vertical extension ranging from 600 m in proximity of the top of the slope to 250 m over the valley;

- a deep (about 800 m) subsidence region from x = 8000 m to x = 10000 m which closes the overall circulation.
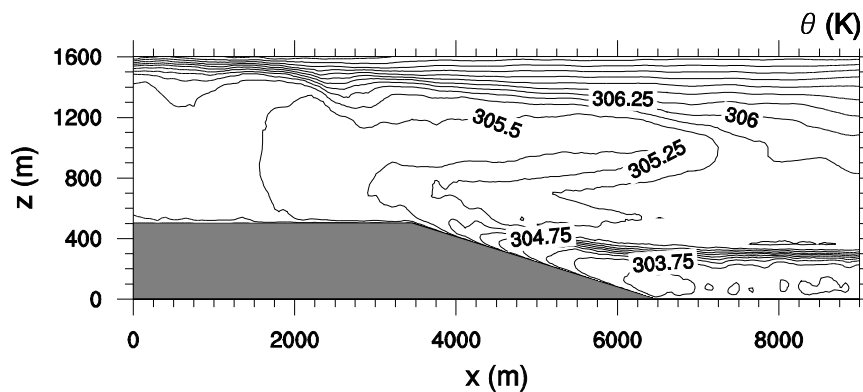
Fig. 4.4. Vertical cross section of the averaged isotherms at t = 5 h for Case 2.
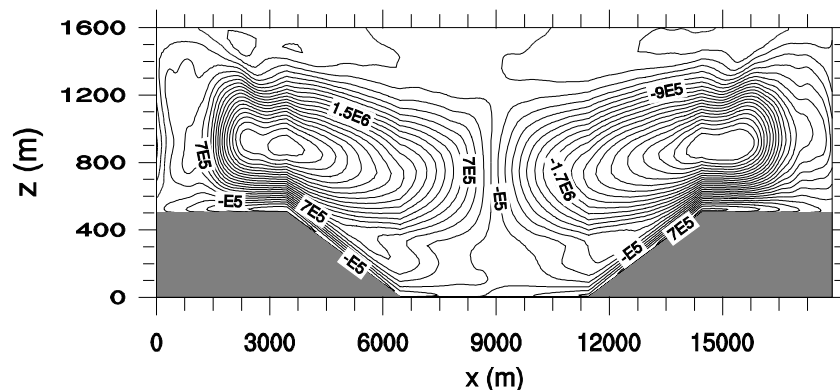
Fig. 4.5. Vertical cross section of the stream function of the mean wind field at t = 5 h for Case 2; the different components of the circulation are evidenced: the anabatic flow, the horizontal breeze at ridge height, the return current and the deep subsidence zone over the basin.

The depth of the slope current h is determined, from the vertical profiles of u, by the height where the wind speed goes below 15% of its maximum value. The maximum intensity of the upslope wind is attained, for Case 2, at t = 5 hours of simulation. At that time, when the surface temperature is increased of $\cong$ 5 K, the depth of the current continues to increase due the development of a horizontal breeze directed from the center of the valley toward the two ridges and located between 400 and 600 m. This current can be regarded as a secondary flow resulting from the layered thermal structure of the basin and can be explained considering the

mutual influence of different factors. A first mechanism is related to the interaction of the subsidence current over the valley with the strong inversion layer below; the current is then forced to flow horizontally, interacting with the anabatic wind over the slope. An important aspect for the two-layer characteristic of the anabatic flow is the stronger stratification at low levels in the valley compared to that of the region above the inversion. A second mechanism is then related to the smaller mass flux associated to the lower slope region which is characterized by a stronger potential temperature lapse rate. The large mass-flux required by the upper circulation is then partially compensated by a horizontal flux at ridge height. A significant role in this phenomenon is also played by the higher values of the surface kinematic heat flux over the two ridges compared to the lower ones at the bottom of the valley at t = 5 h (Fig. 4.6), since Q_s drives and strengthens the return current and hence the subsidence flow.
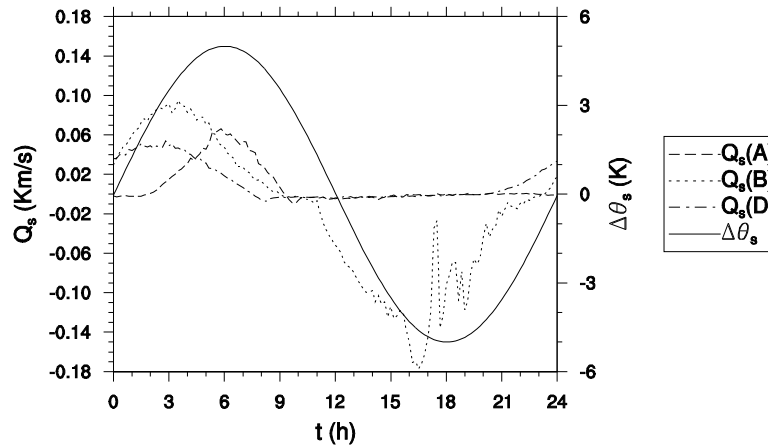
Fig. 4.6. Time evolution of the potential temperature surface anomaly $\Delta\theta$ and the averaged surface kinematic heat flux Q_s at different locations of the domain (see Fig. 4.2) for Case 2.

A simulation run with the same geometry but with a constant prescribed surface heat flux (Catalano et al. 2007) did not revealed the two-layer feature of the anabatic flow. Also, the horizontal breeze was not observed in previous investigations of the valley circulation. This might be due to stronger synoptic conditions; in fact the field measurements of Rotach et al. (2004) and the LES by Chow et al. 2006) show an upper level cross-valley wind of ~ 15 m/s. This is also confirmed by the results described in Section 5.3, relative to a simulation run with an along-valley geostrophic wind of 10 m/s.

The daytime values of the surface kinematic heat flux over the slope (point B) are about 1.5 times larger than those observed on the valley floor (point D). Q_s shows a negative phase shift with respect to the imposed temperature on the slope and the valley base; Q_s is in phase with the temperature on the ridge top. Also, the transition between positive and negative (or zero) heat flux occurs earlier on the valley ground than on the slope. The field measurements of the Riviera project (Rotach et al. 2004) showed a similar daytime evolution of Q_s for a steep symmetric Alpine valley. The authors attributed such behavior to the differences in exposure and slope angle. Instead, the similarity with the present results, which do not take

into account the solar radiation, suggests that the surface heat flux evolution is mostly influenced by the local flow conditions (through the coupling with surface momentum fluxes). This complex distribution of the surface heat flux, which is in agreement with the numerical results of Chow et al. (2006), was not observed in previous studies, conducted imposing a surface heat flux constant in space (Catalano et al. 2007). The large negative values of the surface kinematic heat flux, associated to the nighttime period, are not comparable with those reported by Rotach et al. (2004), due to a sensible difference between the arbitrarily imposed surface temperature and the values measured during the night at that site.

The anabatic flow shows a distinctive layered structure, as appears in the two distinct maxima in the vertical profiles of horizontal velocity (Fig. 4.7). Vertical layering is a typical feature of thermally driven circulations over complex terrain (Fernando et al. 2001; Reuten et al. 2005; Reuten et al. 2007) and is a consequence of the interaction of multiple spatial and temporal scales. At t = 5 h the horizontal breeze is characterized by approximately the same intensity as the anabatic wind; as the upslope current decays at t = 9 h, the horizontal breeze is three times more intense than the anabatic wind. At the foot of the slope (Fig. 4.7b) the two-layer structure of the anabatic flow is even clearer and lasts for the entire daytime period; furthermore, a weak return current is observed between the anabatic wind and the horizontal breeze at $\cong 300$ m. The intensity and depth of the upper return current are about the same in the middle of the slope and at its foot.
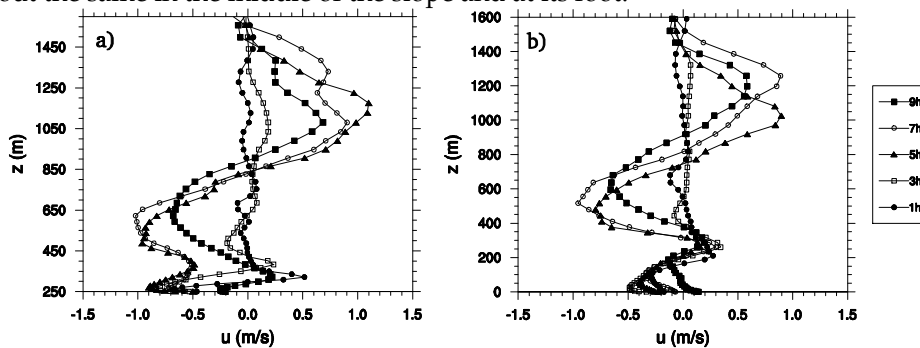
Fig. 4.7. Daytime vertical profiles of the averaged horizontal wind speed for Case 2: (a) at point B, (b) at point C.

The vertical profiles of u at t = 5 h taken at different x distances (Fig. 4.8) show that over the valley at x = 7750 m only the horizontal breeze is present; the anabatic current is very weak at x = 6500 m (about half of the strength of the horizontal breeze); at x = 5000 m the anabatic wind and the horizontal breeze have the same intensity and two different maxima can be observed; at the top of the slope (x = 3500 m) the two currents are completely merged and the wind is characterized by an intensity of 2 m/s. Due to the development of the horizontal breeze, the maximum vertical extension of the anabatic wind is reached later than its maximum intensity and is associated with a slower upslope current.
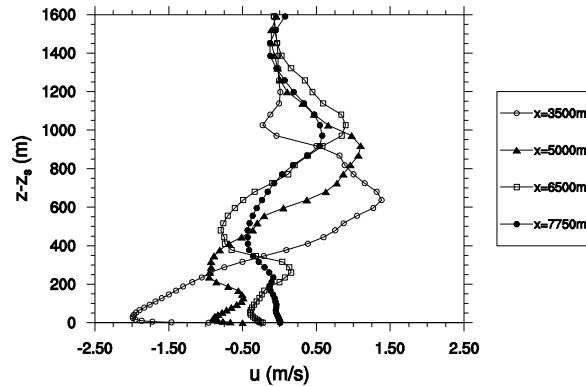
Fig. 4.8. Daytime vertical profiles of the averaged horizontal wind speed for Case 2 at different x locations at t = 5 h.

Over the ridge the stable layer developed during the night of the pre-integration period is very shallow, hence the evolution of the CBL promptly interacts with the residual layer generating a well defined mixing layer (Fig. 4.9a); over the slope and in the middle of the valley the strong stable layer is gradually eroded. Over the slope the warm air, advected by the return current of the anabatic winds enhances the erosion of the inversion layer and the residual layer above is reached at 7 h (Fig. 4.9b). In the middle of the valley the extension of the stable layer is progressively reduced by the combined effects of the subsidence above and the growing of a mixing layer below (Fig. 4.9c). Princevac and Fernando (2008) (hereinafter PF) proposed a cold pool destruction mechanism based on the relative importance of the heat flux and the stratification. According to their conceptual model, supported by laboratory measurements in a V-shaped valley, when the stratification prevails (type I), the erosion of the nocturnal inversion is mainly driven by horizontal intrusion at mid-depth of the basin. Otherwise, if the heat flux is significant compared to the stratification (type CI), the destruction of the stable core is driven by upslope advection and subsidence over the valley center. The variables which determine the prevailing inversion breakup mechanism are the buoyancy parameter $B = N^3 h^2 / (Q_s g / \theta_0)$ and the slope angle β; the intrusion dominates for values of B larger than $B_c = C\beta^{2/3}$. With the value of the empirical constant (C = 1750) suggested by PF, our results are expected to follow the type I mechanism for all the simulations, since B ~ 103 and B_c ~ 102. However, the return current in the present cases is located higher up the valley top and we did not observe any intrusion at mid-depth of the basin and the characteristics of the cold pool breakup are ascribable to type CI. This can be explained by the different geometry of PF, in particular their negligible bottom width, as mentioned by the authors themselves. This phenomenon can affect the air quality of cities in similar environments, since the pollutant will be likely to stagnate for a long time under such conditions.

The subsidence over the valley induces warming, in agreement with the measurements made by Brehm and Freytag (1982). The warming effect is more important for smaller valleys, as can be seen from the comparison of the potential temperature profiles for Cases 2 and 3 (Fig. 4.9c, Fig. 4.10).
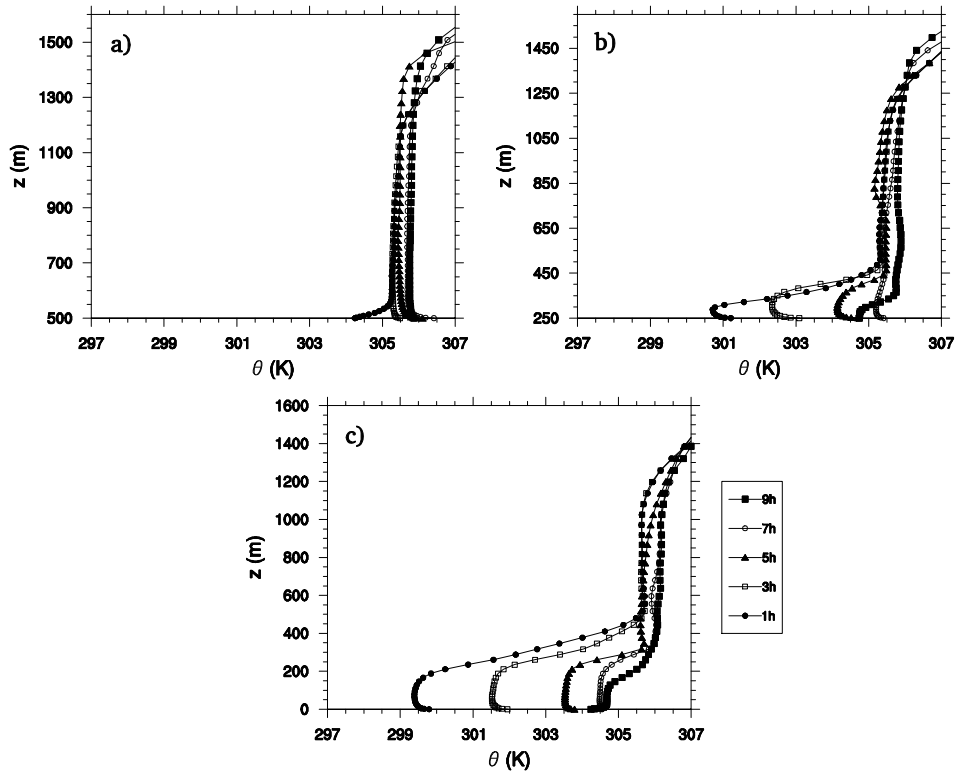
Fig. 4.9. Daytime vertical profiles of the averaged potential temperature for Case 2: (a) at point A, (b) at point B, (c) at point D.
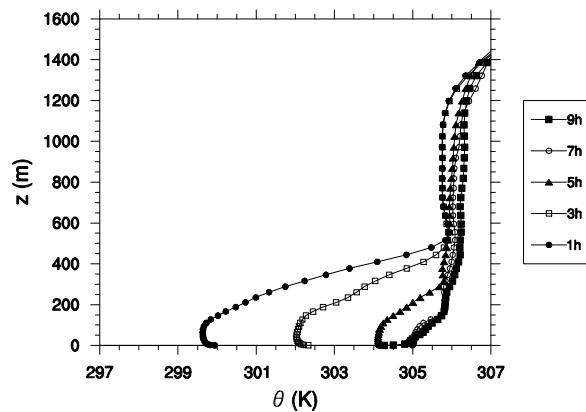
Fig. 4.10. Daytime vertical profiles of the averaged potential temperature at point D for Case 3 (smaller valley).

It is interesting to note that in Case 1, which has a gentler slope, the vertical profiles at mid depth of the valley (Fig. 4.11a) show that the anabatic current is completely merged with the horizontal breeze until 7 h, while at the foot of the slope (Fig. 4.11b) the horizontal breeze prevails. This demonstrates that the slope steepness plays a much more important role during the onset of the anabatic, in particular at the foot of the slope.
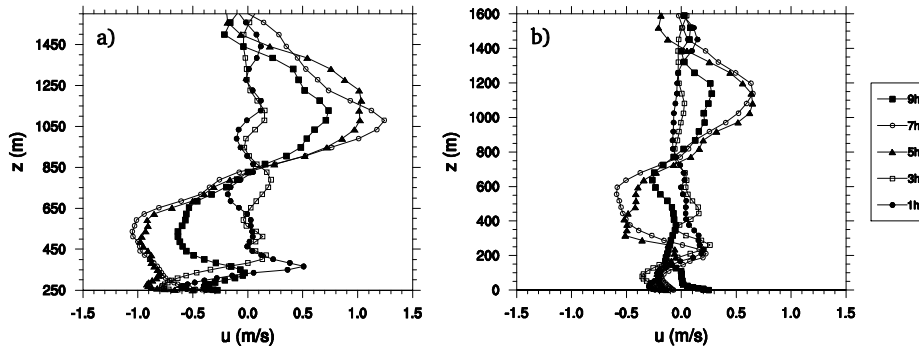
Fig. 4.11. Daytime vertical profiles of the averaged horizontal wind speed for Case 1 (gentler slope): (a) at point B, (b) at point C.

The high resolution of this LES study makes it possible to identify some characteristic microscale features of the anabatic current, like the presence of waves at the interface between the upslope current and the horizontal breeze (Fig. 4.12), resulting from the entrainment of warmer air into the anabatic current. A similar wave activity was observed by Schumann (1990) between the anabatic flow and the return current for slope angles of about 10°. In the current case, the presence of the horizontal breeze restricts larger overturning motions to the lower part of the slope ($6000 \leq x \leq 6500$ m), where a weak eastward current is observed at $\cong 300$ m (Fig. 4.7b).
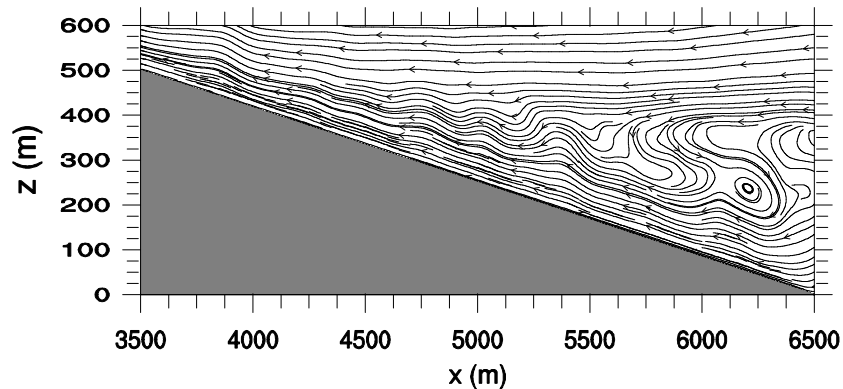
Fig. 4.12. Vertical cross-section of the streamlines of the mean flow at t = 5 h for Case 2, revealing waves at the interface between the anabatic wind and the horizontal breeze.

4.2.2   Turbulence

Most of the past LES investigations assumed horizontal homogeneity and computed the statistics as spatial averages over horizontal planes or time averages on the steady state solution. The present investigation considers time varying surface forcing and the only homogeneous direction is y, hence we will compute the averages for every (x, z) location in space. To improve the data sample, the statistics are next averaged over a 40 minutes time interval. This choice for the averaging period allows including a significant number of the characteristic timescales, as suggested by Sakai et al. (2001). As an example, at t = 5 h, the PBL depth $z_i \cong 200$ m,

w_* $\cong$ 0.81 m/s and the convective time scale $t_* = z_i/w_* = 247$ s, hence the averaging interval is $\cong$ 10 t_*.

The vertical profiles of TKE (total, resolved and subgrid scale) at t = 5 h show (Fig. 4.13) that the maximum values ($\cong$ 0.75 m^2/s^2) are attained over the ridge at z $\cong$ 700 m, due to the instabilities associated to a strong roll vortex associated to the reverse of the anabatic current and the presence of deep thermals. In the middle of the slope (Fig. 4.13b) the maximum values of TKE ($\cong$ 0.25 m^2/s^2) are located close to the surface; a second maximum is observed at z $\cong$ 1200 m, perhaps due to the shear generation at the interface between the return current and the free atmosphere. Over the valley (Fig. 4.13c), the maximum values, located $\cong$ 100 m above the ground, are about five times lower than over the ridge, whereas the very low turbulence activity in the upper layer can be explained by the weak intensity of the subsidence motions. The resolved part of TKE is the most important contribution, apart from the first levels close to the ground where the grid spacing, even with a vertically stretched grid, is still not enough to fully resolve the very fine structure of that part of the boundary layer.

The horizontal breeze determines the presence of a relative maximum of TKE in the upper part of the domain over the slope (Fig. 4.13b). This mechanism can be of great importance in the computation of the exchange coefficient in the PBL parameterizations for mesoscale or GCM models, which usually neglect orographic effects, as long as simple one-dimensional models are used.

The level where the vertical profiles of TKE go below 15% of their maximum value is used to estimate the vertical extension of the PBL. It is important to recall here that the PBL depth differs from the height of the total anabatic flow (defined in section 4.2.1), which includes the upper horizontal breeze. The maximum velocity of the anabatic wind component is located within 10 – 20% of the boundary-layer depth, while the maximum of the horizontal breeze is associated with the upper maximum in the TKE profiles.
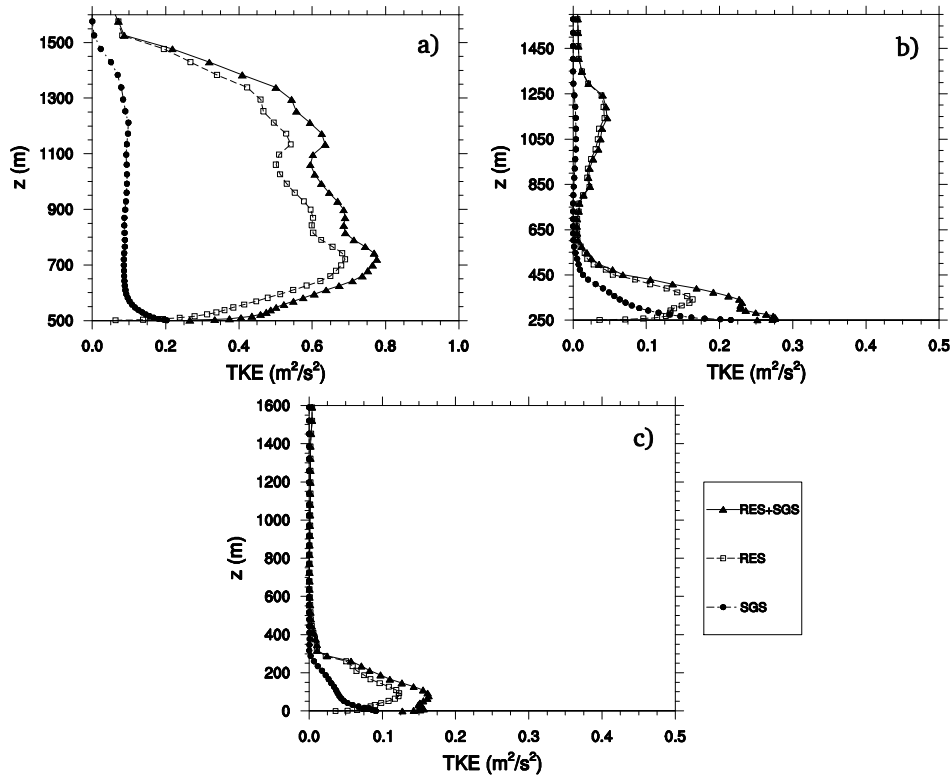
Fig. 4.13. Vertical profiles of TKE at t = 5 h for Case 2: (a) at point A, (b) at point B, (c) at point D. Open squares/ dashed lines represent the resolved contribution, filled circles/ dash-dotted lines shows the subgrid-scale contribution, filled triangles/ full lines represent the total variable.

In order to analyze the effect of the new formulation for the filter width it is convenient to examine the behavior of the simulated turbulent flow in wavenumber space. Since the vertical direction is not homogeneous we will limit the analysis to the horizontal wavenumber spectra. The one-dimensional spectra of the horizontal component of the velocity along the longitudinal wavenumber direction k_x are obtained by performing a two-dimensional Fourier transformation of the u field for a fixed vertical level and then integrating the two-dimensional periodogram along the transverse wavenumber direction k_y. Even if the flow described in this work is characterized by a marked anisotropy and inhomogeneity along the x direction, it is still possible to isolate a portion of the domain where homogeneous and isotropic conditions are approximately satisfied, like in the middle of the CBL over the valley. Furthermore, in order to reduce the inhomogeneities of the flow field being analyzed, a detrending operation is performed following Errico (1985).

On the basis of the above discussion, following Moeng and Wyngaard (1988), it is then possible to compare the one dimensional spectrum obtained for that subdomain against the theoretical -5/3 inertial subrange form of the Kolmogorov spectrum, valid for homogeneous and isotropic turbulence:

$$E(k)=\alpha\varepsilon^{2/3}k^{-5/3} \tag{4.3}$$

where $k\equiv|\mathbf{k}|=\sqrt{k_x^2+k_y^2}$ and $\alpha = 1.5$. The u component of the spectrum tensor along the k_x wavenumber has the expression:

$$\Phi_{ux}(\mathbf{k})=\frac{E(k)\left(k^2-k_x^2\right)}{4\pi k^4} \tag{4.4}$$

The truncated one-dimensional inertial range spectrum is defined as the integral of the spectrum tensor over all the wavenumbers greater than k_x:

$$E_{ux}(k_x)=2\int_{k_x}^{k_N} 2\pi k\Phi_{ux}(\mathbf{k})dk \tag{4.5}$$

where $k_N=\sqrt{\left(\frac{\pi}{\Delta x}\right)^2+\left(\frac{\pi}{\Delta y}\right)^2}$. Because of the finite upper limit in (4.5), $E_{ux}(k_x)$ differs from the log-log line with slope -5/3 for the higher wavenumbers.

Solving the finite difference equations for the system (2.48) - (2.50) on a staggered grid is equivalent (Schumann 1975) to applying a top-hat filter to the variables. Hence, in order to account for the filter type we perform a convolution operation with the top-hat filter kernel on the theoretical one dimensional Kolmogorov spectrum tensor, obtaining:

$$\tilde{E}_{ux}(k_x)=2\int_{k_x}^{k_N} 2\pi k\Phi_{ux}(\mathbf{k})\times G^2(\mathbf{k})dk \tag{4.6}$$

The filter transfer function for the two-dimensional top-hat filter kernel is:

$$G(k)=\frac{\sin\left(k_x\frac{\Delta x}{2}\right)}{k_x\frac{\Delta x}{2}}\frac{\sin\left(k_y\frac{\Delta y}{2}\right)}{k_y\frac{\Delta y}{2}} \tag{4.7}$$

44
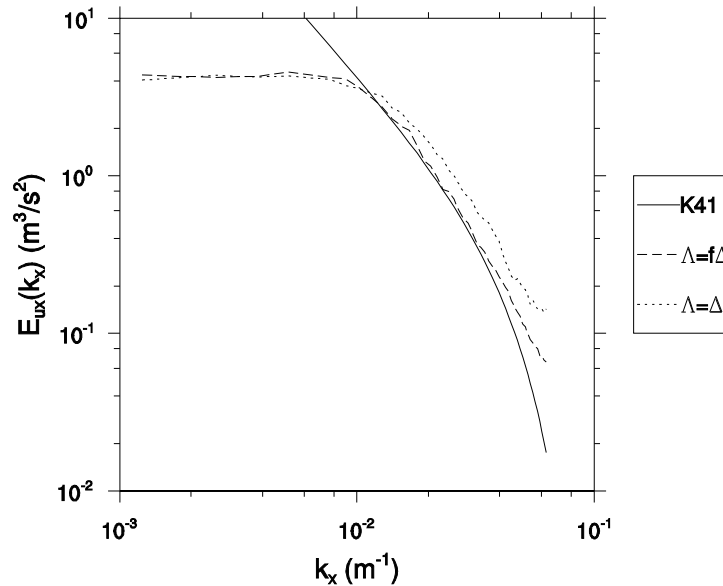
Fig. 4.14. One dimensional spectrum of the horizontal wind component over the valley core ($6500 \leq x \leq 11500$) at z - $z_s \cong 60$ m at t = 5 h for Case 2. the solid line represent the top-hat filtered theoretical Kolmogorov spectrum for isotropic and homogeneous turbulence (K41), coarse dashed line is the spectrum obtained using the filter with the correction proposed by Scotti et al. (1993), fine dashed line is the spectrum obtained using the Deardorff's (1970) filter definition.

Fig. 4.14 shows the spectrum obtained for the valley subdomain (6500 m $\leq$ x ≤ 11500 m) for level 8 of the grid (z - $z_s \cong 60$ m) at t = 5 h taken from Case 2 and from the same simulation recomputed without the anisotropy correction; both the curves are compared to the filtered truncated Kolmogorov spectrum (K41). This level has been chosen because it is located in a well mixed zone of the PBL, thus not being too close to the ground where the flow tends to be less resolved, and because the important aspect ratio of the grid at that level (~5) allows us to evaluate the influence of grid anisotropy. The spectrum obtained with the corrected length scale clearly lies closer to the theoretical curve, apart from the high wavenumber region where data seems to be slightly affected by aliasing.

4.3   Nighttime results

4.3.1   Mean winds and temperature

During the nighttime period, as the ground temperature goes down, a stable layer develops in the valley, thus eroding the residual layer just above (Fig. 4.15). The surface cooling is responsible for the development of downslope currents, flowing from the top of the two ridges. The maximum depth of the katabatic current (~20 m), determined by the sign of the vertical profiles of u, is several times lower than the vertical extent of the anabatic flow. Instead, the intensity of the downslope wind is about 2 - 2.5 times larger than the anabatic one (Fig. 4.16). Another important difference with respect to the daytime circulation is the absence of a

return current of significant intensity, in agreement with the flow measurements of Princevac et al. (2008) and the LES results of Skyllingstad (2003). The katabatic wind, in fact, can be interpreted as a low level jet in a stratified flow.
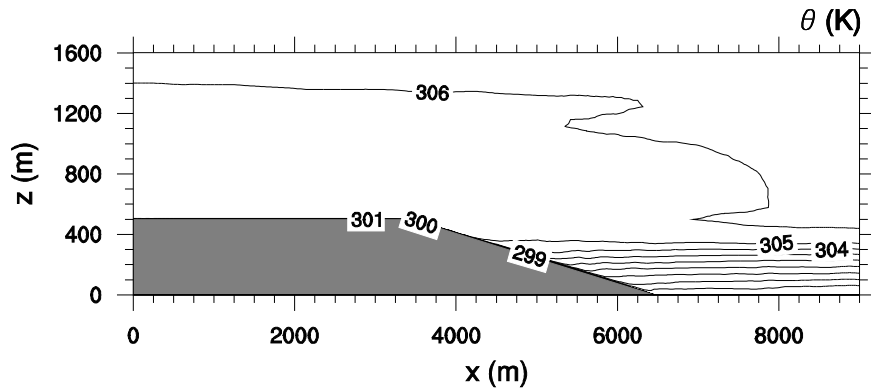
Fig. 4.15. Vertical cross section of the averaged isotherms at t = 17 h for Case 2.
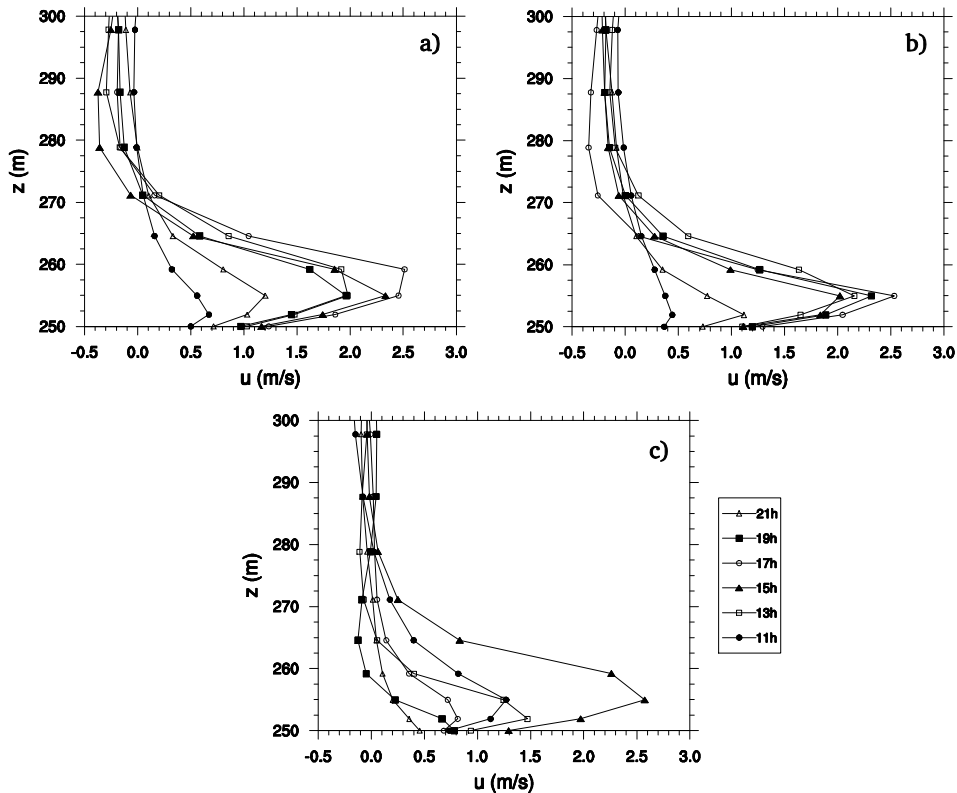
Fig. 4.16. Nighttime vertical profiles of the averaged horizontal wind speed at point B: (a) Case 1, (b) Case 2, (c) Case 3.

The downslope wind is a gravity current, so the length and the angle of the slope are the most important control parameters. The vertical profiles of the wind speed show that, during the onset and the early stage of the katabatic current, the longer

slope of Case 1 (Fig. 4.16a) is characterized by intensity and depth similar to those of the shorter but steeper slopes (Fig. 4.16b, c). Next, the interaction with the growing stable boundary layer inside the basin will make the late evolution of the flow essentially governed by the volume of the valley. In fact, in the smaller basin the growth of the stable boundary layer is faster, causing an earlier damping of the katabatic wind.

In the valley system a stable stratification develops. Over the slope (Fig. 4.17), negative values of surface kinematic heat flux (Fig. 4.6) are associated to the katabatic wind. Over the valley (Fig. 4.18) Q_s is almost zero and the cooling is driven by the advection of cold air by the downslope currents. Three different zones can be distinguished in the vertical direction:

- a shallow surface layer with a strong lapse rate can be observed. Over the slope this layer corresponds to the vertical extension of the katabatic current (Fig. 4.17). The lapse rate in this zone reaches its maximum of 0.3 K/m at 17 h, at the same time where the maximum wind speed is attained;

- a stably stratified layer above with a smaller lapse rate, corresponding to the evolution of the cold pool in the basin; the intensity of the stratification increases during the night;

- a residual layer above 500 m and extending up to the maximum daytime PBL depth.

Up to 17 h the atmosphere above the katabatic layer has a very small lapse rate of 0.007 K/m. After this time the depth and intensity of the katabatic currents begin to decay and the stratification extends to the higher levels of the atmosphere. This phenomenon can be interpreted considering that the katabatic wind produces an increase in the negative turbulent heat fluxes near the ground, which enhances surface cooling. At the same time, warmer air from the ridge is advected in the upper level of the downslope current; this contributes to maintain a shallow stable layer during the first hours of the night.
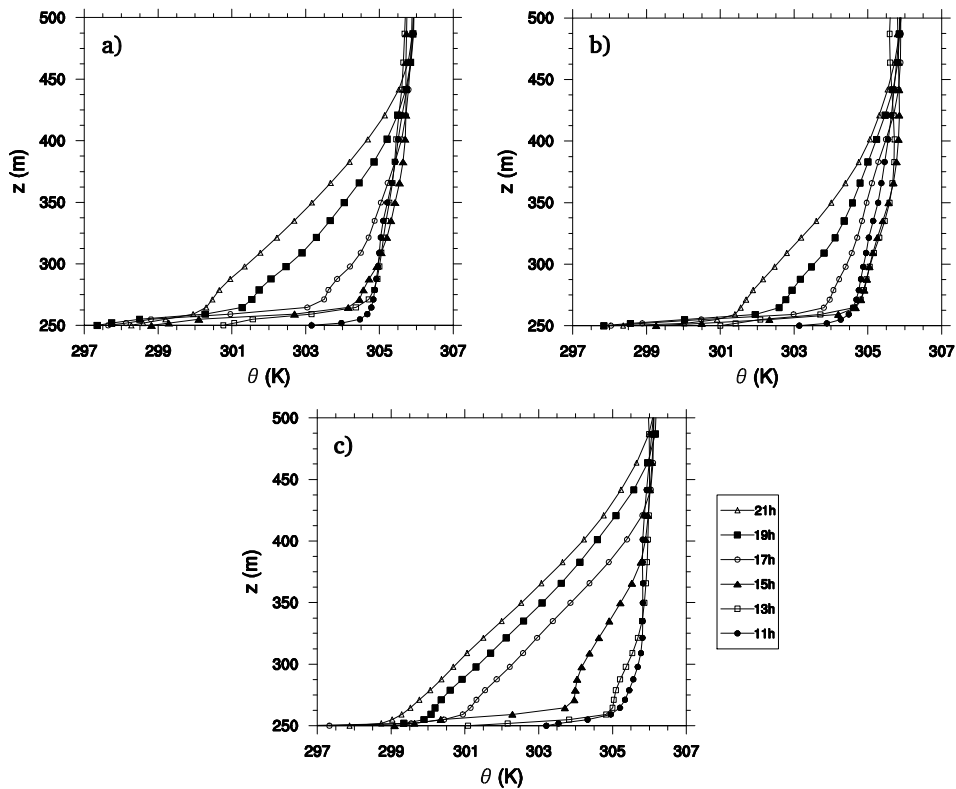
Fig. 4.17. Nighttime vertical profiles of the averaged potential temperature at point B: (a) Case 1, (b) Case 2, (c) Case 3.
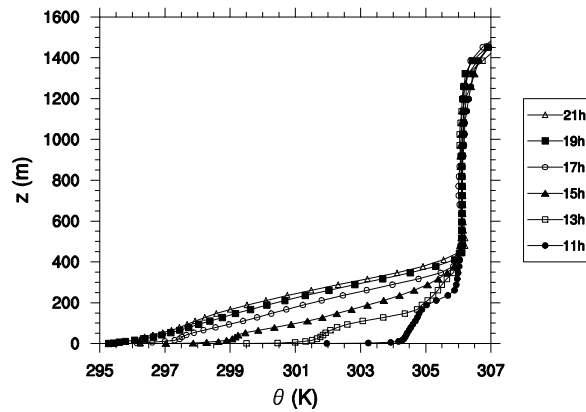
Fig. 4.18. Nighttime vertical profiles of the averaged potential temperature at point D for Case 2.

It is important to recall here that, during the night, over the ridge and the valley the heat exchange is almost zero, while over the slope it reaches absolute values even bigger than the daytime ones (Fig. 4.6), due to the intense momentum fluxes generated by the katabatic wind. Such large negative surface heat flux reflects a limitation of the imposed thermal forcing; in fact, prescribing soil temperature has

the drawback that the feedback with the uppermost soil layer, which would reduce the surface temperature anomaly, is neglected. Nevertheless, our choice for the thermal forcing stresses the importance of considering the coupling between heat and momentum fluxes instead of directly imposing the surface heat flux.

The main parameter which controls the evolution of the nocturnal PBL under this topographical configuration is found to be the volume of the valley; in fact, the smaller valley exhibits a faster cooling (Fig. 4.17). Slope steepness also plays an important role, since the faster current flowing over the steepest slope slightly reduces and delays cooling with the mechanism discussed above.

Intersecting the vertical profiles of potential temperature over the valley at different times with the neutral profile at the end of the diurnal period, it is possible to analyze the evolution of the depth h_p of the cold pool into the valley (Fig. 4.19). The life cycle of the nocturnal inversion starts when the lapse rate becomes positive near the valley floor and ends when the stability regime turns back to be unstable driven by the positive surface heat flux (morning of third day of simulation). In Case 3 the cold pool evolves quickly during the first hours of the night, reaching a depth of $\cong 150$ m at t = 11 h, while for the other cases the stable layer has grown only a few tens of meters. A rapid increase of the cold pool is observed when the base of the former inversion layer is reached; this occurs at $t \cong 10{:}30$ h for Case 3, at $t \cong 11{:}30$ h for Case 1 and at $t \cong 12{:}30$ h for Case 2. At $t \cong 15$ h the depth of the stable core is roughly the same for the three cases; from this point on the growth rate decreases for cases 1 and 2 and a difference in depth of $\cong 50$ m with respect to Case 3 is kept. As already mentioned, one can see the role played by the volume of the valley and the effect of the slope steepness in delaying the formation of the stable boundary layer.
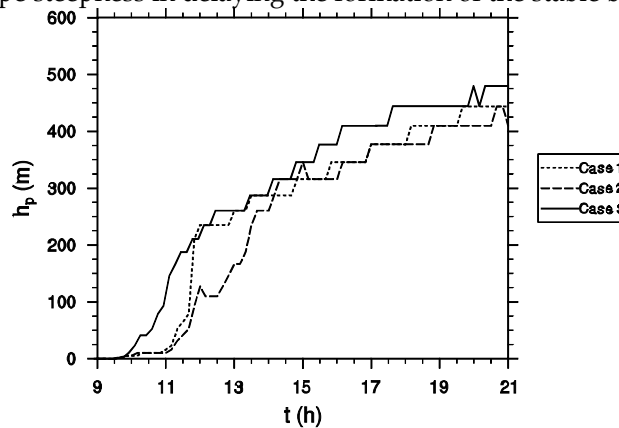
Fig. 4.19. Cold pool height h_P evolution for the different cases computed by the potential temperature profiles taken at point D.

4.3.2   Turbulence

The maximum values of turbulent kinetic energy ($\cong 0.5$ m^2/s^2) over the slope are observed near the surface (Fig. 4.20). At this point the depth of the PBL ($\cong 20$ m) roughly equals the vertical extension of the katabatic current. Despite the increased vertical resolution near the ground, the horizontal grid spacing is still too coarse to

fully capture all the fine turbulent structures in the lowest model layer, hence the modeled components of TKE are the most important contribution during the nocturnal period. In this sense, the results obtained for the nighttime period can be regarded as the output of a RANS model with a second-order closure for the turbulence kinetic energy and a first-order closure for the temperature fluxes. The difference in the model behavior with respect to the diurnal period is due to the fact that the characteristic length scales of turbulence are strongly reduced in presence of stratification. It should be recalled here that the aim of this Chapter is to simulate the entire diurnal cycle over a quite large periodic ridge-valley domain. The choice of the spatial resolution is then a compromise between the need to resolve the main features of the circulation and the computational demand.
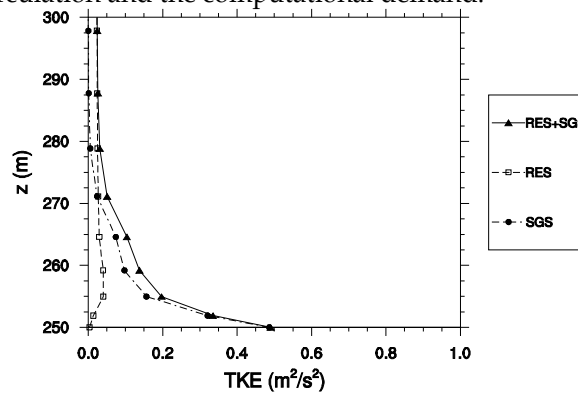
Fig. 4.20. Vertical profiles of TKE at t = 17 h at point B for Case 2. Open squares/ dashed lines represent the resolved contribution, filled circles/ dash-dotted lines shows the subgrid-scale contribution, filled triangles/ full lines represent the total variable.

As the downslope gravity current impacts with the quiescent air of the developing cold pool in the valley, an instability zone forms in association with a vortex and an updraft current (Fig. 4.21). At 17:30 h it is located between x = 4500 m and x = 5000 m, with an extension of 500 m in the horizontal and 100 m in the vertical. If we consider the atmosphere in the framework of a two-layer bulk hydraulic model (Ball 1956), the densimetric Froude number $Fr = \dfrac{U_{max}}{\sqrt{g'h}}$ can be assumed to characterize the instability region. Here $g' = \dfrac{\rho_k - \rho_a}{\rho_a} g$ is the reduced gravity, ρ_k is the density of the katabatic layer and ρ_a is the density of the atmosphere above the current.

50
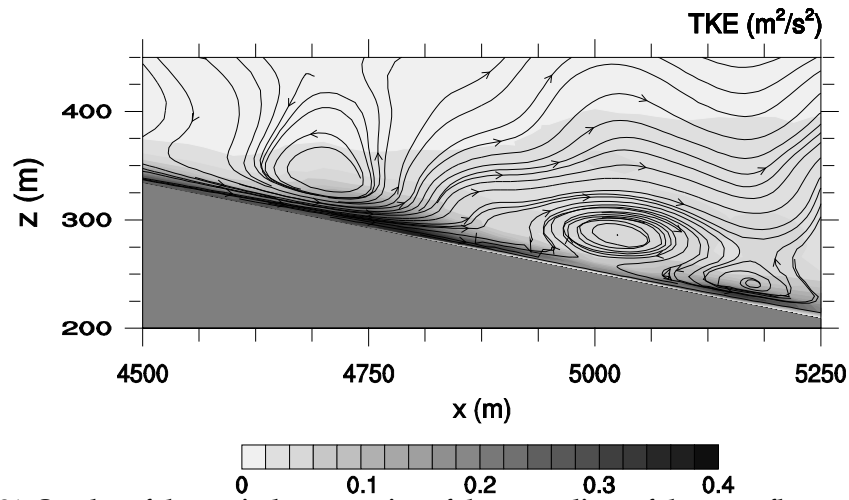
Fig. 4.21. Overlay of the vertical cross section of the streamlines of the mean flow and TKE over the west slope at t = 17:30 h for Case 2: a weak jump beginning at x ≅ 4750 m is revealed by the presence of a vortex and the concentration of TKE.

Although there is a dramatic decrease in Fr immediately after the recirculation zone, its values upwind are less than unity (Fig. 4.22); hence the phenomenon cannot be strictly termed a jump. In any case, it must be said that the uncertainties on the determination of the height of the current make the estimation of Fr prone to some error, since h is the most sensitive parameter for its computation. It must also be observed that the values of h downwind of the jump refer to the small katabatic layer flowing below the instability zone, rather than the vertical extent of the zone itself. Despite the uncertainties associated with the computation of Fr, the structure has most of the characteristics of a katabatic jump: a significant positive vertical velocity can be observed in the middle of the jump (Fig. 4.23) as well as stronger values of turbulent kinetic energy (Fig. 4.21). Further evidence of the presence of the jump can be inferred from the surface kinematic heat flux plot in B (Fig. 4.6) which shows a strong discontinuity in correspondence to t = 17:30 h.

In agreement with Yu and Cai (2006), waves are observed downstream of the jump, as shown in the contour plot of the vertical velocity (Fig. 4.24); the wavelength is about 250 m. These authors attributed the generation of this kind of oscillations to the deformation induced in the wind field by the presence of an updraft region. It is worth noting that Yu and Cai (2006) considered intense (~ 10 m /s) katabatic winds over strongly cooled and long (~ 70 km) slopes in Antarctica. The present study confirms the development of such disturbances on shorter slopes in a valley; with this geometry, the growth of the cold pool assumes an important role in triggering mechanism for the formation of the jump.
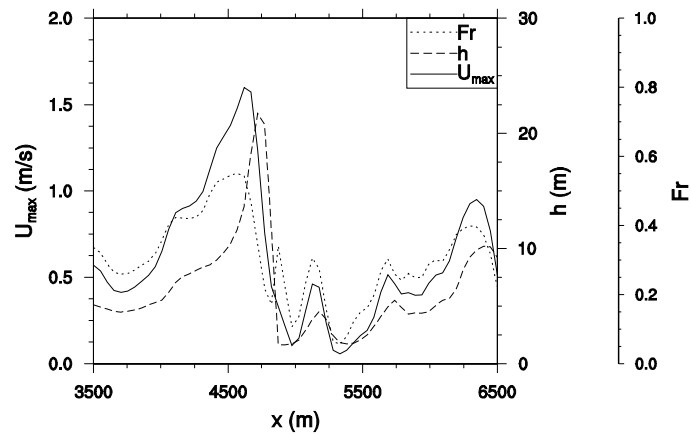
Fig. 4.22. Discontinuity in the x-evolution of the maximum wind speed U_{max}, flow depth h and Froude number Fr at t = 17:30 h over the slope in correspondence of the jump. All the variables are averaged along the y direction.
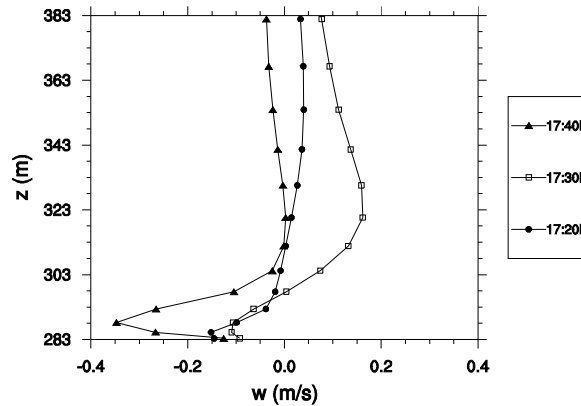
Fig. 4.23. The mean vertical velocity profiles at x = 4750 m for Case 2 at different times show an updraft at t = 17:30 h, when the jump forms.
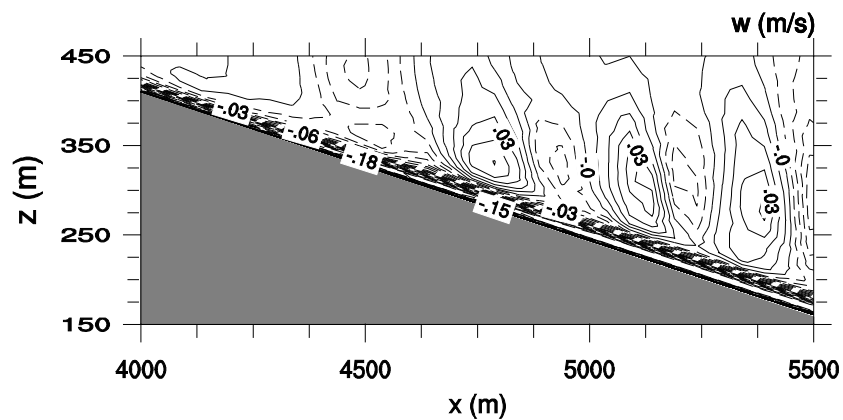
Fig. 4.24. Waves downwind of the jump, as evidenced by the alternate positive-negative pattern shown by the mean vertical velocity contours at t = 17:30 h for Case 2.

4.4   Considerations on the complete cycle

The time evolution over a complete diurnal cycle of the maximum wind speed U_{max}, along with the height of the flow over the slope and the imposed surface temperature θ_s in the middle of the left slope (Fig. 4.25) gives a sketch of the response of the atmosphere to the variable thermal forcing in the presence of complex geometry. This plot also summarizes some of the main characteristics of the upslope and downslope winds, like the differences in intensity and vertical extension. Comparison of the three curves demonstrates that the maximum intensity of the anabatic current occurs about at the same time as the maximum surface forcing. During the day the maximum height of the flow takes place about 2 h later (t = 8 h) with respect to the imposed temperature maximum, due to the horizontal breeze. In the night the maximum depth of the katabatic wind is promptly reached 1 h after the inversion of the surface forcing, then it remains almost constant until the cold pool reaches the middle of the slope at t = 19 h; from this time on the current begins to decay both in intensity and in depth. One can also observe an important drop (~ 2 m/s) in the wind speed and flow depth (~ 15 m) at 17:30 h, when the weak jump is taking place upstream. It is worth noting that the weak jump is an isolated and almost instantaneous phenomenon in our case.
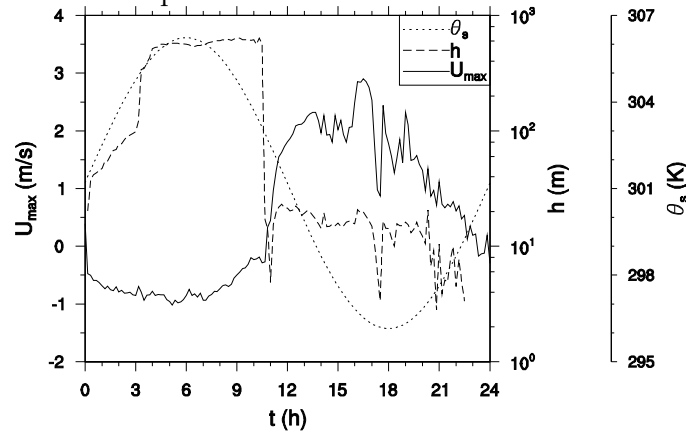
Fig. 4.25. Time evolution of the y-averaged maximum wind speed U_{max}**, y-averaged flow depth** h **(in logarithmic scale) and surface potential temperature** θ_s **at point B for Case 2.**

4.5   Comparisons

In absence of an accurate dataset of measurements taken in conditions similar to those described in this work, we will compare the results with the prediction of two well-known theoretical models. The differences between the hypotheses of the theoretical models and our geometry and boundary conditions pose some limitations that are discussed below.

The HU bulk theoretical model was developed for the anabatic flow over a finite slope and a ridge. Since this model assumes a steady state flow, in order to make a comparison with measurements or results from prognostic numerical models, quantities must be considered averaged over the diurnal period (positive surface

heat flux). The calibration parameter λ for the HU model, defined in (3.5), is obtained from the current simulations averaging over the depth of the anabatic layer the values of the wind speed taken in point B. The values of λ are compared with the field measurements of Princevac et al. (2001), the laboratory investigation of Chan (2001) and Cenedese et al. (2004) and the simulations of Catalano et al. (2007). It can be seen (Table 4.3) that the development of the horizontal breeze, which is a peculiarity of our investigation, causes lower values of λ, due to the resulting higher values of the flow depth.

	λ
this study	1.76
Catalano et al. 2007	3.42
Cenedese et al. 2004	3.73
Chan 2001	3.3
Princevac et al. 2001	4.15

Table 4.3. Comparisons with literature determinations of the λ parameter for the HU model.

The MS model predicts the depth of the katabatic wind as a function of the distance from the beginning of the slope; they considered a semi-infinite slope. Our results for cases 1 and 2 (Fig. 4.26 a and b) show a fairly good agreement for the upper part of the slope, then they deviate from the theoretical predictions as the wind impacts with the quiescent air of the cold pool. For Case 3 (Fig. 4.26c), at this time (17:30 h) the current has been significantly weakened by the cold pool development and hence the comparison is quite poor. An interesting feature is that the depth of the katabatic wind inside of the cold pool layer is reduced proportionally to the length of the slope, with the longer slope (Case 1) showing a deeper residual flow. Another difference with respect to the theoretical predictions can be seen near the upper end of the slope, due to the fact that the MS model was developed for a slope without a ridge; here it appears that the current tends to propagate downward on the ridge for a certain extent with a depth of $\cong 5$ m.

The plot for Case 2 gives further evidence of the weak jump, which appears as a discontinuity in the flow depth with a slight increase upwind and a strong decrease downwind.
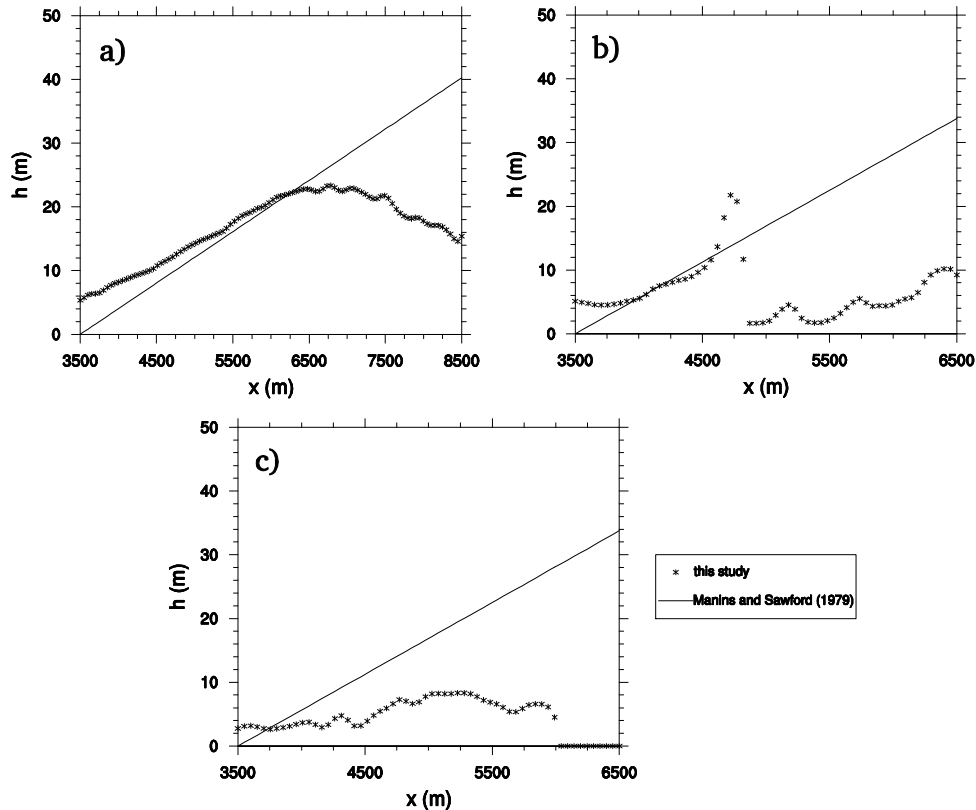
Fig. 4.26. Comparisons of the y-averaged depth h of the katabatic wind determined by this study with the theoretical predictions of the MS model at t = 17:30 h: (a) Case 1, (b) Case 2, (c) Case 3.

4.6   Summary

The three dimensional non-hydrostatic meteorological model WRF was modified to perform Large Eddy Simulations of the thermally driven circulation over a valley under calm geostrophic wind conditions.

In order to correctly reproduce the fine structures of the anabatic and katabatic winds a vertically stretched grid was introduced with a finer mesh close to the ground. With highly anisotropic grids, problems arise with the classical definition of the filter width, so the length scale of the subgrid scale model was modified according to the theoretical considerations of Scotti et al. (1993).

Most of the past LES studies in the literature introduced the forcing at the bottom boundary of the domain by directly imposing the surface heat flux as the term h_j in the right hand side of (2.50). The most important drawback of this formulation is that it does not take into account the coupling between heat and momentum fluxes in the surface layer and thus cannot reproduce the differential heating of zones with different flow characteristics. In the present study the LES model is coupled with a surface layer scheme; the surface heat flux as well as the

friction velocity were computed according to the Monin-Obukhov similarity theory. Differences with respect to a previous study without coupling of Catalano et al. (2007) were emphasized. It should be recalled here that prescribing the surface temperature anomaly (as in this study) still has the drawback that the feedback with the uppermost soil layer cannot be simulated.

The evolution of the diurnal boundary layer was investigated, pointing out the great importance of the subsidence over the valley and its related warming. A horizontal breeze develops as a consequence of the layered thermal structure of the basin. This flow can be explained considering the mutual influence of two principal factors: 1) the interaction between the subsidence current over the valley and the strongly stratified layer below; 2) the smaller mass flux associated to the lower slope region which is characterized by a stronger stratification. The large mass-flux required by the upper circulation is then partially recovered horizontally. The higher values of the surface kinematic heat flux over the ridge compared to those at the bottom of the valley also cover an important role in this phenomenon.

The waves at the interface between the anabatic wind and the horizontal breeze were correctly reproduced and shown by the streamlines. The parameter λ from the HU theoretical model was computed and compared with previous investigations; the most relevant effect of the valley geometry is a lowering of this parameter due to the higher values of the flow depth caused by the interaction of the anabatic wind with the horizontal breeze.

The nocturnal boundary PBL was investigated along with the evolution of the cold pool into the valley. It was found that the volume of the valley is the most important parameter for the evolution of the katabatic winds in a valley, since it controls the rate of the growth of the stable boundary layer into the basin. The resolution of this study, even if not large enough to fully resolve the small surface structures of the SBL, allowed capturing the flow separation which occurs as the fast katabatic wind impacts with the quiescent air of the cold pool. Comparisons with the MS hydraulic model show an agreement outside of the cold pool layer; in the lower part of the basin the depth of the katabatic current is reduced proportionally to the volume of the basin and the length of the slope. The formation of a hydraulic jump induces an increase of the flow depth upwind and a sensible decrease downwind of the discontinuity with respect to the theoretical predictions.

During the nighttime period the SGS contribution to total TKE is significantly larger than the resolved one, thus the results should be interpreted like those of a RANS model with a second-order closure for the turbulence kinetic energy and a first-order closure for the temperature fluxes. The compromise on the spatial resolution is motivated by the aim of this work to reproduce both diurnal heating and nocturnal cooling over a quite large periodic ridge-valley domain.

5   Large Eddy Simulation of the circulation in a valley: influence of geostrophic wind

A three dimensional meteorological model is used to perform large eddy simulations of the upslope flow circulation over a periodic ridge-valley terrain. The subgrid-scale quantities are modeled by a prognostic TKE scheme. The grid has a constant horizontal resolution of 50 m and is stretched along the vertical direction. To account for the grid anisotropy a modified subgrid length scale is used. To allow for the response of the surface fluxes to the valley-flow circulation, the soil surface temperature is imposed and the surface heat and momentum fluxes are computed based on Monin-Obukhov similarity theory. The model is designed with a symmetrical geometry using periodic boundary conditions in both x and y. Two cases are simulated to study the influence of along-valley geostrophic wind forcing with different intensities. The presence of the orography introduces numerous complexities both in the mean properties of the flow and in the turbulent features, even for the idealized symmetric geometry. Classical definitions for the height of the PBL are revisited and redefined to capture the complex structure of the boundary layer. Analysis of first- and second-moment statistics, along with TKE budgets, highlights the different structure of the PBL at different regions of the domain.

This Chapter aims at investigating both the mean quantities and turbulent variances and fluxes that characterize the daytime circulation over a valley with an LES based on the WRF model. In order to reduce the degree of freedom of the system and to isolate the interacting phenomena we will limit the study to a simple periodic ridge-valley terrain. The model characteristics along with the simulation setup are briefly discussed in Section 5.1, Section 5.2 presents the flow feature and turbulence statistics that develop during the daytime convective PBL and the transition to the nighttime stable atmosphere. Section 5.3 examines the effect of geostrophic wind along the valley. Section 5.4 summaries the work with some discussions and remarks.

5.1   Model and experiment setup

The three dimensional meteorological model WRF (The Weather Research and Forecasting Model) is used as a framework for the LES simulations of the present work. WRF is a fully compressible, non-hydrostatic model with a terrain-following hydrostatic-pressure vertical coordinate. The model has been shown to be a good tool for LESs (Moeng et al. 2007), but has never been still needs to be thoroughly tested to perform LES in complex geometries. In a recent work, Lundquist et al. (2010) performed high resolution simulations of the flow over an urban skyline with WRF using the immersed boundary method but without focusing on the turbulent

fluxes. This work hence provides a step toward developing a multi-scale model for real-world PBLs which often consist of both mesoscale circulations and microscale turbulence.

Since the scales of the investigated phenomena are quite small we neglect the Coriolis terms in the LES equations, but implicitly include the Coriolis effect in the geostrophic forcing. We also limit our study to a dry atmosphere. The modified WRF TKE diffusion scheme, described in Sections 2.4.1.1 and 4.1, is used to model the effects of SGS turbulence.

The domain geometry is shown in Fig. 4.2. The parameters of the domain setup are reported in Table 5.1. The domain is very similar to that of Case 2 in Chapter 4; here the width d has been increased to improve the robustness of second-moment statistics.

a (m)	3500
b (m)	3000
c (m)	5000
d (m)	5000
h (m)	500
H (m)	2400
β	$\cong 9°30'$
V_{valley} (km^3)	12

Table 5.1. Domain configuration: geometry is given in Fig. 4.2.

The horizontal grid resolution is uniform, $\Delta x = \Delta y = 50$ m; the vertical grid is defined with a parabolic stretching in order to have $\Delta z \cong 2$ m near the ground and $\Delta z \cong 90$ m at the top of the domain. The time step for the RK loop and the acoustic time-split scheme, as well as the parameters controlling the algorithm for acoustic wave modes damping are reported in Section 4.1.

Periodic lateral boundary conditions are imposed in x and y, so the valley flow and turbulence statistics are symmetric about $x = L_x/2$. The top boundary of the domain is assumed to be at constant pressure with zero vertical velocity; as discussed in Section 4.1, an upper damping layer is not necessary for the present simulations. The lower boundary condition is described by the sinusoidal thermal forcing given by (4.2). The initial soil temperature is a function of the height of the ground relative to the bottom of the valley (z_s). The evolution of the surface temperature is shown by its Hovmöller plot (Fig. 5.1). The surface heat flux and the friction velocity are computed according to Monin-Obukhov similarity theory.

58
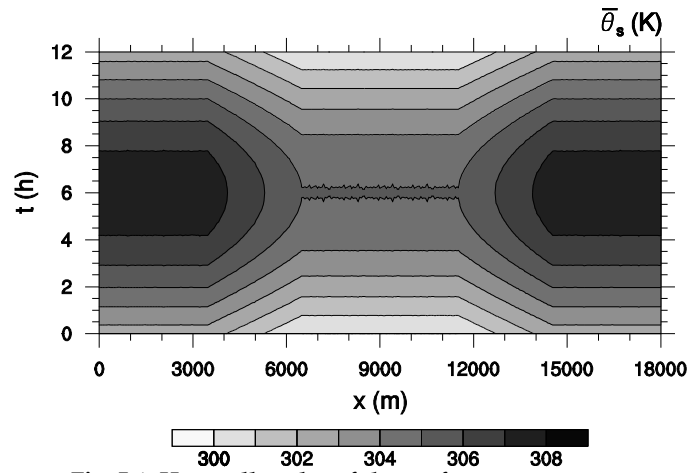
Fig. 5.1. Hovmöller plot of the surface temperature.

Two cases were investigated to study the influence of along-valley geostrophic wind on the thermal circulation and turbulence properties. Case 1 with V_g = 2 m/s represents a situation which is likely to occur in a real PBL over weak synoptic systems, while Case 2 is driven by a stronger geostrophic condition of V_g = 10 m/s. In both cases the symmetry in x is preserved by the orientation of V_g. The surface roughness z_0 is set to 0.3 m (e.g. brush).

The total grid points are 360 in x, 100 in y, and 58 in z. The model was integrated for 12 h, starting from the sunrise, to simulate the daytime PBL cycle. As discussed in Section 4.3, our grid resolution is not fine enough to fully resolve the turbulent eddies in the nighttime PBL; in fact, for very stable regimes the SGS component of the turbulent fluxes is prevailing and the model results can be interpreted like those of a RANS model with a second-order closure for the turbulence kinetic energy and a first order closure for the temperature fluxes.

5.2   Results

Since the valley flow and the PBL turbulence are driven mainly by surface heating, we first present the time evolution of the y-averaged surface kinematic heat flux in Fig. 5.2, for Case 1. In the valley, the surface kinematic heat flux reaches its maximum around hour 4 even though its ground temperature is warmest around 6 h. This shows an evidence of strong coupling of the surface to the valley flow, which results in the largest difference between the surface and the near-surface air temperature at hour 4. Over the ridge, the maximum heat flux occurs around hour 5. The sharp peak near the top of the slope is about twice of the maximum value over the valley. The time cycle over the slope region shows an intermediate situation between the ridge and the valley, with stronger flux toward the ridge. The surface flux becomes negative after $\cong$ 8 h over the valley and after $\cong$ 9.5 h over the ridge. The largest negative heat flux occurs at $\cong$ 12 h near the foot of the slope. As outlined in Chapter 4, this complicated spatial and temporal evolution of the surface kinematic heat flux is typical of steep alpine valleys, as documented by the field measurements of Rotach et al. (2004) and the numerical simulations of Chow et al. (2006), and can

be reproduced only through the computation of the surface heat fluxes from a coupled surface layer scheme; such complicated interaction between valley-flow and surface fluxes was neglected in previous studies that imposed a constant surface heat flux (Catalano et al. 2007).
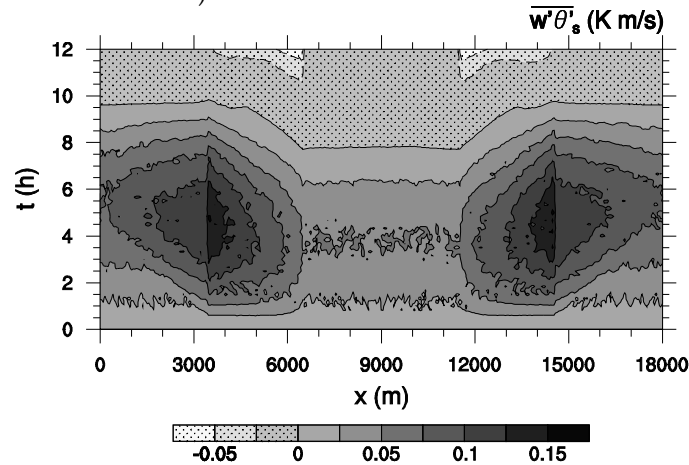
Fig. 5.2. Hovmöller plot of the y-averaged surface kinematic heat flux for Case 1 (V $_g$ = 2 m/s).

5.2.1 Instantaneous flow fields

Due to the symmetric geometry of the numerical domain, the simulated flow field remains symmetrical about the vertical plane at x = L_x/2. Henceforth, in most contour plots we will show just the west half of the domain. One of the most important advantages of the LES approach is the ability to resolve the turbulent structures of the flow. The instantaneous flow field at t = 7 h of simulation, when the daytime circulation is well developed, displays both terrain-induced mesoscale circulations as well as the random turbulent motions. The potential temperature field (Fig. 5.3a) shows a shallow mixed layer with a well-defined inversion at z $\cong$ 400 m over the valley and a deep mixed layer with an inversion at z $\cong$ 1300 m over the ridge, while the wind field (Fig. 5.3b) reveals a large circulation with an upslope wind near the surface and a return flow below z $\cong$ 1300 m. The streamline also suggests a secondary circulation (i.e., clockwise between z $\cong$ 400 m and 1300 m) in the upper part of the valley and slope region, which will be described later.

Fig. 5.4 provides a horizontal view of vertical velocity fluctuations at $\cong$ 50 m above the ground. Irregular cellular pattern is observed over the ridge and slope areas, which is typical of a CBL. The turbulent fluctuations are much weaker in the valley. As shown, the surface kinematic heat flux at this simulation hour is positive at all locations but it is at least three times smaller over the valley. The horizontal density gradients over the slopes produce an anabatic wind near the surface blowing from the valley toward the ridges; this is also reflected in the observed surface kinematic heat flux differences in the different regions of the domain. Over the valley the eddy structure is oriented along the y direction; this elongated feature

is related to the vertical shear induced by the geostrophic wind forcing and its interaction with the surface buoyancy.
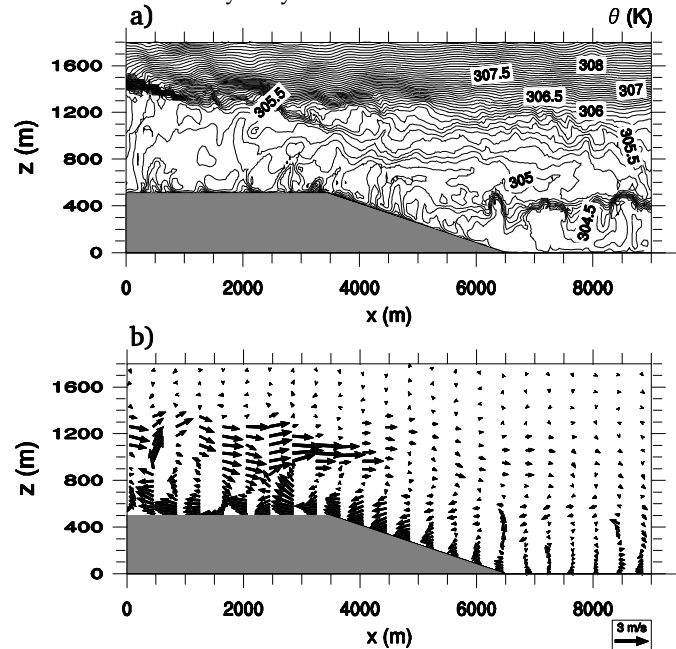
Fig. 5.3. Instantaneous vertical cross sections: isotherms (a) and vectors (b) at t = 7 h for Case 1 (V_g = 2 m/s), taken at y = L_y/2.
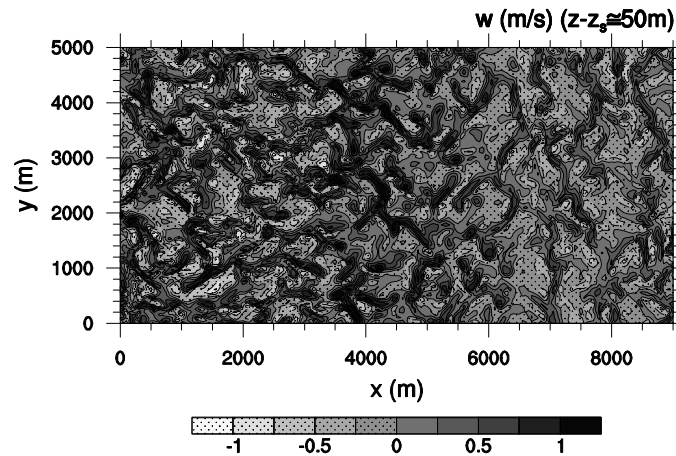
Fig. 5.4. Instantaneous horizontal cross section of the vertical velocity at t = 7 h for Case 1 (V_g = 2 m/s), at a fixed relative height from the ground.

5.2.2   Averaging procedures for computing statistics

Most of previous LES studies investigated idealized PBLs over horizontal homogeneous surfaces (both in x and y directions), so the averaging procedure in defining turbulence statistics was straightforwardly obtained by horizontal averaging; this approach guarantees a sufficient number of sample points for the

robustness of the statistics even with domains of modest sizes. In the present case the only statistically homogeneous direction is in y. Therefore, the perturbations φ' are defined:

$$\varphi'(x,y,z,t)=\varphi(x,y,z,t)-\overline{\varphi}(x,z,t) \tag{5.1}$$

where φ is the instantaneous value of the considered variable, $\overline{\varphi}=\dfrac{1}{L_y}\displaystyle\sum_{j=1}^{N_y}\varphi_j$ is its

average value along the y direction, and L_y is the length of the domain in y. The averaging length L_y has to be more than ten times the turbulence integral scale in order to obtain reliable statistics (Wyngaard 1983). In this study, we set L_y = 5 km, which is a compromise between the needs for a long averaging length and the computational demand. To improve the data sample for reliable statistics, all moment statistics are subsequently averaged in time over a period of 40 minutes.

5.2.3   Distributions of first-moment statistics

The averaged potential temperature at hour 7 in Fig. 5.5 shows a deep well-mixed PBL in the ridge region where the PBL is capped by a well-defined inversion layer above z ≅ 1300 m. In the valley, the PBL is much shallower with a capping inversion between z = 300 m and 450 m. Below the free atmosphere (z < 1200 m) two interacting internal boundary layers can be identified over the valley (6500 m < x < 11500 m) at this time, separated the thermal inversion: the lower one is quite uniform and extends up to z ≅ 400 m; the upper one, located at 500 m < z < 1200 m, is horizontally inhomogeneous. The inversion is maintained by (1) the warm-air advection from the return flow and (2) by subsidence warming due to the sinking motion of the induced circulation. A relevant effect of this twofold warming mechanism is the depression of the development of the CBL in the basin, as confirmed by the measurements of Kondo et al. (1989). The mean temperature field shows a horizontal gradient of the near-surface temperature along x, which leads to the development of an anabatic flow over the two slopes as revealed by the stream function of the averaged wind fields (Fig. 5.6).
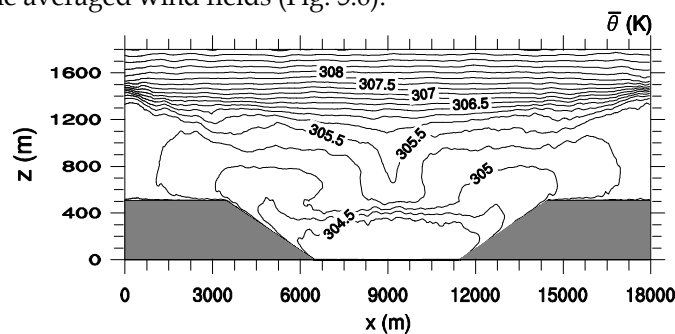
Fig. 5.5. Averaged vertical cross section of isotherms at t = 7 h for Case 1 (V_g = 2 m/s).
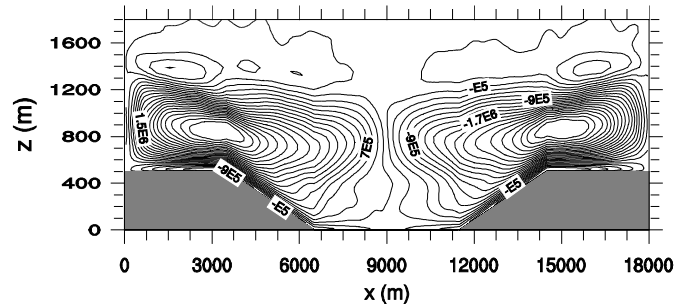
Fig. 5.6. Stream function of the averaged wind field at t = 7 h for Case 1 (V $_g$ = 2 m/s).

Fig. 5.7 shows the three components of the mean wind at hour 7. The maximum intensity of the upslope wind is attained at t = 5 h (not shown). After that time, the depth of the upslope current continues to rise and eventually merges with a horizontal breeze (westward) located between z = 400 m and 800 m and extending from valley into the slope region (Fig. 5.7a). This horizontal breeze occurs at the terrain-height level of the ridge and is driven by the horizontal pressure gradient between the valley and the ridge. The horizontal breeze, along with the return flow, induces a secondary circulation in the upper part (400 m < z < 1300 m) of the domain. This secondary circulation could affect the air quality of cities in such an environment enhancing the dispersion of pollutants into upper air (above the mixed layer) over the valley. Similarly to the cases described in Chapter 4, this upper-level circulation is maintained by the subsidence over the center of the valley and the presence of a strong inversion at $z \cong 400$ m over the valley. The inversion forces the downward flow to diverge and move horizontally toward the ridges. Note that between $z \cong 500$ m and $z \cong 800$ m the potential temperature of the air above the slope is lower than that over the valley (Fig. 5.5), and hence the horizontal breeze blows against the horizontal gradient of temperature. A more detailed description of the mechanisms responsible of the formation of this current has been given in Section 4.2.1.

The along-valley component of the wind (Fig. 5.7b), forced by the prescribed geostrophic wind, shows a tunneling effect in the center of the valley, where a shallow layer with an intensity of about 1.8 m/s is present between 400 m and 500 m. This layer coincides with the westward horizontal breeze layer seen in Fig. 5.7a, together suggesting a north-westward current confined at the top of the PBL in the valley, and this current extends to the slope region and sits in between the anabatic flow and the return current.

The vertical velocity (Fig. 5.7c) shows strong updrafts around x = 0 m where the two upslope flows converge (due to the periodic boundary condition in x). The characteristic depth of the mean updrafts decreases toward the valley, as the surface heat flux decreases. A broad mean subsidence extending over the whole valley can be observed between $z \cong 500$ m and $z \cong 1100$ m with an intensity of 0.1 - 0.2 m/s.
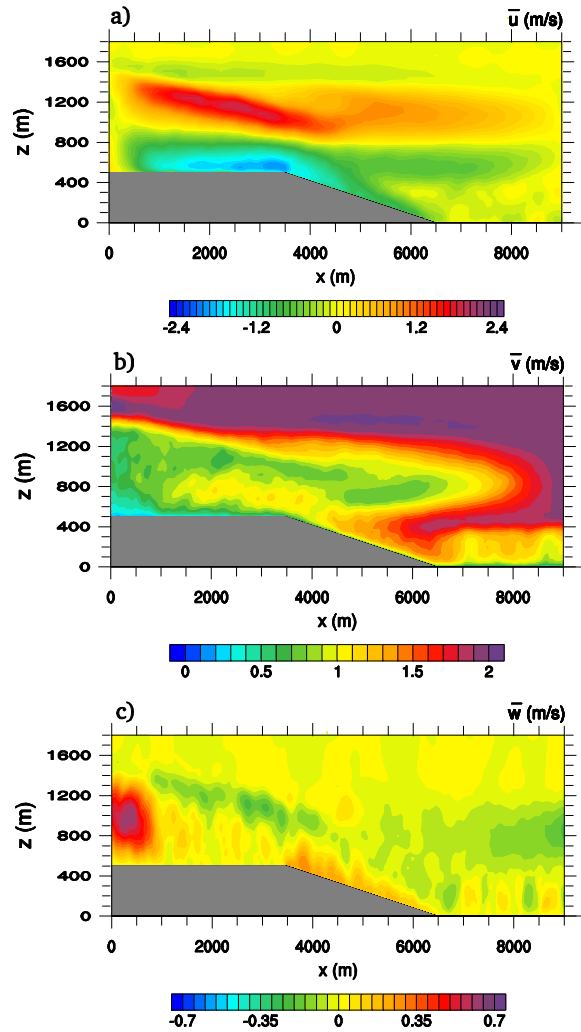
Fig. 5.7. Averaged vertical cross sections: $\overline{u}$ **(a),** $\overline{v}$ **(b),** $\overline{w}$ **(c) at t = 7 h for Case 1 (V_g = 2 m/s).**

5.2.4   The PBL depth

Due to the variable orography, the height of the PBL z_i must be defined locally and relative to its ground level z_s. Also, different definitions must be given depending on the stability regime, which varies with time and x location, as seen from the sign of the surface kinematic heat flux (Fig. 5.2). The complex and spatially varying PBL structure makes the classical definitions for the convective boundary layer (based on the minimum of the vertical kinematic heat flux or the maximum potential temperature gradient, Sullivan et al. 1998) inapplicable.

For the unstable regime ($\overline{w'\theta'}_s > 0$) we propose to define z_i as the height where the magnitude of the vertical gradient of potential temperature goes above a critical

value Γ_c = 0.001 K/m (i.e., at the base of a capping inversion) with the additional constraint that the heat flux is less than 15% of its maximum value. This definition is justified by the shape of the vertical profiles of the mean potential temperature at different x locations at t = 7 h (Fig. 5.8), where the height relative to the ground $z_r = z - z_s$ has been normalized by z_i. While over the ridge there is a clear signal for a single inversion layer, over the slope and the valley two inversions exist; over the valley the lower inversion corresponds clearly to a sharp capping inversion, while this is not the case over the slope region. Because we exclude the entire capping inversion zone to be part of the PBL, our method may underestimate z_i compared with the common definitions of the CBL depth.
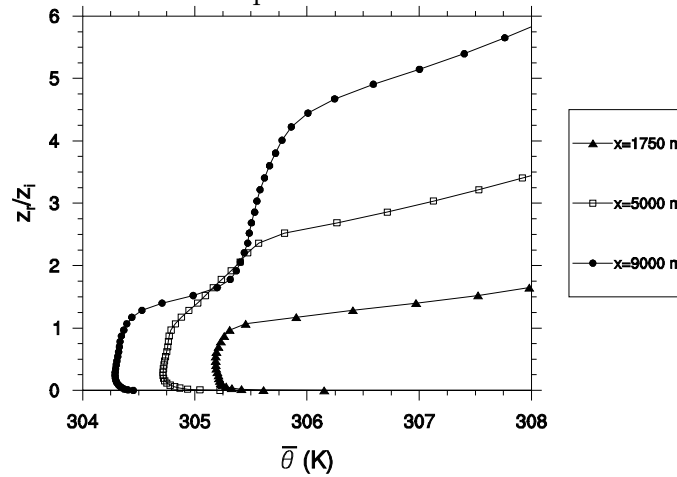
Fig. 5.8. Profiles of the averaged potential temperature $\overline{\theta}$ at different x locations at t = 7 h for Case 1 (V_g = 2 m/s) as a function of the non-dimensional vertical coordinate $z_r/z_i = (z - z_s)/z_i$, where z_i is the PBL depth and z_s is the local terrain elevation. Filled circles refer to the valley centre, open squares refer to the middle of the left slope and filled triangles refer to the middle of the left ridge.

For the near-neutral to moderately stable regimes ($\overline{w'\theta'}_s \leq 0$, e. g., during the evening transition) we distinguish between two situations: (1) when the PBL structure is dominated by the surface wind shear (due to geostrophic forcing); and (2) when the effect of temperature stratification (i.e., surface inversion) prevails. The friction velocity u_* is used to distinguish the two conditions with an empirical threshold value of 0.2 m/s. For the former case, z_i is defined as the height where the along-y component of wind shear $\sqrt{\left(\dfrac{\partial \overline{v}}{\partial z}\right)^2}$ goes below a critical value S_c = 0.005 s^{-1}, which is the height where the $v \cong V_g$. For $u_* <$ 0.2 m/s, the inversion strength approach proposed by Hyun et al. (2005) is applied and z_i is defined at the level where the surface inversion strength $\delta = \theta - \overline{\theta}_s$ is smaller than 20% of its maximum value.

We have also tested a method based on the values of TKE (not shown) that could be applied to both unstable and stable regimes, but the presence of upper-level turbulence (to be discussed in the next subsection) induced by the interaction of the valley flows with the geostrophic wind makes this method impractical.

The time evolution of the PBL depth for Case 1 is reported in Fig. 5.9. We compute z_i at each (x, y) location and average them along y and also over a time period of 40 minutes. The plot shows a substantial increase of z_i up to the time where the surface heat flux becomes negative (Fig. 5.2), and then the PBL drops abruptly to below 50 m. As we will see in section 4, this can be attributed to the weak geostrophic forcing which does not produce enough shear to generate turbulence against the negative surface heat flux. Maximum PBL depths of about 850 m are observed at both ends of the ridges in correspondence to the strong updrafts. The average PBL depth over the slope (about 400 m in its middle) is about 100 m higher than that over the valley, although this value does not consider the upper mixed layer that forms over the valley (see Fig. 5.8).
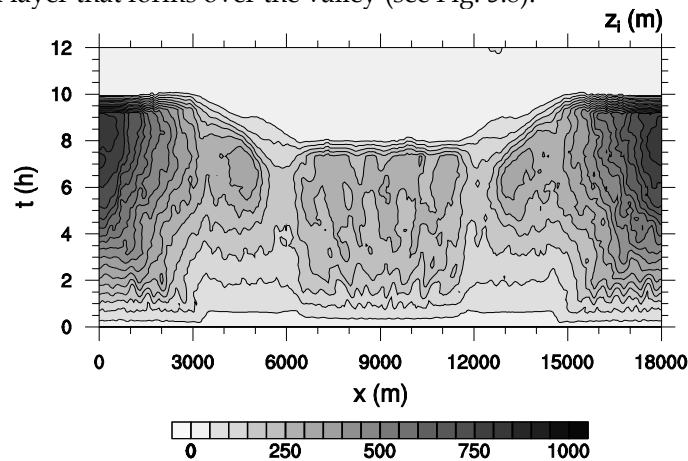
Fig. 5.9. Hovmöller plot of the PBL depth z_i for Case 1 (V_g = 2 m/s).

5.2.5   Distributions of second-moment statistics

Fig. 5.10a shows a vertical cross section of the total TKE, along with the wind vectors at hour 7; the black line shows the estimate PBL depth. At this time, the inclination of the growth line of the z_i over the ridge is close to the angle of the slope. The horizontal breeze at $z \cong 400$ m over the slope does not cause a noticeable increase in the turbulence kinetic energy. Over the valley region, z_i is about 300 m while the TKE remains significant at about 400 m. Hence the method we proposed to compute z_i underestimates the turbulence layer by about 25% over the valley in the presence of a strong capping inversion. To understand the source of TKE, we examine the individual components of the velocity variances. The SGS contributions to these variances are assumed to be 2/3 of the predicted SGS TKE. Over the ridge, the most important contribution to the TKE comes from the u-variance (Fig. 5.10b), except near the west boundary where w-variance dominates (Fig. 5.10d). The large contribution from the u-variance in the CBL over the ridge is unexpected; the TKE in the bulk of a typical CBL is usually dominated by the w-variance instead (e.g.,

Moeng and Sullivan 1994). The dominance of the u-variance in TKE implies a significant shear production due to valley-flow circulation, which will be confirmed later. The turbulence over the slope is mostly determined by the w-variance. The v-variance contribution (Fig. 5.10c) is relatively small, except in the inversion layer near the west-end boundary where the buoyancy flux is negative (Fig. 5.11a). Fig. 5.10a and b also reveal double peaks in the u-variance profiles over the ridge and the upper part of the slope: one in the middle of the PBL and the other near the PBL top. The TKE budget shown later suggests that the upper maximum is due to horizontal advection of the TKE. Overall the TKE over the ridge is about two times higher than that over the slope and three times higher than that over the valley.

The vertical fluxes (resolved plus SGS) are shown in Fig. 5.11. The kinematic heat flux is mostly positive except near the PBL top, which is typical of the CBL. Negative fluxes at the CBL top are the capping inversion regions, which agree well with our estimated z_i shown in the same plot (Fig. 5.11a). The strong negative values of $\overline{u'w'}$ (Fig. 5.11b) and the significant positive gradients of mean u over the ridge (Fig. 5.7a) yield a large shear production for TKE, which explains the large contribution of u-variance to TKE in that region. In the valley, negative $\overline{v'w'}$ (Fig. 5.11c) coincides with positive v-gradient in the lower PBL (Fig. 5.7b) which also contributes to shear production for TKE. The horizontal flux $\overline{u'v'}$ shown in Fig. 5.11d will be used to discuss the TKE budget later.
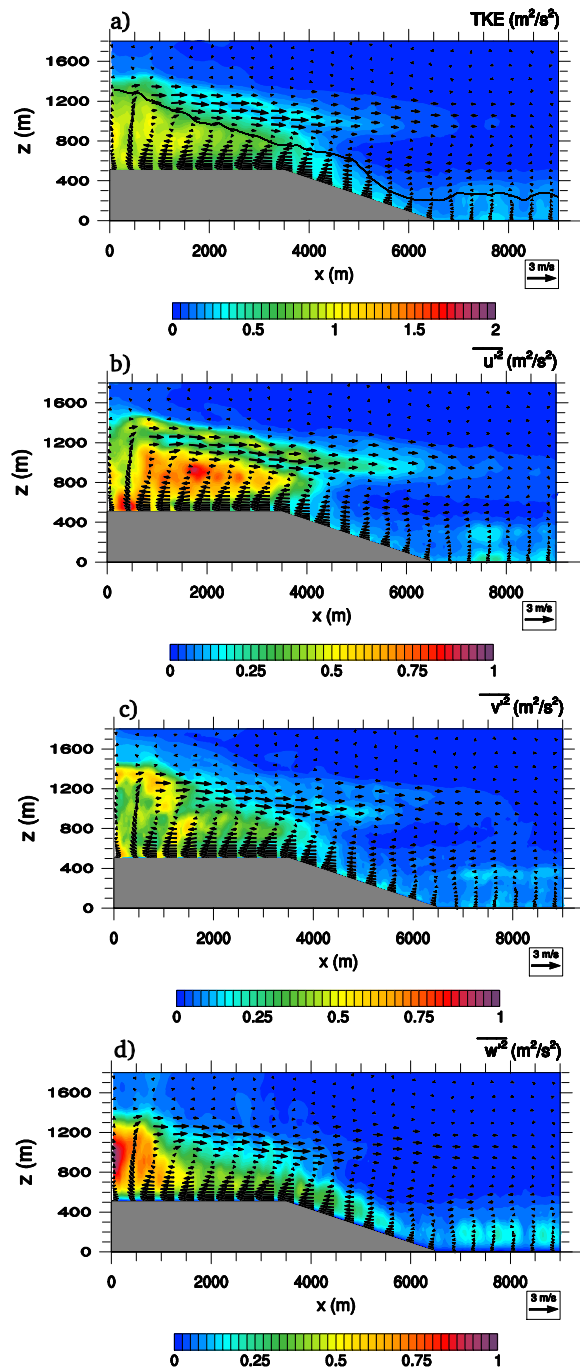
Fig. 5.10. Vertical cross sections of TKE and variances, together with the averaged wind vectors: TKE (a), $\overline{u'^2}$ (b), $\overline{v'^2}$ (c), $\overline{w'^2}$ (d) at t = 7 h for Case 1 (V_g = 2 m/s): the black line in panel (a) delineates the PBL depth.
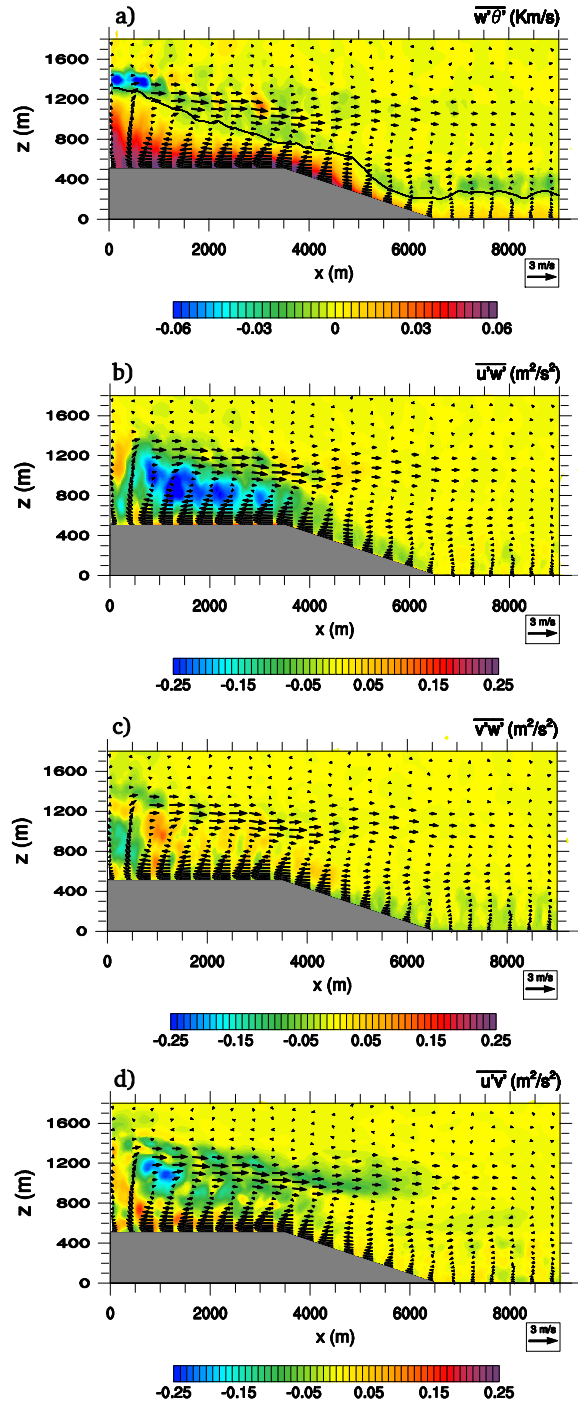
Fig. 5.11. Vertical cross sections of fluxes, together with the averaged wind vectors: $\overline{w'\theta'}$ (a), $\overline{u'w'}$ (b), $\overline{v'w'}$ (c), $\overline{u'v'}$ (d) at t = 7 h for Case 1 (V_g = 2 m/s): the black line in panel (a) delineates the PBL depth.

In our simulations we reproduce the interaction of three forcing mechanisms: (1) buoyancy resulting from the surface heat flux; (2) baroclinic shear induced by the valley-flow circulation; (3) shear generated by the imposed geostrophic forcing. Even if buoyancy dominates in many regions of the domain (particularly in Case 1), shear plays a marked influence on the TKE and particularly during the transition toward the nighttime period.

To normalize the vertical profiles of variances, fluxes, and TKE budgets, we apply the scaling law proposed by Moeng and Sullivan (1994) which takes into account both buoyancy and shear effects, for the period when the surface heat flux is positive. The velocity scale w_m^2 is defined as $w_m^3 = w_*^3 + 5u_*^3$ while the temperature scale is $\theta_m = \dfrac{\overline{w'\theta'}_s}{w_m}$, where $w_* \equiv \left(\dfrac{g}{T_0} \overline{w'\theta'}_s z_i \right)^{1/3}$ is the convective velocity proposed by Deardorff (1972) and $\dfrac{g}{T_0}$ is the buoyancy parameter. This scaling approach assumes a linear combination of convection and surface shear effects and hence neglects all nonlinear feedbacks between shear and buoyancy forces. Nevertheless, it has been shown to be a suitable scaling for the second- and third-order moments of turbulence in sheared CBLs (Moeng and Sullivan 1994). For the moderately stable regime (discussed in the next section), we use u_* as the velocity scale since shear is the only mechanism responsible of turbulence production. We also normalize the height z_r by the estimate z_i shown in Fig. 5.9.

Here we will discuss the profiles taken in the middle of the slope shown in Fig. 5.12 as an example. The upper maximum of the normalized $\overline{u'^2}$ (at about $z_r/z_i = 2$), is about 1.8 times larger than the lower one, so the contribution from horizontal advection accounts for a very important part of the turbulence over the slope. The v-variance also shows an upper maximum from advection at the same level. The maximum of w variance occurs at $z_r/z_i \cong 0.4$, which is typical of a CBL (Nieuwstadt et al. 1993; Moeng and Sullivan 1994). The profile also shows a secondary maximum at $z_r/z_i \cong 2.1$, albeit small, which has been observed in sheared CBLs (Sorbjan 2004; Conzemius and Fedorovich 2006). The momentum flux $\overline{u'w'}$ (Fig. 5.13a) is positive very close to the surface ($z_r/z_i < 0.1$) due to the upslope westward wind, and negative between $z_r/z_i \cong 0.1$ and 0.7 due to the strong vertical shear of the induced valley flow. The upper maximum at about $z_r/z_i = 2.2$ may be due to the presence of gravity waves. The shear contribution from $\overline{v'w'}$ (Fig. 5.13b) is less important and limited to the levels below $z_r/z_i \cong 0.5$. The vertical profile of the kinematic heat flux (Fig. 5.13c) shows a nearly linear decrease with height as a typical convection PBL; however, unlike a typical CBL, there is little negative buoyancy flux at the PBL top, due to the weak capping inversion layer (see Fig. 5.8) as a result of the interaction with the horizontal breeze and the effect of the return current.

The above second moments profiles also show that the resolved part of turbulence dominates the subgrid-scale part except at the first few levels close to the

ground (below $z_r/z_i \cong 0.1$) where the grid spacing, even with a vertically stretched grid, is still not fine enough to fully resolve the energy-containing eddies.
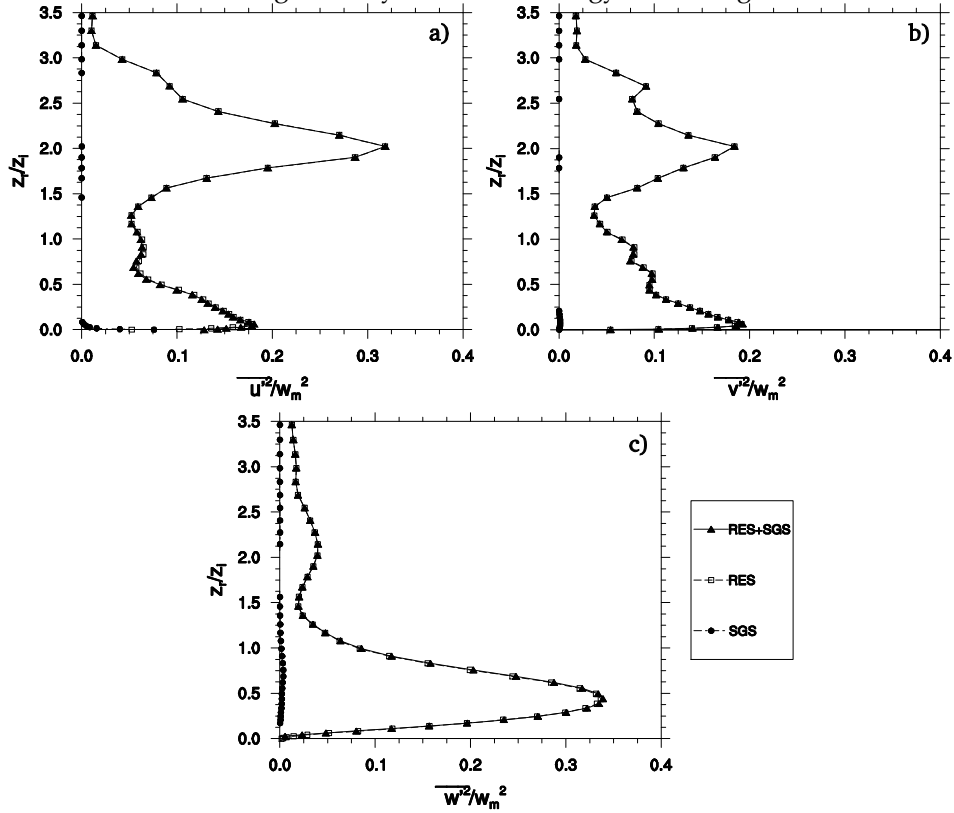
Fig. 5.12. Normalized vertical profiles of the variances: $\overline{u'^2}\big/w_m^{\,2}$ (a), $\overline{v'^2}\big/w_m^{\,2}$ (b), $\overline{w'^2}\big/w_m^{\,2}$ (c) at x = 5000 m at t = 7 h for Case 1 (V_g = 2 m/s). Open squares/ dashed lines represent the resolved contribution, filled circles/ dash-dotted lines shows the subgrid-scale contribution, filled triangles/ full lines represent the total variable.
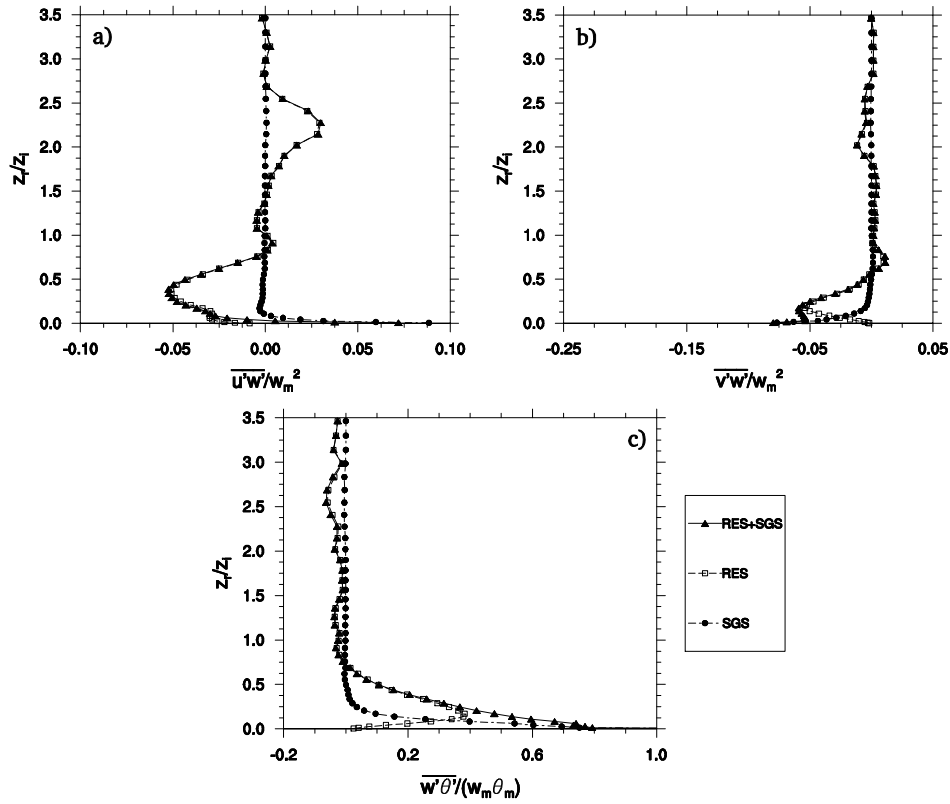
Fig. 5.13. Normalized vertical profiles of the fluxes: $\overline{w'\theta'}/\left(w_m\theta_m\right)$ **(a)**, $\overline{u'w'}/w_m^2$ **(b)**, $\overline{v'w'}/w_m^2$ **(c)** at x = 5000 m at t = 7 h for Case 1 (V$_g$ = 2 m/s). Open squares/ dashed lines represent the resolved contribution, filled circles/ dash-dotted lines shows the subgrid-scale contribution, filled triangles/ full lines represent the total variable.

5.2.6 TKE budget analysis

To clarify the nature of the turbulence, the TKE budget is analyzed in this section. The governing equation for the total (resolved+sgs) turbulent kinetic energy E is:

$$\frac{\partial E}{\partial t} = -\underbrace{\left(\overline{u}\frac{\partial E}{\partial x} + \overline{w}\frac{\partial E}{\partial z}\right)}_{I} +$$

$$-\underbrace{\left(\overline{u'^2}\frac{\partial \overline{u}}{\partial x} + \overline{u'w'}\frac{\partial \overline{w}}{\partial x} + \overline{u'v'}\frac{\partial \overline{v}}{\partial x} + \overline{w'^2}\frac{\partial \overline{w}}{\partial z} + \overline{u'w'}\frac{\partial \overline{u}}{\partial z} + \overline{v'w'}\frac{\partial \overline{v}}{\partial z}\right)}_{II} + \underbrace{\frac{g}{\theta}\overline{w'\theta'}}_{III} +$$

$$-\underbrace{\left\{\frac{\partial}{\partial x}\left[\overline{u'\left(E+\frac{p'}{\rho}\right)}\right] + \frac{\partial}{\partial z}\left[\overline{w'\left(E+\frac{p'}{\rho}\right)}\right]\right\} + \overline{\left(E+\frac{p'}{\rho}\right)\left(\frac{\partial u'}{\partial x} + \frac{\partial v'}{\partial y} + \frac{\partial w'}{\partial z}\right)}}_{IV} - \varepsilon$$

(5.2)

with ρ and p deviations from the background hydrostatic profiles of density ρ_0 and pressure p_0. The terms in I represent the horizontal (ADV_h) and vertical (ADV_v) advection, II contains the horizontal and vertical shear production (S), III the buoyancy production (B), and the last term ε accounts for small-scale dissipation. The first two terms in IV represent the horizontal and vertical redistribution of turbulence by pressure fluctuations (P) and turbulent transport (T), while the last term represents the return-to-isotropy contribution, which should be zero for an incompressible flow field. In the above equation we have implicitly neglected, for simplicity, the advection and shear generation along y. The horizontal shear production (first three terms of II) are negligible in all analyzed locations (not shown), despite the fact that $\overline{u'v'}$ (Fig. 5.11d) is large and varying from location to location; this is because $\overline{u'v'}$ and $\frac{\partial v}{\partial x}$ are poorly correlated.

WRF is a compressible model and the pressure field is computed diagnostically from the equation of state. We checked the flow divergence $\nabla \cdot \mathbf{V} = \frac{\partial u}{\partial x} + \frac{\partial v}{\partial y} + \frac{\partial w}{\partial z}$ and found its magnitude significant (on the order of 10^{-4} s^{-1}) even in the shallow PBL. The divergence field is almost uniform in y (not shown). The y-average of the flow divergence is shown in Fig. 5.14; it reveals wavy structures characterized by alternating bands of positive and negative values with about 30° orientation with respect to the ground. A large band is observed above the plateau, in correspondence of the region characterized by large negative buoyancy (Fig. 5.11a). The kink at the top of the slope can be an effect of the pressure coordinate due to the sharp change of terrain inclination. With this large flow divergence field, we cannot separate the turbulent pressure fluctuations from those due to flow compressibility. Hence we will not calculate the pressure term P.
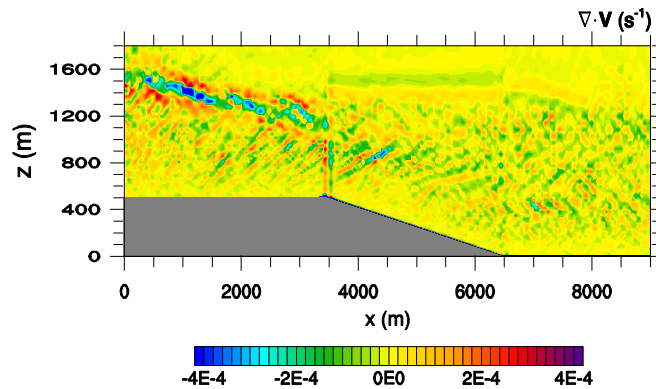
Fig. 5.14. Vertical cross section of the averaged divergence of the wind field at t = 7 h for Case 1 (V_g = 2 m/s).

To better characterize the nature of turbulence and to intercompare their profiles in different zones of the domain, the budget terms in Fig. 5.15 are normalized by

w_m^3/z_i . Also, to show the relative importance of shear and buoyancy in determining the regime of the PBL, plots have been labeled with Deardorff's stability parameter z_i/L, where L is the Monin-Obukhov length. The upper boundaries of the vertical axis in Fig. 5.15a and b reach the top of the domain.
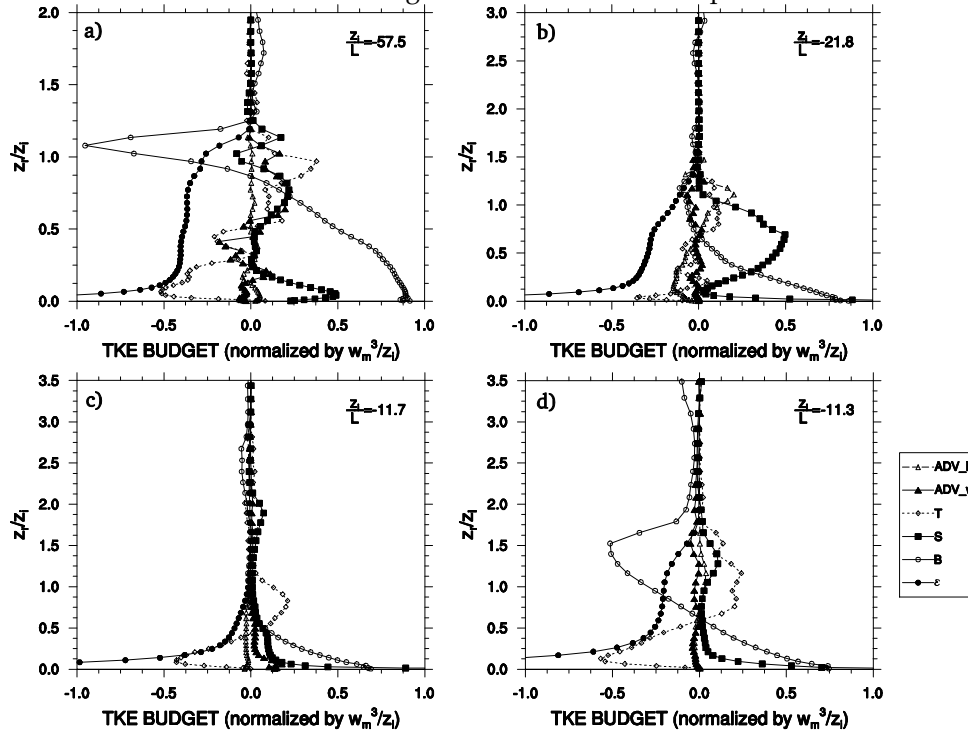
Fig. 5.15. Normalized vertical profiles of the TKE budget: x = 250 m (a), x = 1750 m (b), x = 5000 m (c), x = 9000 m (d) at t = 7 h for Case 1 (V$_g$ = 2 m/s). The curves represent the different terms in (11): ε (filled circles/ full lines) is the dissipation, B (open circles/ full lines) is the buoyancy, S (filled squares/ full lines) is the shear production, T (open diamonds/ dotted lines) is the turbulent transport, ADV_v (filled triangles/ full lines) and ADV_h (open triangles/ dashed lines) are, respectively, the vertical and horizontal advection terms. The stability parameter z_i/L, where L is the Monin-Obukhov length, shows the presence of different regimes over the domain.

Comparing the four figures in Fig. 5.15, which represent four selected locations, reveals significantly different TKE budgets, even though they are all taken at the same time period (t = 7 h). At the west-end boundary (x = 250 m), buoyancy production and small-scale dissipation are the two major terms in the TKE budget (Fig. 5.15a). This is consistent with the extremely negative stability parameter, z_i/L = -57.5. However, due to the presence of a strong updraft (Fig. 5.7c), along with a significant negative vertical gradient of TKE in the upper half of the PBL (Fig. 5.10a), there is also a significant contribution from shear production S, turbulence transport T and vertical advection. A thick negative buoyancy flux layer of ~ 300 m is also present between $z_r/z_i \cong 0.8$ and 1.2; such unusual large negative B has also been reported by Patton et al. (2005) in their LES of a flat terrain with surface

heterogeneities. We cannot find any budget term to balance this large negative buoyancy and will discuss this later.

At x = 1750 m (Fig. 5.15b), which is still over the ridge but has a strong influence from the valley-flow circulation, the vertical shear production becomes the primary source of TKE between $z_r/z_i \cong 0.3$ and 1.2, while buoyancy dominates only in the lower part of the PBL. Note that the PBL at this location has a stability parameter z_i/L = -21.8 that according to Deardorff (1972) should be dominated by buoyancy production. The horizontal advection is also significant; it is negative in the lower half of the PBL but positive in the upper part. The redistribution term T is quite small, except very close to the surface.

In the middle of the slope at x = 5000 m (Fig. 5.15c), the TKE budget is dominated by buoyancy production and small-scale dissipation in the lower half of the PBL. Near the ground (up to $z_r/z_i \cong 0.3$), positive contributions from vertical shear and vertical advection are also significant. A significant redistribution of energy by turbulent transport from the lower half to the upper part of the PBL is also observed as in other three locations; this term is likely to be counterbalanced somewhat by the pressure redistribution P in the CBL (Moeng and Sullivan 1994) but unfortunately the P term cannot be estimated from the WRF output as mentioned before.

In the middle of the valley (Fig. 5.15d) both buoyancy and shear are large production terms below $z_r/z_i \cong 0.5$, although buoyancy is still the prevailing one. Above 0.5 z_i, buoyancy becomes a large sink for TKE; the large TKE sink between $z_r/z_i \cong 0.5$ and 1.7 is only partially balanced by the vertical transport of turbulence and the shear production. Advection plays a negligible role in the budget in the valley. A local maximum of shear production can be observed at $z_r/z_i \cong 1.3$, which is induced by the vertical shear of mean v as evidenced from Fig. 5.7b. The stability parameter over the valley is comparable to that over the slope but their budgets (Fig. 5.15c and d) are similar only in the lower half of the PBL. The major difference in the TKE budgets above z_r/z_i = 0.5 in these two locations is dominated by the much larger negative buoyancy term associated with the very strong capping inversion over the valley. This unusually large negative buoyancy in the capping inversion is also observed at x = 250 m.

To better clarify the nature of the large negative buoyancy in the inversion layers at x = 250 m and x = 9000 m, a quadrant analysis of the vertical kinematic heat flux has been performed following Sullivan et al. (1998). Fig. 5.16 shows the resolved contribution of the normalized kinematic heat flux from the four quadrants: $\overline{w^+\theta^+}$, $\overline{w^+\theta^-}$, $\overline{w^-\theta^-}$, $\overline{w^-\theta^+}$, where + and – represent the positive and negative fluctuations from the y averages, as well as the total fluxes. In both locations wave activity is present in the capping zone and above as suggested by Fig. 5.14. In the lower half of the PBL, the total flux is dominated by the two positive quadrants, particularly by $\overline{w^+\theta^+}$ at x = 250 m (Fig. 5.16a) due to the strong updrafts.
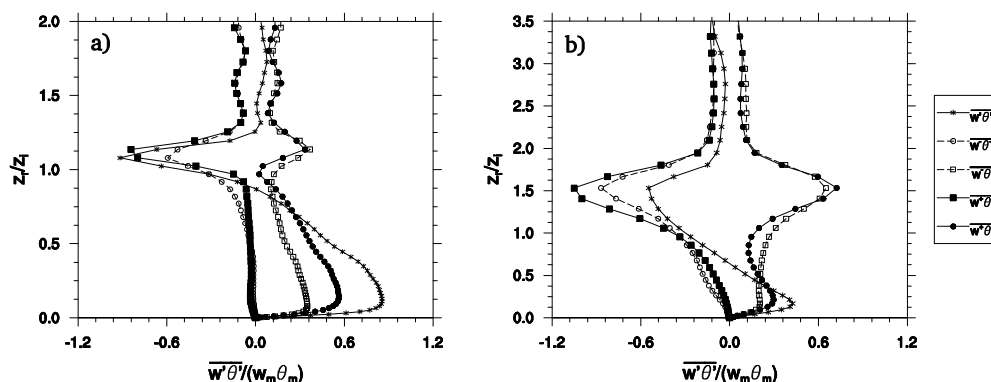
Fig. 5.16. Normalized vertical profiles of the buoyancy flux partitioned into four quadrants: x = 250 m (a), x = 9000 m (b) at t = 7 h for Case 1 (V$_g$ = 2 m/s). The signs + and – stand for the positive and negative fluctuations with respect to the y averages. The total resolved kinematic heat flux is shown by the asterisk/ full lines.

In the inversion layer at both locations, the two positive quadrants have similar magnitudes, so do the two negative quadrants, which suggest wave motions; however, the magnitudes of the two negative quadrants are much larger than those of the two positive quadrants, which then results in the very negative buoyancy flux there. Our quadrant distributions in the inversion layer also differ from those of the entrainment heat flux analyzed by Sullivan et al. (1998) where the entrainment flux is dominated by the second (cold air rising) and the third (cold air sinking) quadrants. This seems to suggest that our negative heat flux is not due to entrainment. This puzzling negative heat flux in the inversion layer results in an unbalanced TKE budgets. We have tried to look for mechanisms to explain the large negative B and to balance the TKE budgets but failed. This problem may be physical, relating to the induced valley flow circulation, but may also be just a WRF model problem due to its compressibility as indicated in Fig. 5.14. As will be shown in the next section, this large negative buoyancy and the associated imbalance in the TKE budget is not observed in presence of a stronger along-valley wind. This might be connected to the less important role played by pressure fluctuations as the shear production terms increase. Further investigation is needed.

5.3 Influence of a strong geostrophic wind along the valley

Next, we examine Case 2, which has a stronger geostrophic wind V$_g$ = 10 m/s compared to Case 1; all other parameters of the two simulations remain the same. Our discussion below will focus mainly on the differences between the two cases to signify the effect of geostrophic forcing. Fig. 5.17 shows the time evolution of the surface kinematic heat flux for Case 2. The maximum values are roughly the same as those in Case 1 (Fig. 5.2) but appear one hour earlier. Again, after 9.5 hours the positive surface heat flux vanishes everywhere in the domain; however, the sign change occurs earlier (at about 6.5 h) over the valley. So, at t = 7 h we have unstable PBLs over the ridges and the slopes, but a weakly stable PBL over the valley. Just like Case 1, the most negative heat flux occurs over the slopes at t = 11 h, but with a much larger magnitude; this time period coincides with the onset of katabatic winds

(not shown). The differences between the two cases can be explained by the feedbacks between shear and buoyancy forces. The kinematic surface heat flux is given by:

$$\overline{w'\theta'}_s = ku_* \left(\theta_s - \theta_1\right)\frac{1}{\phi_h} \tag{5.3}$$

where k is the Von Karman constant, θ_1 is the temperature at the first model layer and ϕ_h is the stability function for temperature. Initially, shear contributes to enhance u_* and thus $\overline{w'\theta'}_s$. Later on, when the mixed layer grows up, the shear generated by the geostrophic wind is reduced (because $\frac{\partial v}{\partial z}$ becomes smaller). The shear generated by the baroclinic circulation is instead sustained by the surface temperature increase. This explains why the maximum values of the surface heat flux are reached earlier in Case 2 but are roughly the same for both cases. The transport of warm air from the upper levels toward the ground by subsidence in the valley causes the decrease of $\left(\theta_s - \theta_1\right)$ and hence of the surface heat flux. In addition, as shown later, the capping inversion over the valley is much stronger in Case 1, which effectively isolates the warm inversion air from reaching to the first grid level. Thus, over the valley the sign change of $\left(\theta_s - \theta_1\right)$ occurs later in Case 1. In other regions of the domain, the sign change of the surface heat flux occurs at the same time in both simulations. When the surface heat flux becomes negative, its magnitude is increased by the wind shear. A negative value of $\overline{w'\theta'}_s$ drives the onset of katabatic winds over the slopes. The other shear source in moderately stable conditions is the geostrophic forced wind shear. Therefore, the higher negative values are observed in Case 2 over the slopes.
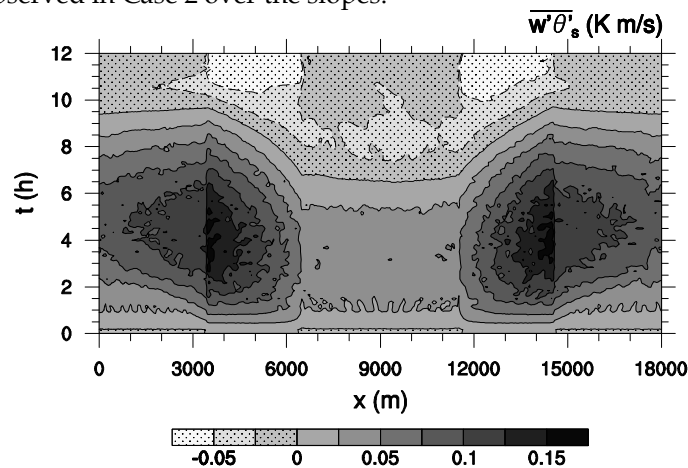
Fig. 5.17. Hovmöller plot of the y-averaged surface kinematic heat flux for Case 2 ($V_g = 10$ m/s).
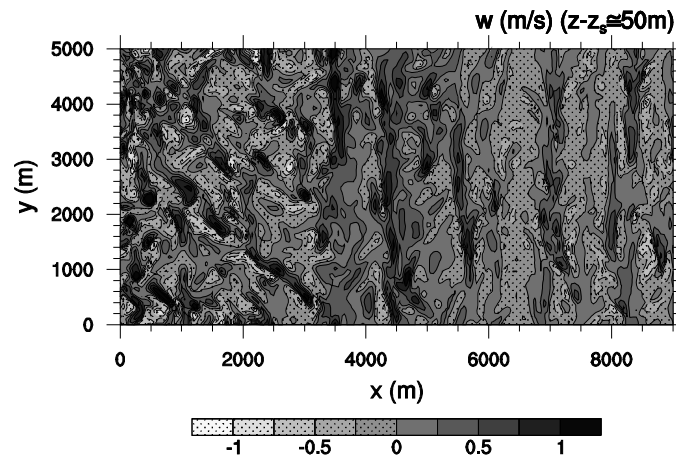
Fig. 5.18. Instantaneous horizontal cross section of the vertical velocity at t = 7 h for Case 2 (V_g = 10 m/s), at a fixed relative height from the ground.

The horizontal cross section of the instantaneous field of vertical velocity 50 m above the ground (Fig. 5.18) reveals two distinct flow features: (1) over the ridge the combined effect of the along-x mesoscale circulation and the along-y geostrophically forced wind results in structures approximately oriented along a 45° angle from the x axis, although the cellular pattern is still present near the west-end boundary; (2) over the slope and the valley large streaks are clearly aligned with the geostrophically forced wind, giving evidence that turbulence in this region of the domain is dominated by shear.

Fig. 5.19 shows the distribution of mean winds for Case 2. The thermally driven mean circulation is similar to that in Case 1, but with a stronger anabatic wind, a weaker return current and a weaker horizontal breeze (Fig. 5.19a). Also, its return current is thicker, extending up to 1700 m, while the depth of the upslope wind remains equal to that of Case 1. The mean v wind (Fig. 5.19b) shows no tunneling over the valley due to the lack of a capping inversion layer (Fig. 5.20). The mean vertical velocity (Fig. 5.19c) reveals a stronger updraft over the west-end of the ridge than that in Case 1. It also shows several updrafts along the slopes and in the valley; these updrafts are associated with the streaks along y shown in Fig. 5.18 over the foot of the slope and the valley, which extend vertically up to the entire PBL depth. Of particular evidence is a counterclockwise vortex street along the foot of the slope, which extends horizontally from x ≅ 6200 m to x ≅ 7500 m.
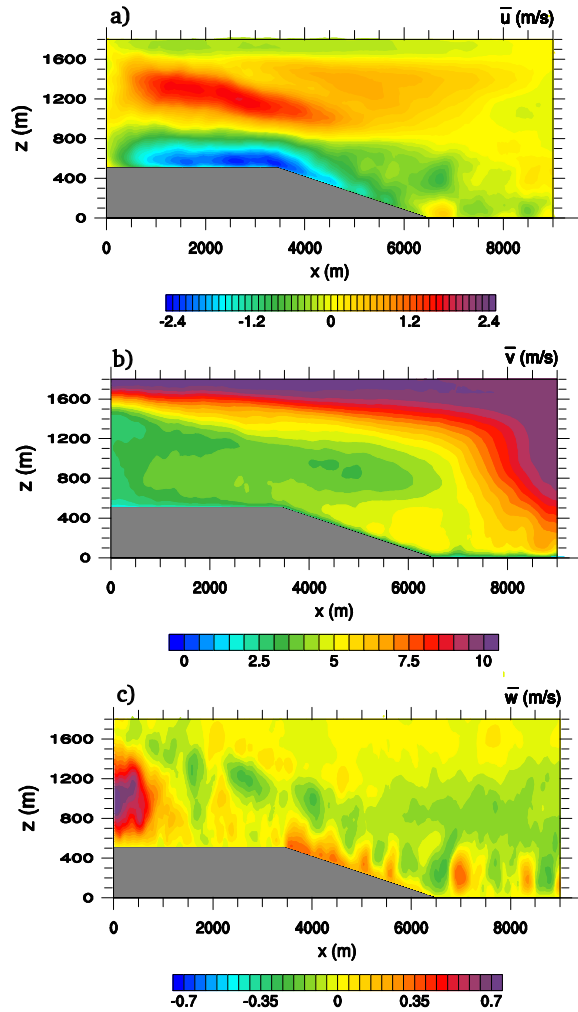
Fig. 5.19. Averaged vertical cross sections: $\overline{u}$ (a), $\overline{v}$ (b), $\overline{w}$ (c) at t = 7 h for Case 2 (V_g = 10 m/s).
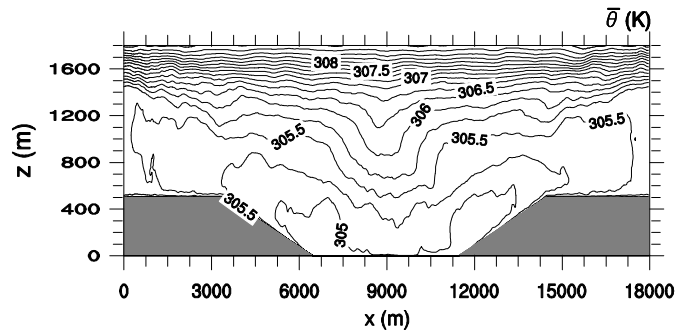
Fig. 5.20. Averaged vertical cross section of isotherms at t = 7 h for Case 2 (V_g = 10 m/s).

Fig. 5.21 illustrates the temporal evolution of the PBL height z_i, as determined by the method described in subsection 3d. The stronger shear in Case 2 makes the field much more irregular than that in Case 1, particularly with the formation of streaks and roll-like structures. On average z_i grows faster and reaches higher levels compared to Case 1, in agreement with the observations taken for various strongly sheared CBLs by Fedorovich and Conzemius (2008). The maximum value of $z_i \cong 950$ m (vs. $\cong 850$ m in Case 1) is attained at t = 7 h near the side boundaries over the ridges and it persists until hour 9; after that time a sharp decrease of the PBL height accompanies the vanishing of the positive surface heat flux over the ridges (Fig. 5.17). The plot also shows a deepening of the PBL in proximity of the feet of the slopes during the transition to the weakly stable regime occurring from hour 7 to hour 9; here the depth of about 600 m is associated with the formation of two-dimensional rolls, as evidenced from the mean wind fields (Fig. 5.19a and c). These large 2D rolls persist and even grow in depth from t = 7 h to 9 h (not shown).
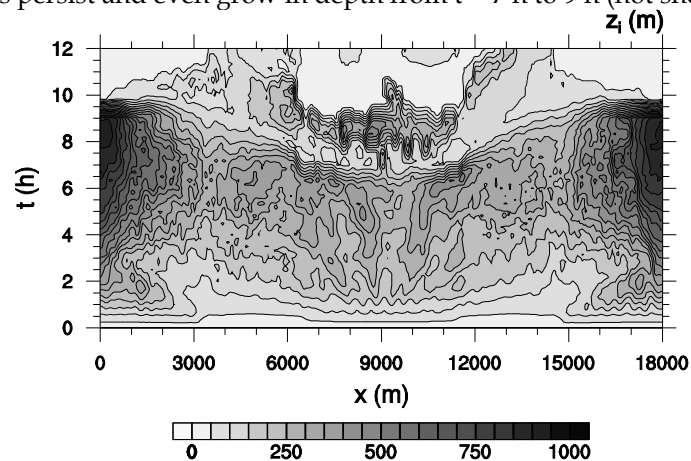
Fig. 5.21. Hovmöller plot of the PBL depth z_i for Case 2 (V_g = 10 m/s).

Fig. 5.22 shows a vertical cross section of the total TKE, the wind vectors, and the PBL depth. Maximum turbulence values are about 1.7 times higher than those in Case 1 (Fig. 5.10a), confirming the noticeable influence of the wind shear, especially in the upper part of the PBL. Like in Case 1, the maximum TKE occurs near the west-end boundary; but in Case 2 a second peak of TKE near the west-end boundary occurs at $\cong 1600$ m, which will be discussed later. A fairly good correlation between z_i and the level where TKE decreases significantly is observed only over the slope and the eastern part of the ridge, where z_i again reveals an angle close to the slope inclination. Surprisingly, the large 2D roll along y near the foot of the slope is not associated with intense turbulence, while the other roll-like structures (associated with mean updrafts in Fig. 5.19c) over the valley carry a higher energetic content.
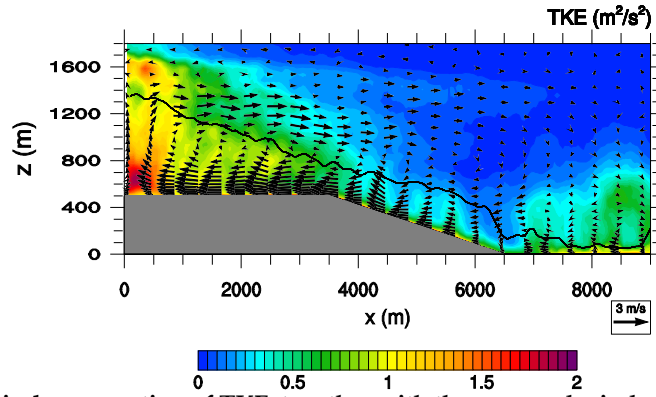
Fig. 5.22. Vertical cross section of TKE, together with the averaged wind vectors at t = 7 h for Case 2 (V_g = 10 m/s): the black line delineates the PBL depth.
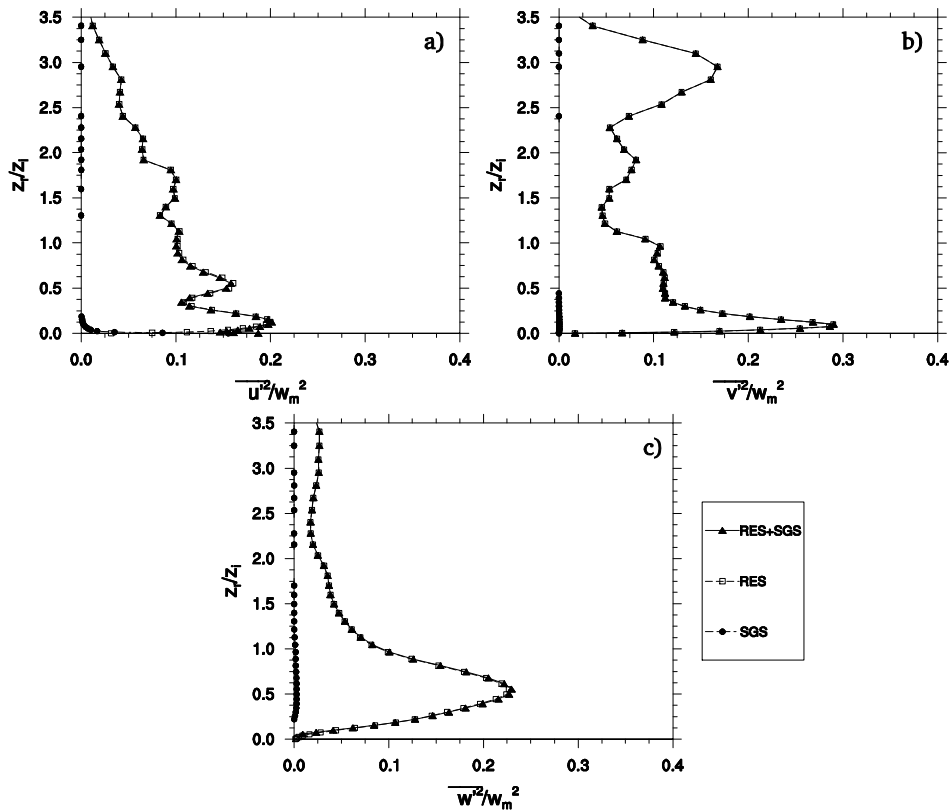
Fig. 5.23. Normalized vertical profiles of the variances: $\overline{u'^2}/w_m^2$ **(a),** $\overline{v'^2}/w_m^2$ **(b),** $\overline{w'^2}/w_m^2$ **(c) at x = 5000 m at t = 7 h for Case 2 (V_g = 10 m/s). Open squares/ dashed lines represent the resolved contribution, filled circles/ dash-dotted lines shows the subgrid-scale contribution, filled triangles/ full lines represent the total variable.**

Next we apply the scaling described in subsection 3e to the vertical profiles of second-moment statistics, again taken in the middle of the slope (where the surface

heat flux is still positive). The lower maximum of the u variance (Fig. 5.23a) is slightly more intense than that in Case 1. The secondary maximum in Case 1 above the PBL disappears here, which will be shown later to relate to the strong geostrophic wind which reduces the horizontal advection along x. The v variance profile (Fig. 5.23b) is similar to Case 1, although the surface maximum is 1.5 times larger and the upper peak is shifted upward to $z_r/z_i \cong 3$; this shift can be explained by the presence of an intense wind shear at this level. As expected for a less buoyancy dominant PBL, the normalized vertical velocity variance (Fig. 5.23c) peak is less intense than that of Case 1 and locates higher up to $z_r/z_i \cong 0.5$, which agree with the LES results obtained by Sorbjan (2004) of a strongly sheared baroclinic CBL.
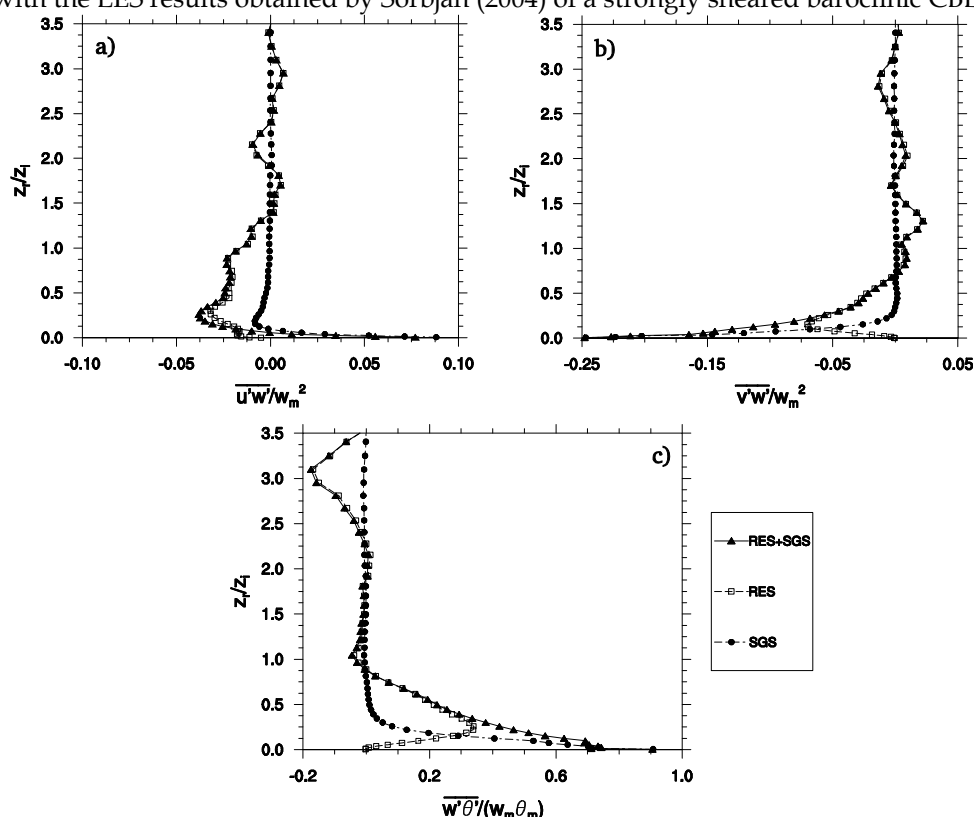
Fig. 5.24. Normalized vertical profiles of the fluxes: $\overline{w'\theta'}/(w_m \theta_m)$ (a), $\overline{u'w'}/w_m^2$ (b), $\overline{v'w'}/w_m^2$ (c) at x = 5000 m at t = 7 h for Case 2 (V_g = 10 m/s). Open squares/ dashed lines represent the resolved contribution, filled circles/ dash-dotted lines shows the subgrid-scale contribution, filled triangles/ full lines represent the total variable.

The normalized $\overline{u'w'}$ profile (Fig. 5.24a) is similar to that of Case 1, but the negative value is smaller and extends up to the top of the PBL; also, the secondary peak in Case 1 at $z_r/z_i \cong 2.2$ is not present here. Vigorous surface shear is shown in $\overline{v'w'}$ profile (Fig. 5.24b) up to half of the PBL depth; the magnitudes are about 2.5 times higher than those in Case 1. A modest positive flux is shown just above the

height of the PBL, which may be associated to the presence of gravity waves. It is interesting to note that in this case such upper-level secondary large flux appears in the v-flux profile, while in case of weak geostrophic condition the secondary large flux shows up in the u-flux. The kinematic heat flux (Fig. 5.24c) is similar to that in Case 1 except the presence of a deep negative-flux layer between $z_r/z_i \cong 2.5$ and 3.5; as shown later, this is related to the strong shear generation of turbulence at this level.

The normalized TKE budgets at various locations are shown in Fig. 5.25. Again, they differ significantly from location to location. In the middle of the ridge (Fig. 5.25a) the buoyancy production is important in the lower half of the domain, while the vertical shear dominates in both the surface layer and the upper half of the PBL. An entrainment layer (i.e., the negative buoyancy flux layer) is present between $z_r/z_i \cong 1.5$ and 2. Horizontal advection is negative in the lower half of the PBL and becomes positive above $z_r \cong z_i$. Between $z_r/z_i \cong 1$ and 2 both horizontal advection and vertical shear are major production of TKE, which balance the dissipation and the negative buoyancy. The stability parameter z_i/L = -6.6 still indicates an unstable regime, but its magnitude is about 3 times smaller than that in Case 1 due to the increasing importance of the surface shear. The redistribution by turbulence transport is negative below $z_r/z_i \cong 0.8$ and positive up to $z_r/z_i \cong 2$.

In the middle of the slope (Fig. 5.25b) the most important contributions to the production of turbulence are the shear and the vertical advection up to $z_r/z_i \cong 0.2$. In the remaining part of the PBL, buoyancy prevails. At $z_r/z_i \cong 3$, in correspondence to the interface between the return current and the stratified atmosphere above, buoyancy destruction in the entrainment zone is nearly balanced by the shear.

In the middle of the valley (Fig. 5.25c) we have near neutral conditions (z_i/L = 0.2) and hence friction velocity is the appropriate parameter for scaling the TKE budget profiles. The small-scale dissipation nearly balances the shear production, which is typical of a near-neutral PBL (e.g., Moeng and Sullivan 1994).

It is worth noting that Case 2 does not show any imbalance in the TKE budget at any location. This may be due to a less importance role of pressure fluctuations in a stronger shear case.
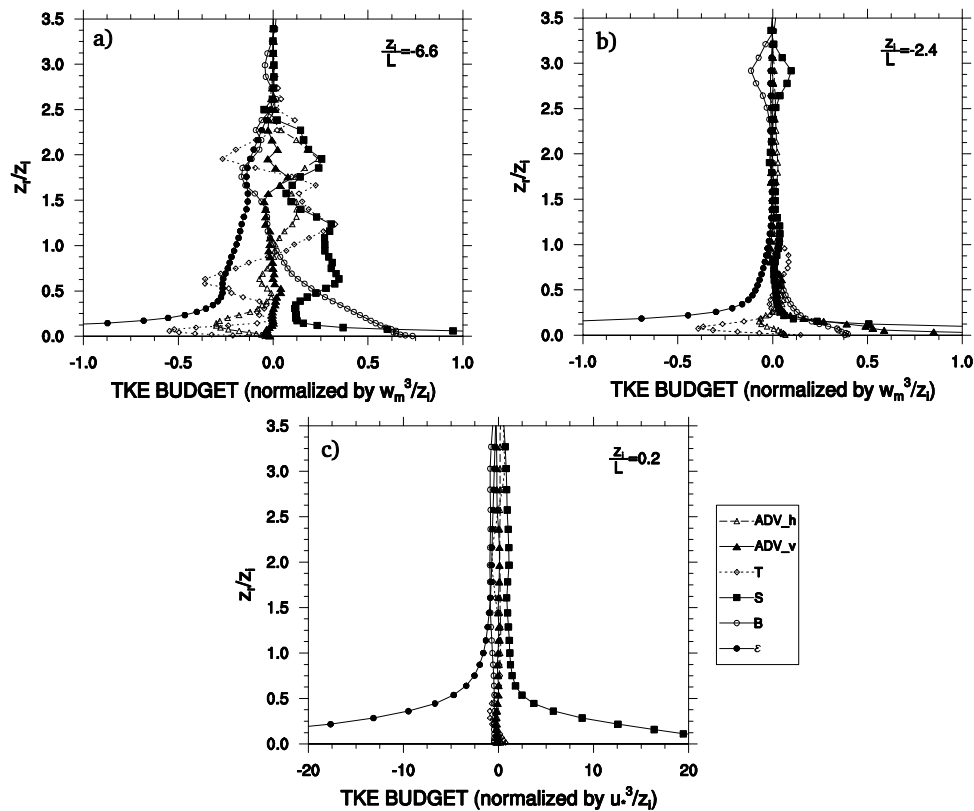
Fig. 5.25. Normalized vertical profiles of the TKE budget: x = 1750 m (a), x = 5000 m (b), x = 9000 m (c) at t = 7 h for Case 2 (V_g = 10 m/s). The curves represent the different terms in (11): ε (filled circles/ full lines) is the dissipation, B (open circles/ full lines) is the buoyancy, S (filled squares/ full lines) is the shear production, T (open diamonds/ dotted lines) is the turbulent transport, ADV_v (filled triangles/ full lines) and ADV_h (open triangles/ dashed lines) are, respectively, the vertical and horizontal advection terms. The stability parameter z_i/L, where L is the Monin-Obukhov length, shows the presence of different regimes over the domain.

5.4   Summary

The turbulent structure of a complex baroclinic PBL driven by (1) surface heating and (2) along-valley geostrophic wind V_g is investigated by means of the LES technique. The three-dimensional non-hydrostatic meteorological model WRF is modified to include new formulation for the SGS filter width. Ridge-valley topography, symmetrical in x and uniform in y, is simulated with an LES grid resolution to explicitly resolve the energy-containing turbulent eddies. The thermally driven circulation is generated by imposing a sinusoidal time change of the surface temperature; the surface heat and momentum fluxes are then computed based on Monin-Obukhov surface similarity theory. The approach enables the model to generate a surface heat flux that responds and couples to the valley-flow circulation. In this study we focus on the daytime circulation, i.e., the upslope flow.

Two cases are simulated with different V_g (2 m/s and 10 m/s) to investigate the influence of geostrophic wind on valley flows and their turbulence properties.

Turbulence statistics vary from location to location due to topography. We define the ensemble statistics as averages along y (along the valley) and also over a time period of 40 minutes. The first-moment statistics show the characteristics of the mean flow, which consists of two symmetrical upslope circulations. The surface kinematic heat flux reveals complicated time and space distributions: the largest positive surface flux occurs about two hours before the maximum ground temperature; during the transition from anabatic to katabatic flows the largest negative flux occurs near the foot of the slope. Both cases show some characteristic features: the PBL over the ridge is much deeper than that in the valley and the growth line of the PBL over the slope (and even extending into the ridge) roughly corresponds to the slope angle.

The PBL structure differs from the idealized CBL over a uniform surface. Even when the stability parameter indicates a very unstable CBL, the shear production is as important as (or even dominates) the buoyancy production in generating turbulence in many regions, particularly over the ridge where the valley-flow circulation creates a strong vertical shear of the mean u. The TKE budgets vary significantly at different regions among ridge, slope and valley.

In the case with V_g = 2 m/s, a horizontal breeze, from valley towards the ridge, appears near the top of the PBL (which happens to be at about the ridge height) over the valley and extends to the slope region. This breeze merges with the anabatic flow and significantly deepens the upslope flow at the top of the slope. The horizontal breeze, along with the return current, also leads to a secondary circulation over the valley, which may significantly impact the vertical distribution of air pollution in the valley. Associated with this westward horizontal breeze is a strong northward wind (tunneling along the valley) again at about the ridge height. In the case with V_g = 10 m/s, the horizontal breeze is weaker and the tunneling wind disappears, which may be due to the change in strength and height of the capping inversion over the valley.

In the case with V_g = 2 m/s, a strong capping inversion forms over the valley at $\cong$ 400 m, which is about the ridge height, as a result of the strong subsidence induced by the return current of the thermal circulation. This capping inversion weakens in the case with V_g = 10 m/s because of (1) a deeper earlier CBL over the valley, which grows above the ridge height and (2) the formation of two-dimensional roll-like structure over the valley and at the foot of the slope due to larger shear during the transition to the stable regime.

In the case with V_g = 2 m/s, the TKE over the slope exhibits a secondary peak above the PBL due to the horizontal advection of turbulence (carried by the return current), which may significantly affect the dispersion process there. With strong geostrophic wind forcing, this horizontal advection effect is much reduced, but a large v-variance appears at $z_r \cong 3z_i$ over the slope due to the much stronger shear at that level.

Over the slope, the CBL reveals some unusual features. For example, in both cases, the capping inversion at the top of the CBL is largely diminished due to the formation of the horizontal breeze and the return current. In the case with $V_g = 10$ m/s, an entrainment heat flux occurs at the interface between the return current and the stratified atmosphere above, around $z_r \cong 3z_i$, where the negative buoyancy balances the shear production of TKE.

It should be observed that, since the orography and the forcings in the present study are idealized, some of the details of the circulation and the turbulence structure might not be transferrable to real valleys, also due to the effect of different synoptic conditions.

In this study, we show that the LES technique can be used to study higher-moment turbulence statistics such as variances, fluxes, TKE budgets, and how they distribute over different regions of a complex terrain. Despite the fact that these higher moment statistics are of great importance to PBL applications such as air pollution and wind farm siting, they have not been thoroughly investigated at a spatial resolution as high as 50 m in previous LES studies over variable orography.

6 Conclusions

The simulation of the atmospheric circulation over a heterogeneous terrain involves the modeling of a number of phenomena occurring at different scales. The analysis of the different turbulence closure techniques, presented in Chapter 2, evidenced that the main advantage of the LES methodology relies in its ability to model only the small scales; a higher energetic content is generally resolved and the influence of the subgrid contributions on the resolved scales is less important than with the RANS technique. Nevertheless, the need to model highly anisotropic wall structures with non uniform vertical grids requires a particular care in the definition of the filter width. Starting from considerations about the theoretical spectrum it is possible to derive an expression for the filter width which takes into account the grid anisotropy. We introduced this modification into the TKE subgrid scale model of WRF and tested against the filtered Kolmogorov spectrum; as discussed in Chapter 4, this formulation of the filter width results in a closer agreement with the theoretical predictions.

Past LES studies introduced the surface heat forcing by directly imposing the surface heat flux as a source term in the thermal energy balance equation. This formulation does not take into account the coupling between heat and momentum fluxes in the surface layer. We proposed a more realistic bottom boundary condition obtained coupling the LES model with a surface layer scheme based on the Monin-Obukhov similarity theory. The results of Chapters 4 and 5 show that this method allows to reproduce the differential heating of zones with different flow characteristics.

We evidenced the occurrence of coherent structures in the valley atmosphere. During the daytime we have: (1) an anabatic current over the slopes; (2) a horizontal breeze directed from the center of the valley toward the slopes; (3) a strong updraft and an associated intense roll vortex over the ridges; (4) a region characterized by a free convection regime over the ridges away from the slopes and at the bottom of the valley; (5) a return current in the upper part of the domain directed from the ridges toward the center of the valley; (6) a deep subsidence region over the basin which closes the overall circulation. During the nighttime period we have: (1) a stable layer develops in the valley (cold pool), thus eroding the residual layer just above; (2) the development of downslope currents, flowing from the top of the two ridges; (3) the absence of a significant return current.

We emphasize here that the horizontal breeze, along with the return current, leads to a secondary circulation over the valley, which may significantly impact the vertical distribution of air pollution in the valley. In case of a weak geostrophic wind forcing directed along the valley axis, a strong northward wind tunneling along the

valley at about the ridge height is associated with the horizontal breeze. In the case with a strong geostrophic wind forcing the horizontal breeze is weaker and the tunneling wind disappears.

Turbulence statistics vary from location to location due to orography. The PBL over the ridge is much deeper than that in the valley. The growth line of the PBL over the slope (and even extending into the ridge) roughly corresponds to the slope angle. Even when the stability parameter indicates a very unstable CBL, the shear production is important in generating turbulence in many regions. The TKE budgets vary significantly at different regions among ridge, slope and valley.

Previous LES studies of complex PBLs mainly investigated the mean fields. In this study, we studied higher-moment turbulence statistics such as variances, fluxes, TKE budgets, and how they distribute over different regions of a complex terrain. These higher moment statistics are of great importance to PBL applications such as air pollution and wind farms.

The results of this study shows that, even with a certain degree of idealization, spatial inhomogeneities in terrain elevation considerably modify the mechanisms of turbulence generation and redistribution under convective conditions, introducing significant shear production and advection terms in the TKE budget.

Imposing the surface temperature anomaly as the thermal forcing, even neglecting the interaction with the soil capacity, allows the coupling between surface thermal and momentum fluxes, which is a step toward the reproduction of real conditions where the surface heat flux over the slopes significantly differs from that over the valley or the ridges. In fact, most of the previous LES studies considered a constant stationary surface heat flux which is not realistic under variable terrain elevation.

The present non-stationary LES investigation revealed that the PBL characteristics (e. g. its depth and the stability regime) are governed by mechanisms that change during the daytime evolution, depending on the relative importance of thermal and shear forcing. This implies that different scaling parameters should be used in the analysis of turbulence statistics at different times of the day and also for the different regions of the domain, according to the local stability regime defined by the sign of z_i/L. Furthermore, the PBL height itself must be defined locally and its determination method depends on the sign of the surface heat flux.

Valley circulation is not explicitly reproduced by mesoscale models, whose fine grids have a horizontal grid spacing ≥ 1 km. Furthermore, currently used mesoscale PBL schemes are one-dimensional and do not include the effects of horizontal transport. It has been shown in the present investigation that the complex turbulence structure over a valley and its significant horizontal heterogeneity has a large impact on the mesoscale circulation, particularly the buoyancy fluxes redistribution; hence it should be included as additional source/sink terms in future PBL parameterization.

Future LES studies should investigate the effects of the valley circulation on the formation and distribution of clouds, including the role of moisture and its interaction with the observed significant buoyancy fluxes.

The parameters from the Hunt et al. (2003) and Manins and Sawford (1979) theoretical models were computed and compared with previous investigations, pointing out the effects of the geometry on the flow properties.

A thorough comparison with observations is an important step in order to confirm the findings of this study. Nevertheless, detailed and reliable data on both mean quantities and turbulence statistics are very difficult to obtain and such field campaign is beyond the scope of the present work. Also, we have focused on an idealized geometry which is not representative of real meteorological conditions.

Appendix A   Physics schemes

In the application of the models on different scales the phenomena characterized by dimensions smaller than the computational cell are not explicitly evaluated. Nevertheless, subgrid scale phenomena may have a significant influence on larger scales flows. Therefore, these effects must be taken into account by empirical or semi-empirical formulations, which are aimed to provide corrections to the meteorological fields resulting from the resolution of the governing equations in every point of the grid. The classification of the schemes for the physics is:

- Microphysics (MP);

- Convection (CP);

- Radiation (RA);

- Land Surface (LSM);

- Surface Layer (SFC);

- Planetary Boundary Layer (PBL).

Fig. A. 1 shows the flux diagram of the modeling system composed by governing equations and parametric schemes; the shaded lines indicate that that specific scheme is not activated for every integration step. $LW\uparrow$, $SW\uparrow$, $LW\downarrow$, $SW\downarrow$ are the infrared (LW) and visible (SW) radiation fluxes, the arrows indicate the direction of the fluxes (upward $\uparrow$ and downward $\downarrow$); P is the total rain, sum of the explicitly resolved contribution P_{RIS} and the part coming from the convective scheme P_{CONV}; the subscript $()_s$ denotes the surface layer variables, $()_0$ refers to ground values and $()_a$ denotes the variables defined at the first grid level; X_C and X_W are the mixing ratios for water vapor and condensed cloud water, respectively. The remaining variables will be defined in the following.
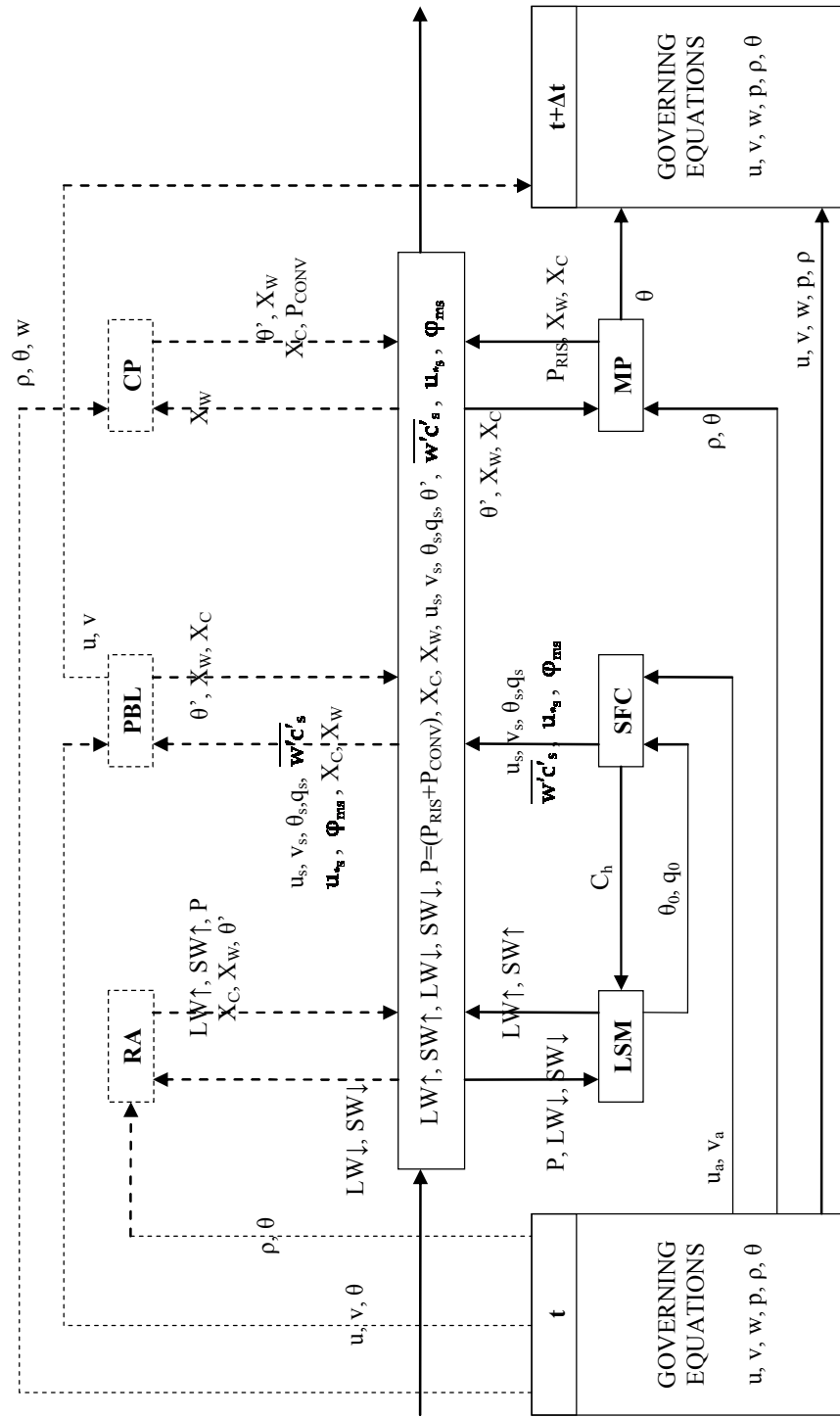
Fig. A. 1. Interactions of the physics with the governing equations between two subsequent time steps: the arrows show the incoming and outgoing variables as used by the different schemes.

A.1   Microphysics

Microphysics schemes model all the processes of the change of state of the water in the atmosphere; the formation and the evolution of clouds and precipitations. They are classified on the basis of the way they consider the changes of state of water.

We describe, as an example, the scheme of Lin et al. (1983) which considers five classes of hydrometeors: cloud water and cloud ice (under saturation conditions), rain, snow, hail. Snow is assumed for aggregates of ice crystals of 2 - 5 mm of diameter, a density of 0.05 - 0.89 g/cm^3 and a terminal velocity of 0.5 - 3 m/s; hail indicates aggregates characterized by a diameter larger than 5 mm, density of 0.8 - 0.9 g/cm^3 and terminal velocity of 10 - 40 m/s. The dimensions of the particles which compose snow and hail aggregates are assumed to be small enough to neglect their terminal velocities, thus considering only the terminal velocities of the respective aggregates. Fig. A. 2 shows a diagram of the model with all the parameterized processes and their interactions; the symbols are explained in Table A. 1.
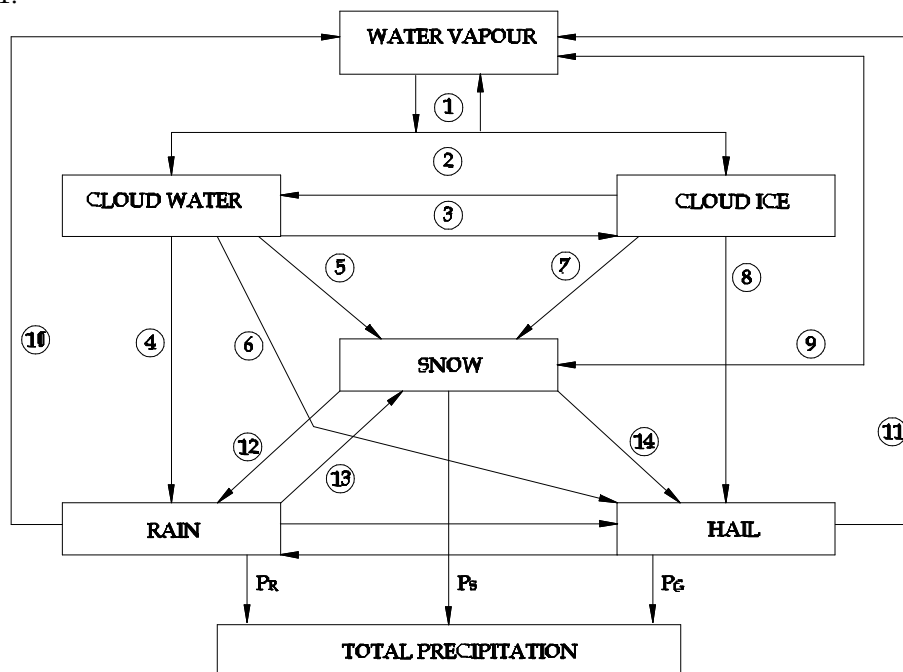
Fig. A. 2. Microphysics scheme of Lin et al. (1983): the circled numbers represent the modeled physical processes, described in Table A. 1; the arrows represent the transformation between two different states.

Symbol	Parameterized Process
①	– Condensation, evaporation, deposition and sublimation.
②	– Melting of cloud ice to form cloud water, T ≥ 0°C.
③	– Growth of cloud ice by deposition of cloud water; – Homogeneous cooling of cloud water to form cloud ice.
④	– Heterogeneous nucleation by collision and coalescence of water droplets; – Homogeneous nucleation; – Accretion of cloud water on snow particles; produces snow if T < 0°C, rain if T ≥ 0°C.
⑤	– Accretion of cloud water on snow particles; produces snow if T < 0°C, rain if T ≥ 0°C; – Bergeron processes (deposition and riming) to form snow.
⑥	– Accretion of cloud water on hail particles.
⑦	– Heterogeneous nucleation by collision and coalescence of cloud ice; – Accretion of cloud ice on snow particles; – Freezing of rain droplets which collide with cloud ice particles; produces snow if $X_R \leq 10^{-4} g/g$, hail if $X_R > 10^{-4} g/g$; – Autoconversion of cloud ice in snow via the growth of Bergeron nuclei (crystals of 50 μm diameter).
⑧	– Accretion of cloud ice on hail particles; – Freezing of rain droplets which collide with cloud ice particles; produces snow if $X_R \leq 10^{-4} g/g$, hail if $X_R > 10^{-4} g/g$.
⑨	– Accretion by deposition of snow particles at T < 0°C; – Sublimation of snow particles under unsaturated conditions.
⑩	– Evaporation of rain droplets under unsaturated conditions.
⑪	– Sublimation of hail particles under unsaturated conditions.
⑫	– Melting of snow particles to form rain, T ≥ 0°C.
⑬	– Accretion of rain droplets on cloud ice particles; produces hail if $X_R > 10^{-4} g/g$, $X_s \geq 10^{-4} g/g$ and T < 0°C. – Accretion of rain droplets on snow particles; with T < 0°C produces hail if $X_R \geq 10^{-4} g/g$ and $X_s \geq 10^{-4} g/g$, else generates snow. With T ≥ 0°C enhances snow melting.
⑭	– Heterogeneous nucleation by collision and coalescence of snow particles; – Accretion of snow particles on hail particles; produces hail; – Accretion of snow particles on rain droplets; produces hail if $X_R \geq 10^{-4} g/g$, $X_s \geq 10^{-4} g/g$ and T < 0°C.
⑮	– Accretion of rain droplets on hail particles; – Accretion of rain droplets on cloud ice particles; produces hail if $X_R \geq 10^{-4} g/g$, $X_s \geq 10^{-4} g/g$ and T < 0°C; – Freezing of rain droplets to form hail; – Accretion of rain droplets on snow particles; with T < 0°C produces hail if $X_R \geq 10^{-4} g/g$, $X_s \geq 10^{-4} g/g$, else generates snow. With T ≥ 0°C enhances snow melting.
⑯	– Melting of hail to form rain, T ≥ 0°C.

Table A. 1. Microphysics processes in the model of Lin et al. (1983).

An exponential distribution is assumed to describe the dimensions of the precipitating particles:

$$n_j\left(D_j\right)=n_{0j}e^{-\lambda_j D_j} \tag{A. 1}$$

where the subscript $_j$ refers to rain $(_{j\,=\,R})$, snow $(_{j\,=\,S})$ and hail $(_{j\,=\,G})$; n_{0j} indicates the intercepts with the axis $n_j\left(D_j\right)$ in a logarithmic plot. The values of the constants are:

- $n_{0R}=8\times10^{-2}cm^{-4}$ (Marshall and Palmer 1948);

- $n_{0S}=3\times10^{-2}cm^{-4}$ (Gunn and Marshall 1958);

- $n_{0G}=4\times10^{-4}cm^{-4}$ (Federer and Waldvogel 1975).

D_j represents the diameter of the particles. The slopes of the distributions λ_j are found, considering a unit air volume, multiplying (A. 1) by the parcel mass $\rho_j\pi\dfrac{D_j^3}{8}$, integrating over all the diameters between 0 and ∞ and imposing the result equal to the water content ρX_j:

$$\lambda_j=\left(\frac{\pi\rho_j n_{0j}}{\rho X_j}\right)^{0.25} \tag{A. 2}$$

where ρ and ρ_j are the air and hydrometeor densities, respectively; the snow density is set to 0.1 g/cm^3. X_j represent the mixing ratios for the three hydrometeors.

The terminal velocities for the single particles are given by:

$$U_{DR}=aD_R^b\sqrt{\frac{\rho_R}{\rho}} \tag{A. 3}$$

$$U_{DS}=cD_S^d\sqrt{\frac{\rho_S}{\rho}} \tag{A. 4}$$

$$U_{DG}=\sqrt{D_G\frac{4g\rho_G}{3\rho C_D}} \tag{A. 5}$$

The values for the constants are:

- $a=2115cm^{1-b}s^{-1}$; $b=0.8$ (Liu and Orville 1969);

- $c=152.93cm^{1-d}s^{-1}$; $d=0.25$ (Locatelli and Hobbs 1974);

- $C_D=0.6$ (Wisner et al. 1972).

In the computations the terminal velocities are averaged weighted by the mass, for the generic velocity:

$$U = \int_0^\infty \frac{U_D X(D)}{X} dD \tag{A. 6}$$

thus, for the three hydrometeors:

$$U_R = \frac{a\Gamma(4+b)}{6\lambda_R^b} \sqrt{\frac{\rho_R}{\rho}} \tag{A. 7}$$

$$U_S = \frac{c\Gamma(4+d)}{6\lambda_S^d} \sqrt{\frac{\rho_S}{\rho}} \tag{A. 8}$$

$$U_S = \frac{\Gamma(4.5)}{6\lambda_G^{0.5}} \sqrt{\frac{4}{3} \frac{g\rho_G}{\rho C_D}} \tag{A. 9}$$

where $\Gamma(\alpha) = \int_0^\infty D_j^{\alpha-1} e^{-D_j} dD_j$ (con $\alpha > 0$) is the gamma function.

The scheme provides empirical relations for each of the processes described in Table A. 1 as functions of the variables defined above; the terms P_R, P_S and P_G are obtained applying the balance of Fig. A. 2.

A.2   Convection

Convective schemes are aimed at the modeling of updrafts, downdrafts and related convergent and divergent compensative motions. These currents, carrying the moist warm air of the lower troposphere, are responsible, under atmospheric unstable conditions, of the mechanisms of generation of deep clouds and rainstorms. The goal of these models is twofold: estimate the convectively induced precipitation and correct the resolved fields by the modification of the vertical profiles of heat and moisture fluxes. Convective schemes are intended for an application up to horizontal resolution of 10 km; at higher resolutions the convective clouds start to be explicitly computed by the governing equations. The two main categories of convective schemes are: mass flux and adjustment. The formers are based on the modeling, by means of physically based relationships, of the convection phenomenon and on the computation of its effects on the grid points; the latter only correct the profiles of the pertinent variables by the use of empirical or semi-empirical relationships.

Among the mass flux schemes, the Kain-Fritsch (Kain and Fritsch 1990) is widely used for mesoscale investigations. It is one-dimensional and applies to air columns. The onset of convective motions, represented by an updraft and a downdraft, is related to the amount of kinetic energy of the air parcels on the considered vertical profile, evaluated by the CAPE (Convective Available Potential Energy):

$$CAPE = \frac{1}{2} w^2 \Big|_{\widehat{EL}} - \frac{1}{2} w^2 \Big|_{\widehat{LFC}} = \int_{\widehat{LFC}}^{\widehat{EL}} g \frac{\hat{T}_U(z) - \hat{T}(z)}{\hat{T}(z)} dz \tag{A. 10}$$

where:

- – EL Equilibrium Level;

- – LFC Level of Free Convection;

- – $\hat{T}_U(z)$ characteristic temperature of the updraft;

- – $\hat{T}(z)$ temperature on the grid points;

- – w vertical velocity.

The overbar denotes the variables after the convective correction. Once the condition CAPE > 0 is verified for a given column, the convective circulation will continue up to the complete removal of the CAPE. The iterations end when $CAPE-\Delta CAPE=0\pm0.05CAPE$.

The temperature at a given point is computed as the area weighted average of the updraft, downdraft and environment temperatures:

$$\hat{T}(z)=\frac{T_E(z)A_E(z)+T_U(z)A_U(z)+T_D(z)A_D(z)}{A} \tag{A. 11}$$

An analogous relationship is applied to the relative humidity $\hat{r}(z)$:

$$\hat{r}(z)=\frac{r_E(z)A_E(z)+r_U(z)A_U(z)+r_D(z)A_D(z)}{A} \tag{A. 12}$$

where $A=A_E(z)+A_U(z)+A_D(z)$ is the cross section of the considered air column (equal to the face of the computational cell); the subscripts refer to: environment air, updraft and downdraft, respectively.

Starting at 100 mb above the ground, it is assumed the uplift of an air mass with a temperature T_U; this temperature is compared to that of the above levels T. The level where $T_U-T+\Delta T>0$ is assumed as the base of the convective cells. The perturbation ΔT is a function of wind speed w_G at the LCL (Lift Condensation Level) height. The first guess value for $A_U(LCL)$ is equal to 1% of A. The contribution of environment air to the updraft over the interval Δz is:

$$\delta M_E(z)=M_{U0}\left(0.2\frac{\Delta z}{\sqrt{\dfrac{A_U(LCL)}{\pi}}}\right) \tag{A. 13}$$

with:
$$M_{U0}=\rho w_{LCL}A_U(LCL) \tag{A. 14}$$

which gives $M_U(z)$. $T_U(z)$ and $r_U(z)$ are evaluated imposing the conservation of the equivalent potential temperature during the mixing process. $w_U(z)$ is given by:

$$w_U^2(z) = w_U^2(z-\Delta z) + 2g \int\limits_{z-\Delta z}^{z} \frac{T_U(k) - T_E(k)}{T_E(k)} dk \tag{A. 15}$$

At the LFS (Level of Free Sink) the $T_U(z) - T_E(z)$ is negative, the air mass is then characterized by negative buoyancy; this leads to the onset of a downdraft with velocity $w_D(z)$, temperature $T_D(z)$ and humidity $r_D(z)$. $M_D(z)$ is a function of w_{LFS} and is evaluated with the same procedure described for $M_U(z)$. $T_D(z)$ and $r_D(z)$ come from the adiabatic transformation associated to the downdraft. $w_D(z)$ is given by:

$$w_D^2(z) = w_D^2(z+\Delta z) + 2g \int\limits_{z+\Delta z}^{z} \frac{T_D(k) - T_E(k)}{T_E(k)} dk \tag{A. 16}$$

$\rho_U(z)$ and $\rho_D(z)$ are evaluated using the state equation, assuming the pressure at a given level in the updraft and in the downdraft to be equal to the pressure computed by the model for that grid point. $A_U(z)$ and $A_D(z)$ are given by:

$$A_U(z) = \frac{M_U(z)}{\rho_U(z) w_U(z)} \tag{A. 17}$$

$$A_D(z) = \frac{M_D(z)}{\rho_D(z) w_D(z)} \tag{A. 18}$$

The updated values for temperature and relative humidity come from (A. 11) - (A. 12), the CAPE is then updated and the iterative process continues.

The scheme provides also the precipitation (even if no without distinguish between liquid and solid contributions) deriving from the removal of the condensate produced by the convective motions:

$$r_c(z) = r_{c0} \left(1 - e^{-\frac{c_1 z}{w}} \right) \tag{A. 19}$$

where $c_1 = 0.01 s^{-1}$ and r_{c0} is given by the sum of the condensate at level z - 1 and half of the degree of supersaturation at level z+1.

A.3 Radiation

Radiative schemes provide the thermal forcing due to solar irradiation in the components of infrared and visible. The longwave radiation comes from the surface emissivity which, in turn, depends on the soil type and the ground temperature. The shortwave energy flux is due to the reflection caused by surfaces albedo. The energy of solar irradiation is subject, passing through the atmosphere and at the ground, to diffusion, absorption and reflection. The radiation schemes for LAMS are one-dimensional; for urban-canyon resolving simulations it is necessary to use more complex three-dimensional schemes which take into account the differential heating of the building walls. The principal differences among the various schemes are related to the spectrum amplitude, the number of spectral bands and the chemical-

physical elements taken into account for the reflection, refraction and absorption processes. Two kinds of models are used for the shortwave and longwave radiations, respectively. We will briefly describe the RRTM (Rapid Radiative Transfer Model) for the infrared (Mlawer et al. 1997) and the model developed by Dudhia (1989) for the visible.

The RRTM works in the frequency range of 10 - 3000 cm^{-1}. For each vertical level only some representative values of the absorption coefficient $k(\nu)$ are considered. Given the irregular variability of $k(\nu)$, it is necessary to order its values monotonically through a transformation from the space $k(\nu)$ to $k(g)$, where $g(k)$ has the form of a probability density function. The domain of the variable $g(k)$ is subdivided into 16 discrete intervals to each corresponds a characteristic value of the absorption coefficient k_j. These values are then used to evaluate the outgoing radiance R for the vertical level:

$$R(z)=\sum_{j=1}^{16}W_jR_j(z)=\sum_{j=1}^{16}W_j\left[B_{eff,j}(z)+\left(R_{0j}-B_{eff,j}(z)\right)e^{-k_j\frac{\rho\Delta z}{\cos\varphi}}\right] \tag{A. 20}$$

where W_j is the weight associated to the spectral interval, R_{0j} is the incoming radiance of the vertical level, ρ is the air density, Δz is the depth of the level and φ is the angle of incidence of the radiation. $B_{eff,j}$ is the effective Planck function, defined preserving the continuity of the flux between consecutive levels:

$$B_{eff,j}=\frac{B_{lay}+0.2\tau B_{bnd}}{1+0.2\tau} \tag{A. 21}$$

where $\tau=k_j\rho\Delta z$ is the optical depth of the level, B_{lay} and B_{bnd} are the values of the Planck function, computed for the temperature of the level and that of the following level, respectively. The Planck function $B(\nu,\theta)$ is defined by:

$$B(\nu,\theta)=\frac{8\pi h\nu^3}{c^3e^{\frac{h\nu}{\kappa\theta}}-1} \tag{A. 22}$$

where θ is the potential temperature, h is the Planck constant and κ is the Boltzmann constant.

The absorption coefficients k_j are linearly interpolated from a database of known values (containing 59 pressure levels with a constant spacing in logarithmic scale) relative to atmospheric conditions (pressure, temperature, relative humidity) comparable with those of the investigated region. The presence of chemical compounds different from water (CO_2, O_3, CH_4, N_2O, CCl_4, CFC) is taken into account in the database considering characteristical average distributions for the upper (96–0.01 mb) and lower (1050 – 96 mb) atmosphere.

The model developed by Dudhia considers only one spectral band and the radiative flux is assumed to be entirely downward. The model accounts for the effect of the

solar zenith angle, which reduces the incoming radiative flux and increases the radiation path through the atmosphere. The shortwave radiation flux $S_d(z)$ is:

$$S_d(z) = \mu S_0 - \int_z^{top} \left(dS_{cs} + dS_{ca} + dS_s + dS_a \right) \qquad \text{(A. 23)}$$

where μ is the cosine of the solar zenith angle and S_0 is the solar constant. The effects of the clouds are taken into account by two terms: S_{cs} represents the diffusion and S_{ca} includes the absorption processes; both terms are linearly interpolated from a database (Stephens 1978) whose values are functions of μ and the condensate M_l. The air absorption S_a is related to the water vapor content M_{va} and to μ. The air diffusion S_s is considered uniform and proportional to ρ, being also function of μ.

A.4   Soil models

The Land Surface Models (LSMs) provide the surface values of temperature and humidity, to be used by the surface layer schemes for the computation of the fluxes at the first model layer. The progressively increasing resolution of the mesoscale models and the application of the LES technique require a significant detail of the information on the local forcings (strongly dependent on topography, vegetation and land use); it is thus evident the great importance assumed by the LSMs. The input variables are: radiative forcing from the RA schemes and precipitation from MP and CP schemes; soil type and vegetation are used to compute the latent heat flux. The LSMs differ for the number of soil layers considered, the completeness of the relations describing heat and hydraulic exchanging processes, description of the vegetative processes and the effects of snow cover. The schemes operative on the mesoscale are one-dimensional.

We will briefly describe, as an example, the scheme developed by Chen and Dudhia (2001). The model considers four layers in the first 2 m of the soil and the potential presence of a superficial snow cover. The thicknesses of the layers are, starting from the surface: 10, 30, 60 and 100 cm. Empirical relationships account for the water exchange processes connected to the roots (in the first meter from the surface), the evapotranspiration and the superficial runoff (Fig. A. 3).
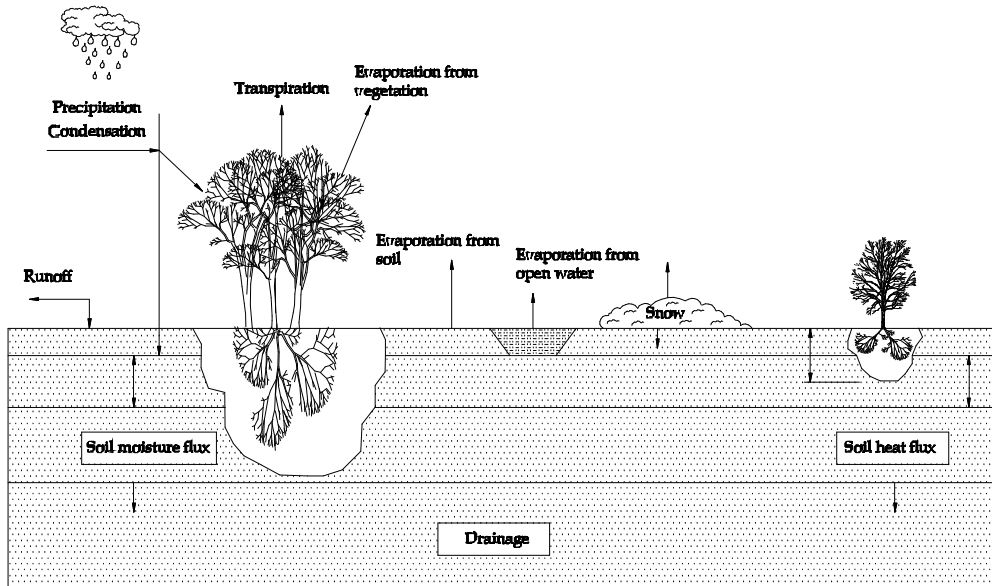
Fig. A. 3. Physical processes modeled by the LSM model of Dudhia (2001).

The effects of vegetation depend on the category of the plants, the season and the soil texture; these data can be obtained from the USGS (United States Geological Service) database, along with the values of albedo and green vegetation fraction. The skin temperature is computed applying the thermal diffusion equation to the soil layers:

$$C(\Theta)\frac{\partial T}{\partial t} = \frac{\partial}{\partial z}\left[K_t(\Theta)\frac{\partial T}{\partial z}\right] \tag{A. 24}$$

where T is the temperature, $C(\Theta)$ $\left(\dfrac{J}{m^3 K}\right)$ is the heat capacity, $K_t(\Theta)$ $\left(\dfrac{W}{mK}\right)$ is the thermal conductivity and Θ is the soil water content (moisture). At the bottom (3 m depth) the temperature is fixed to the mean annual surface temperature. The moisture is computed by the Richard equation:

$$\frac{\partial \Theta}{\partial t} = \frac{\partial}{\partial z}\left(D(\Theta)\frac{\partial \Theta}{\partial z}\right) + \frac{\partial K(\Theta)}{\partial z} + F_\Theta \tag{A. 25}$$

where D is the water diffusivity on the terrain, K is the hydraulic conductivity and the term F_Θ accounts for sources and sinks (precipitation, evapotranspiration, surface runoff, draining). The computation of the evapotranspiration term depends on the surface exchange coefficients C_h and C_q, which are provided by the surface layer scheme.

Whenever snow cover is present, the heat flux G between the soil and the snow surface is given by:

$$G = K_{snow}\frac{T_s - T_{soil}}{D_{snow}} \tag{A. 26}$$

where T_s is the surface temperature, T_{soil} is the temperature of the first soil layer, D_{snow} is the snow cover depth and K_{snow} is the thermal diffusivity of the snow $\left(0.35\dfrac{W}{mK}\right)$.

A.5   Surface Layer

Surface layer modeling relies on the Monin-Obukhov similarity theory, by the evaluation of the friction velocity and the surface exchange coefficients; these variables allow for the computation of the heat, humidity and momentum fluxes in the lower portion of the atmosphere (about 10% of the vertical extent of the PBL), where they are assumed to be constant with height. Similarity theory is based on the Buckingham theorem: every physical law can be expressed as a function of a certain number of non-dimensional parameters; these have to be at least equal to the number n of the quantities involved in the modeled phenomenon minus the number m of the base quantities, that is, n - m non-dimensional parameters. Every quantity must appear at least in one of the non-dimensional parameters and these have to be mutually independent. Monin-Obukhov theory assumes a horizontally homogeneous surface layer with the mean wind and the turbulent characteristics being dependent on five variables: height z, friction velocity u_*, kinematic heat flux $\overline{w'\theta'}_s$, humidity flux $\overline{w'q'}_s$ and buoyancy $\dfrac{g}{\theta}$. θ is the virtual potential temperature and w is the vertical component of the velocity. The apex denotes turbulent fluctuations. Similarity hypothesis implies that: the horizontal velocity field is homogeneous and stationary, the turbulent heat and momentum fluxes are not dependent on the height, the molecular diffusion is negligible with respect to the turbulent transport and the Coriolis force is negligible with respect to friction effects.

The quantities considered for the determination of the non-dimensional groups are:

z height

$$u_*=\left[\left(\overline{u'w'}_s\right)^2+\left(\overline{v'w'}_s\right)^2\right]^{1/4}$$ friction velocity

$$\theta_*=\frac{-\overline{w'\theta'}_s}{u_*}$$ temperature scale

$$q_*=\frac{-\overline{w'q'}_s}{u_*}$$ humidity scale

$$L=\frac{u_*^3}{\kappa\dfrac{g}{\theta}\overline{w'\theta'}_s}$$ Monin-Obuchov length

(A. 27)

where κ = 0.4 is the von Kármán constant.
Therefore, for the mean wind profile the relationship is of the type:

$$f_1\left(\frac{\partial u}{\partial z},z,u_*,L\right)=0 \tag{A. 28}$$

The base quantities are m = 2 (length and time) and the independent variables are n = 4 ($\frac{\partial u}{\partial z}$, z, u_*, L); following the Buckingham theory it is possible to define two non-dimensional parameters related by:

$$\frac{\partial u}{\partial z}\frac{Lk}{u_*}=\varphi_m\left(\frac{z}{L}\right)$$ (A. 29)

For the potential temperature profile the base quantities are: temperature and length; the independent variables are: $\frac{\partial \theta}{\partial z}$, z, θ_*, L.

$$f_2\left(\frac{\partial \theta}{\partial z},z,\theta_*,L\right)=0$$ (A. 30)

$$\frac{\partial \theta}{\partial z}\frac{Lk}{\theta_*}=\varphi_h\left(\frac{z}{L}\right)$$ (A. 31)

Likewise, considering as base quantities mass and length and as independent variables $\frac{\partial q}{\partial z}$, z, q_*, L, it is possible to obtain the humidity profile:

$$f_3\left(\frac{\partial q}{\partial z},z,q_*,L\right)=0$$ (A. 32)

$$\frac{\partial q}{\partial z}\frac{Lk}{q_*}=\varphi_h\left(\frac{z}{L}\right)$$ (A. 33)

The expressions for the stability functions $\varphi_m\left(\frac{z}{L}\right)$ and $\varphi_h\left(\frac{z}{L}\right)$ depend on the stability regime.

As an example, we present the surface layer scheme developed by Zhang and Anthes (1984). This model makes use of the stability functions from Dyer and Hicks (1970), Paulson (1970) and Webb (1970). Depending on the surface bulk Richardson number $Ri_b=\frac{gz_1}{\theta_1}\frac{\theta_1-\theta_s}{U_1^2}$ four stability regimes are considered:

$Ri_b \geq 0.2$:

$$\varphi_m = \varphi_h = \frac{-10}{\ln\left(\dfrac{z_1}{z_0}\right)}$$

$0 < Ri_b < 0.2$:

$$\varphi_m = \varphi_h = \frac{-5Ri_b \ln\left(\dfrac{z_1}{z_0}\right)}{1.1 - 5Ri_b}$$

$Ri_b = 0$:

$$\varphi_m = \varphi_h = 0$$

(A. 34)

$Ri_b < 0$:

$$
\left\{
\begin{aligned}
\varphi_m &= 2\ln\left\{\frac{1}{2}\left[1 + \left(1 + 16\frac{z_1}{L}\right)^{1/4}\right]\right\} + \ln\left\{\frac{1}{2}\left[1 + \left(1 - 16\frac{z_1}{L}\right)^{1/2}\right]\right\} \\
&\quad -2\arctan\left[\left(1 - 16\frac{z_1}{L}\right)^{1/4}\right] + \frac{\pi}{2} \\
\varphi_h &= 2\ln\left\{\frac{1}{2}\left[1 + \left(1 - 16\frac{z_1}{L}\right)^{1/2}\right]\right\}
\end{aligned}
\right.
$$

where the variables defined at the surface are denoted by the subscript $_s$ and those defined at the first model layer by $_1$. $U_1 = \sqrt{u_1^2 + v_1^2}$ is the intensity of the horizontal wind and $\dfrac{z_1}{L} = \dfrac{\kappa \dfrac{g}{\theta_1} z_1 \theta_*}{u_*^2}$.

The friction velocity u_* is given by:

$$u_* = \frac{1}{2}\frac{\kappa U_1}{\ln\left(\dfrac{z_1}{z_0}\right) - \varphi_m}$$

(A. 35)

where z_0 is the surface roughness length and depends on the land use category. The temperature scale θ_* is:

$$\theta_* = \frac{\kappa\left(\theta_1 - \theta_s\right)}{\varphi_h}$$

(A. 36)

The humidity scale is expressed in the same form of (A. 36):

$$q_* = \frac{\kappa\left(q_1 - q_s\right)}{\varphi_h}$$

(A. 37)

The surface exchange coefficient for the heat is:

$$C_h = \frac{c_p \rho u_* \theta_*}{\theta_1 - \theta_s}$$

(A. 38)

and for the humidity:

$$C_q = \frac{c_p \rho u_* q_*}{q_1 - q_s}$$

(A. 39)

where c_p is the specific heat at constant pressure.

The heat and moisture surface fluxes are readily evaluated by the third and fourth expressions in (A. 27). The momentum fluxes are given by:

$$\overline{u'w'}_s = \frac{u_*^2 u_1}{U_1}$$

$$\overline{v'w'}_s = \frac{u_*^2 v_1}{U_1}$$

(A. 40)

A.6   Planetary Boundary Layer

The PBL schemes model the effects of the subgrid vertical fluxes. Therefore, when activated, the vertical diffusion term in the turbulent transport equations is ignored. These models are coupled to the SFC and LSM models, which provide them the lower boundary conditions. The PBL schemes are one-dimensional and assume a clear separation between resolved and subgrid motions; this hypothesis holds only if the horizontal resolution is much coarser than the vertical one, that is for horizontal meshes larger than 1 km; for higher resolutions a three dimensional turbulence transport scheme must be used.

We will briefly describe the PBL model developed by Hong and Pan (1996). The scheme makes use of the non-local counter-gradient theory for the computation of heat and moisture fluxes under unstable conditions; therefore the vertical fluxes depend not only on the local gradients of the resolved variables but also on the presence of large coherent spatial structures (thermals). The turbulence diffusion equation for the generic variable C (u, v, θ, q) is:

$$\frac{\partial C}{\partial t} = \frac{\partial}{\partial z}\left[K_c \left(\frac{\partial C}{\partial z} - \gamma_c \right) \right]$$

(A. 41)

where K_c is the vertical eddy diffusivity coefficient and the counter-gradient term γ_c is a correction to the local gradient which accounts for the contribution of the large scale structures. The counter-gradient term is considered only for the transport of θ and q. The vertical momentum diffusivity coefficient is:

$$K_{zm} = k w_s z \left(1 - \frac{z}{z_i} \right)^p$$

(A. 42)

104

with p = 2; z_i is the PBL height. The scale velocity w_s is given by:

$$w_s = \frac{u_*}{\varphi_m}$$ (A. 43)

u_* and φ_m are provided by the SFC scheme; the height of the surface layer is assumed to be equal to $0.1z_i$.

The counter-gradient terms for heat and moisture fluxes are:

$$\gamma_\theta = b \frac{\overline{w'\theta'}_s}{w_s}$$
$$\gamma_q = b \frac{\overline{w'q'}_s}{w_s}$$ (A. 44)

with b = 7.8. $\overline{w'\theta'}_s$ and $\overline{w'q'}_s$ are provided by the SFC scheme.

The PBL height z_i is evaluated iteratively from:

$$z_i = Ri_{bcr} \frac{\theta_1 U(h)^2}{g[\theta(h) - \theta_{sa}]}$$ (A. 45)

where $Ri_{bcr} = 0.5$ is the critical bulk Richardson number. The temperature near the surface θ_{sa} is given by:

$$\theta_{sa} = \theta_1 + b \frac{\overline{w'\theta'}_s}{w_s z_i}$$ (A. 46)

The vertical eddy diffusivity coefficient K_{zh} for temperature and humidity fluxes is a function of the vertical momentum diffusivity coefficient K_{zm} via the Prandtl number:

$$K_{zh} = \frac{K_{zm}}{Pr}$$ (A. 47)

The vertical diffusion in the free atmosphere (above z_i) is modeled with a local approach. The vertical eddy diffusivity coefficient is given by:

$$K_{m,h} = l^2 f_{m,h} Ri_g \left| \frac{\partial U}{\partial z} \right|$$ (A. 48)

where $Ri_g = \frac{g}{\theta} \frac{\frac{\partial \theta}{\partial z}}{\left| \frac{\partial U}{\partial z} \right|^2}$ is the gradient Richardson number. The characteristic length scale l is given by:

$$\frac{1}{l} = \frac{1}{\kappa z} + \frac{1}{\lambda_0}$$ (A. 49)

where $\lambda_0 = 30m$ is the asymptotic length scale.

The stability function $f_{m,h}$ depends on the atmospheric stability:

$Ri_g > 0$:

$$f_{m,h} = e^{-8.5Ri_g} + \frac{0.15}{Ri_g + 3}$$ (A. 50)

$Ri_g \leq 0$:

$$\begin{cases} f_m = \varphi_m \\ f_h = \varphi_h \end{cases}$$

That is, under neutral and unstable conditions the stability functions are taken equal to those valid for the surface layer (A. 34), substituting $\frac{z_1}{L}$ with Ri_g.

References

Adams, J. C., P. N. Swarztrauber, 1997: SPHEREPACK 2.0: A model development facility. *NCAR/TN-436-STR*, 59 pp.

Anquetin, S., C. Guilbaud, J. P. Chollet, 1998: The formation and destruction of inversion layers within a deep valley. *J. Appl. Meteor.*, **37**, 1547-1560.

Antonelli, M., R. Rotunno, 2007: Large-eddy simulation of the onset of the sea breeze. *J. Atmos. Sci.*, **64**, 4445-4457.

Axelsen, S. L., H. Van Dop, 2009a: Large-eddy simulation of katabatic winds. Part I: Comparison with observations. *Acta Geophysica*, **57**, 803-836.

Axelsen, S. L., H. Van Dop, 2009b: Large-eddy simulation of katabatic winds. Part II: Sensitivity study and comparison with analytical models. *Acta Geophysica*, **57**, 837-856.

Bader, D. C., T. B. McKee, 1983: Dynamical model simulation of the morning boundary layer development in deep mountain valleys. *J. Clim. Appl. Meteor.*, **22**, 341-351.

Ball, F. K., 1956: The theory of strong katabatic winds. *Australian J. Phys.*, **9**, 373-386.

Beare, R. J., M. K. MacVean, A. M. Holtslag, J. Cuxart, I. Esau, J.-C. Golaz, M. A. Jimenez, M. Khairoutdinov, B. Kosovic, D. Lewellen, T. S. Lund, J. K. Lundquist, A. McCabe, A. F. Moene, Y. Noh, S. Raasch, P. Sullivan, 2006: An intercomparison of large-eddy simulations of the stable boundary layer. *Bound.-Layer Meteor.*, **118**, 247-272.

Brehm, M., C. Freytag, 1982: Erosion of the night-time thermal circulation in an alpine valley. *Arch. Meteor. Geoph. Biokl.*, **31**, 331-352.

Briggs, G. A., 1981: Canopy effects on predicted drainage flow characteristics and comparison with observations. *Preprints, Fifth Symp. on Turbulence, Diffusion, and Air Pollution*, Atlanta, GA, Amer. Meteor. Soc., 113–115.

Catalano, F., A. Cenedese, G. Cordisco, 2007: Numerical simulations of thermally driven slope winds. *7th EMS annual meeting / 8th ECAM*, San Lorenzo de El Escorial, Spain, 01-05 October.

Cenedese, A., A. Capriati, P. Monti, 2004: Studio di laboratorio sulla dinamica delle correnti di pendio. *29° Convegno nazionale di idraulica e costruzioni idrauliche*, Trento, Italy, 07-10 September.

Chan, W. C., 2001: The modeling of anabatic flow in complex terrain. *Master thesis*, Arizona State University.

Chen, R.-R., N. S. Berman, D. L. Boyer, H. J. S. Fernando, 1996: Physical model of diurnal heating in the vicinity of a two-dimensional ridge. *J. Atmos. Sci.*, **53**, 62-85.

Chen, F., J. Dudhia, 2001: Coupling an advanced land-surface/hydrology model with the Penn State/NCAR MM5 modeling system. Part I: Model description and implementation. *Mon. Wea. Rev.*, **129**, 569-585.

Chow, F. K., A. P. Weigel, R. L. Street, M. W. Rotach, M. Xue, 2006: High-resolution large-eddy simulations of flow in a steep alpine valley. Part I: methodology, verification and sensitivity experiments. *J. Appl. Meteor. Clim.*, **45**, 63-86.

Conzemius, R. J., E. Fedorovich, 2006: Dynamics of sheared convective boundary layer entrainment. Part I: Methodological background and large eddy simulations. *J. Atmos. Sci.*, **63**, 1151-1178.

Deardorff, J. W., 1970: A numerical study of three-dimensional turbulent channel flow at large Reynolds numbers. *J. Fluid. Mech.*, **41**, 452-480.

Deardorff, J. W., 1972: Numerical investigation of neutral and unstable planetary boundary layers. *J. Atmos. Sci.*, **29**, 91-115.

Deardorff, J. W., 1980: Stratocumulus-capped mixed layer derived from a three-dimensional model. *Boundary-Layer Meteor.*, **18**, 495-527.

Deardorff, J. W., G. E. Willis, 1987: Turbulence within a baroclinic laboratory mixed layer above a sloping surface. *J. Atmos. Sci.*, **44**, 772-778.

Dudhia, J., 1989: Numerical study of convection observed during the winter monsoon experiment using a mesoscale two-dimensional model. *J. Atmos. Sci.*, **46**, 3077-3107.

Dyer, A. J., B. B. Hicks, 1970: Flux-gradient relationships in the constant flux layer. *Quart. J. Roy. Meteor. Soc.*, **96**, 715-721.

Eidson, T. M., 1985: Numerical simulation of the turbulent Rayleigh-Bénard problem using subgrid modelling. *J. Fluid Mech.*, **158**, 245-268.

Erlebacher, G., M. Y. Hussaini, C. G. Speziale, T. A. Zang, 1992: Toward the large-eddy simulation of compressible turbulent flows. *J. Fluid. Mech.*, **238**, 155-185.

Errico, R. M., 1985: Spectra computed from a limited area grid. *Mon. Wea. Rev.*, **113**, 1554-1562.

Federer, B., A. Valdvogel, 1975: Hail and raindrop size distributions from a Swiss multicell storm. *J. Appl. Meteor.*, **14**, 91-97.

Fedorovich, E., R. Conzemius, 2008: Effects of wind shear on the atmospheric convective boundary layer structure and evolution. *Acta Geophysica*, **56**, 114-141.

Fernando, H. J. S., M. Princevac, J. C. R. Hunt, E. Pardyjak, 2000: Thermal circulation in complex terrain: a case of urban fluid mechanics. *5th International symposium on stratified flows*, Vancouver, Canada, 10-13 July.

Fernando, H. J. S., S. M. Lee, J. Anderson, M. Princevac, E. Pardyjak, S. Grossman-Clarke, 2001: Urban fluid mechanics: air circulation and contaminant dispersion in cities. *Environ. Fluid. Mech.*, **1**, 107-164.

Gunn, K. L. S., J. S. Marshall, 1958: The distribution with size of aggregate snowflakes. *J. Meteor.*, **15**, 452-461.

Haiden, T., 2003: On the pressure field in the slope wind layer. *J. Atmos. Sci.*, **60**, 1632-1635.

Haiden, T., C. D. Whiteman, 2005: Katabatic flow mechanisms on a low-angle slope. *J. Appl. Meteor.*, **44**, 113-126.

Hong, S. Y., H. L. Pan, 1996: Nonlocal boundary layer vertical diffusion in a medium-range forecast model. *Mon. Wea. Rev.*, **124**, 2322-2339.

Hunt, J. C. R., H. J. S. Fernando, M. Princevac, 2003: Unsteady thermally driven flows on gentle slopes. *J. Atmos. Sci.*, **60**, 2169-2182.

Hyun, Y.-K., K.-E. Kim, K.-J. Ha, 2005: A comparison of methods to estimate the height of stable boundary layer over a temperate grassland. *Agric. For. Meteorol.*, **132**, 132-142.

Kain, J. S., J. M. Fritsch, 1990: A One-Dimensional Entraining/Detraining Plume Model and Its Application in Convective Parameterization. *J. Atmos. Sci.*, **47**, 2784-2802.

Klemp, J. B., R. Wilhelmson, 1978: The simulation of three-dimensional convective storm dynamics. *J. Atmos. Sci.*, **35**, 1070–1096.

Kondo, J., T. Kuwagata, S. Haginoya, 1989: Heat budget analysis of nocturnal cooling and daytime heating in a basin. *J. Atmos. Sci.*, **46**, 2917-2933.

Laprise R., 1992: The Euler Equations of Motion with Hydrostatic Pressure as an Independent Variable. *Mon. Wea. Rev.*, **120**, 197-207.

Lee, S.-M., W. Giori, M. Princevac, H. J. S. Fernando, 2006: Implementation of a stable PBL parameterization for the mesoscale model MM5: nocturnal flow in complex terrain. *Boundary-Layer Meteorol.*, **119**, 109-134.

Lin, Y., R. D. Farley, H. D. Orville, 1983: Bulk Parameterization of the Snow Field in a Cloud Model. *J. Climate Appl. Meteor.*, **22**, 1065-1092.

Liu, J. Y., H. D. Orville, 1969: Numerical modeling of precipitation and cloud shadow effects on mountain-induced cumuli. *J. Atmos. Sci.*, **26**, 1283-1298.

Locatelli, J. D., P. V. Hobbs, 1974: Fall speeds and masses of solid precipitation particles. *J. Geophys. Res.*, **79**, 2185-2197.

Lundquist, K. A., F. K. Chow, J. K. Lundquist, 2010: An immersed boundary method for the Weather Research and Forecasting model. *Mon. Wea. Rev.*, **138**, 796-817.

Mahrt, L., 1982: Momentum balance of gravity flows. *J. Atmos. Sci.*, **39**, 2701-2711.

Manins, P. C., B. L. Sawford, 1979: A model of katabatic winds. *J. Atmos. Sci.*, **36**, 619-630.

Martin, J. E., 2006: Mid-latitude atmospheric dynamics. *John Wiley and Sons, Ltd.*, 336 pp.

Marshall, J. S., W. McK. Palmer, 1948: The distribution of raindrop with size. *J. Meteor.*, **5**, 165-166.

Michioka, T., F. K. Chow, 2008: High-resolution large-eddy simulations of scalar transport in atmospheric boundary layer flow over complex terrain. *J. Appl. Meteorol. Climatol.*, **47**, 3150-3169.

Mlawer, E. J., S. J. Taubman, P. D. Brown, M. J. Iacono, S. A. Clough, 1997: Radiative transfer for inhomogeneous atmosphere: RRTM, a validated correlated-k model for the longwave. *J. Geophys. Res.*, **102 (D14)**, 16663-16682.

Moeng, C.-H., 1984: A large-eddy-simulation model for the study of planetary boundary-layer turbulence. *J. Atmos. Sci.*, **41**, 2052-2062.

Moeng, C.-H., P. P. Sullivan, 1994: A comparison of shear- and buoyancy-driven planetary boundary layer flows. *J. Atmos. Sci.*, **51**, 999-1022.

Moeng, C.-H., J. C. Wyngaard, 1988: Spectral analysis of large eddy simulations of the convective boundary layer. *J. Atmos. Sci.*, **45**, 3573-3587.

Moeng, C.-H., J. Dudhia, J. Klemp, P. Sullivan, 2007: Examining two-way grid nesting for large eddy simulation of the PBL using the WRF model. *Mon. Wea. Rev.*, **135**, 2295-2311.

Monti, P., H. J. S. Fernando, M. Princevac, W. C. Chan, T. A. Kowalewski, E. R. Pardyjak, 2002: Observations of flow and turbulence in the nocturnal boundary layer over a slope. *J. Atmos. Sci.*, **59**, 2513-2534.

Nieuwstadt, F. T. M., 1990: Direct and Large Eddy Simulation of Free Convection. *Proc. 9th International Heat Transfer Conference*, Jerusalem, **I**, 37-47.

Nieuwstadt, F. T. M., P. J. Mason, C.-H. Moeng, U. Schumann, 1993: Large-eddy simulation of the convective boundary layer: A comparison of four computer codes. *Turbulent Shear Flows 8*, F. Durst et al., Eds., Springer-Verlag, 431 pp.

Noppel, H., F. Fiedler, 2002: Mesoscale heat transport over complex terrain by slope winds – a conceptual model and numerical simulations. *Boundary-Layer Meteor.*, **104**, 73-97.

Orlanski, I., 1976: A simple boundary condition for unbounded hyperbolic flows. *J. Comp. Phys.*, **21**, 251-269.

Orville, H. D., 1964: On mountain upslope winds. *J. Atmos. Sci.*, **21**, 622-633.

Patton, E. G., P. P. Sullivan, C.-H. Moeng, 2005: The influence of idealized heterogeneity on wet and dry planetary boundary layers coupled to the land surface. *J. Atmos. Sci.*, **62**, 2078-2097.

Paulson, C. A., 1970: The mathematical representation of wind speed and temperature profiles in the unstable atmospheric surface layer. *J. Appl. Meteor.*, **9**, 857-861.

Pettré, P., J.-C. André, 1991: Surface-pressure change through Loewe's phenomena and katabatic flow jumps: study of two cases in Adélie land, Antarctica. *J. Atmos. Sci.*, **48**, 557-571.

Pope, B., 2004: Ten questions concerning the large-eddy simulation of turbulent flows. *New Journal of Physics*, **6**, 35-68.

Prandtl, L., 1952: Essentials of fluid dynamics. *Hafner*, 452 pp.

Princevac, M., H. J. S. Fernando, W. C. Chan, T. A. Kowalewski, P. Monti, J. Anderson, 2001: Slope flow measurements during vertical transport and mixing (VTMX) field experiment, Salt Lake City, 2000. *2001 International symposium on environmental hydraulics*, Tempe, Arizona, 05-08 December.

Princevac, M., H. J. S. Fernando, 2005: Turbulent entrainment into natural gravity-driven flows. *J. Fluid. Mech.*, **533**, 259-268.

Princevac, M., H. J. S. Fernando, 2007: A criterion for the generation of turbulent anabatic flows. *Phys. Fluids*, **19**, 105102 1-7.

Princevac, M., H. J. S. Fernando, 2008: Morning breakup of cold pools in complex terrain. *J. Fluid. Mech.*, **616**, 99-109.

Princevac, M., J. C. R. Hunt, H. J. S. Fernando, 2008: Quasi-steady katabatic winds on slopes in wide valleys: hydraulic theory and observations. *J. Atmos. Sci.*, **65**, 627-643.

Rampanelli, G., D. Zardi, R. Rotunno, 2004: Mechanisms of up-valley winds. *J. Atmos. Sci.*, **61**, 3097-3111.

Reuten, C., D. G. Steyn, K. B. Strawbridge, P. Bovis, 2005: Observations of the relation between upslope flows and the convective boundary layer in steep terrain. *Boundary-Layer Meteor.*, **116**, 37-61.

Reuten, C., D. G. Steyn, S. E. Allen, 2007: Water tank studies of atmospheric boundary layer structure and air pollution transport in upslope flow systems. *J. Geophys. Res.*, **112**, D11114.

Reynolds, W. C., 1990: The potential and limitations of direct and large eddy simulations. *Whither Turbulence? Turbulence at the Crossroads, Lecture Notes in Physics*, **357**, ed. J. L. Lumley, Springer, Berlin, p. 313.

Rotach, M. W., and Coauthors, 2004: Turbulence structure and exchange processes in an Alpine valley: The Riviera project. *Bull. Amer. Meteor. Soc.*, **85**, 1367-1385.

Sagaut, P., 2006: Large-eddy simulation for incompressible flows. *Springer*, 556 pp.

Sakai, R. K., D. R. Fitzjarrald, K. E. Moore, 2001: Importance of low-frequency contributions to eddy fluxes observed over rough surfaces. *J. Appl. Meteor.*, **40**, 2178-2192.

Schumann, U., 1975: Subgrid scale model for finite difference simulations of turbulent flows in plane channels and annuli. *J. Comput. Phys.*, **18**, 376-404.

Schumann, U., 1990: Large-eddy simulation of the up-slope boundary layer. *Quart. J. Roy. Meteor. Soc.*, **116**, 637-670.

Scotti, A., C. Meneveau, D. K. Lilly, 1993: Generalized Smagorinsky model for anisotropic grids. *Phys. Fluids*, **5**, 2306-2308.

Segal, M., Y. Ookouchi, R. A. Pielke, 1987: On the effect of steep slope orientation on the intensity of daytime upslope flow. *Notes and correspondence J. Atmos. Sci.*, **44**, 3587-3592.

Simpson, J. E., 1994: Sea breeze and local winds. *Cambridge University Press*, 234 pp.

Skamarock, W. C., J. B. Klemp, J. Dudhia, D. O. Gill, D. M. Barker, M. G. Duda, X.-Y Huang, W. Wang, J. G Powers, 2008: A description of the advanced research WRF version 3. *NCAR/TN-475*, 125 pp.

Skyllingstad, E. D., 2003: Large-eddy simulation of katabic flows. *Boundary-Layer Meteor.*, **106**, 217-243.

Smagorinsky, J., 1963: General circulation experiments with the primitive equations: I. The basic experiment. *Mon. Wea. Rev.*, **91 (3)**, 99-164.

Smith, C. M., E. D. Skyllingstad, 2005: Numerical simulation of katabic flow with changing slope angle. *Mon. Wea. Rev.*, **133**, 3065-3080.

Sorbjan, Z., 2004: Large-eddy simulation of the baroclinic mixed layer. *Boundary-Layer Meteor.*, **112**, 57-80.

Stephens, G. L., 1978: Radiation profiles in extended water clouds. Part II: Parameterization schemes. *J. Atmos. Sci.*, **35**, 2123-2132.

Sullivan P., J. C. Mc Williams, C.-H. Moeng, 1994: A subgrid-scale model for large-eddy simulation of planetary boundary-layer flows. *Bound.-Layer Meteor.*, **71**, 247-276.

Sullivan, P. P., C.-H. Moeng, B. Stevens, D. Lenschow, S. D. Mayor, 1998: Structure of the entrainment zone capping the convective atmospheric boundary layer. *J. Atmos. Sci.*, **55**, 3042-3064.

Webb, E. K., 1970: Profile relationships: the log-linear range, and extension to strong stability. *Quart. J. Roy. Meteor. Soc.*, **96**, 67-90.

Weigel, A. P., F. K. Chow, M. W. Rotach, R. L. Street, M. Xue, 2006: High-resolution large-eddy simulations of flow in a steep alpine valley. Part II: flow structure and heat budgets. *J. Appl. Meteor. Clim.*, **45**, 87-107.

Wisner, C., H. D. Orville, C. Myers, 1972: A numerical model of a hail-bearing cloud. *J. Atmos. Sci.*, **29**, 1160-1181.

Wyngaard, J. C., 1983: Lectures on the planetary boundary layer. *Mesoscale Meteorology-Theories, Observations and Models*, D. K. Lilly and T. Gal-Chen, Eds., D. Reidel Publishing Company, 603-650.

Wyngaard, J. C., 2004: Toward numerical modeling in the "Terra Incognita". *J. Atmos. Sci.*, **61**, 1816-1826.

Ye, Z. J., M. Segal, R. A. Pielke, 1987: Effects of atmospheric thermal stability and slope steepness on the development of daytime thermally induced upslope flow. *J. Atmos. Sci.*, **44**, 3341-3354.

Yu, Y., X.-M. Cai, 2006: Structure and dynamics of katabatic flow jumps: idealised simulations. *Boundary-Layer Meteor.*, **118**, 527-555.

Zhang, D.-L., R. A. Anthes, 1982: A high-resolution model of the planetary boundary layer – sensitivity tests and comparisons with SESAME-79 data. *J. Appl. Meteor.*, **21**, 1594-1609.

Zilitinkevich, S. S., T. Elperin, N. Kleeorin, I. Rogachevskii, I. Esau, T. Mauritsen, M. W. Miles, 2008: Turbulence energetics in stably stratified geophysical flows: Strong and weak mixing regimes. *Quart. J. Roy. Meteor. Soc.*, **134**, 793-799.